The impact of multiparameter ageing of stator poles of traction motors on diagnostic methods

School of Electrical and Computer Engineering

Technical University of Crete

Antonios Douvaras

Thesis Committee: Associate Professor Konstantinos Gyftakis (Supervisor)

Professor Eftychios Koutroulis

Doctor Eleftheria Sergaki

Chania, March 2024

Περίληψη

Τα ορυκτά καύσιμα χρησιμοποιούνται ευρέως λόγω της υψηλής ενεργειακής τους πυκνότητας. Ωστόσο, η καύση τους απελευθερώνει αέρια τα οποία συμβάλλουν στην υπερθέρμανση του πλανήτη και, ως εκ τούτου, στην κλιματική αλλαγή. Κατά συνέπεια, είναι αναγκαίο να ληφθούν επιτακτικά μέτρα για τη μείωση της χρήσης τους μέσω της μετάβασης στην πράσινη ενέργεια. Ως μέρος αυτής της μετάβασης, εντάσσεται η ευρεία υιοθέτηση των ηλεκτρικών οχημάτων (EVs), με τους ηλεκτρικούς κινητήρες να αποτελούν το βασικό στοιχείο τους. Οι σύγχρονες μηχανές μόνιμων μαγνητών (Permanent Magnet Synchronous Motors - PMSMs) είναι όλο και πιο δημοφιλείς στα ηλεκτρικά οχήματα λόγω των εξαιρετικών χαρακτηριστικών τους, συμπεριλαμβανομένης της υψηλής πυκνότητας ροπής, της αυξημένης απόδοσης και της συμπαγής δομής. Ωστόσο, το ελαφρύ βάρος και το μικρό τους μέγεθος τους τα εκθέτουν σε διάφορες καταπονήσεις ανάλογα με τις απαιτήσεις της εφαρμογής, με πιθανό αποτέλεσμα την προοδευτική υποβάθμιση και την τελική αποτυχία τους. Τα σφάλματα στάτη συγκεκριμένα, είναι πολύ επικίνδυνα για τους ηλεκτρικούς κινητήρες λόγω της ταχείας εξέλιξής τους σε καταστροφικά breakdown, που συχνά συνδέονται με την υποβάθμιση και την αποτυχία του συστήματος μόνωσης. Η παρούσα διπλωματική εργασία στοχεύει στην εφαρμογή ενός συνδυασμού καταπονήσεων στους πόλους στάτη με τύλιγμα ενός κινητήρα PMSM. Ο αντίκτυπος αυτών των καταπονήσεων θα αναλυθεί μέσω της χρήσης Frequency Response Analysis (FRA), διαγραμμάτων Nyquist, Breakdown Test και Dissipation Factor (tanδ). Ταυτόχρονα, αναπτύχθηκε ένα λεπτομερές ισοδύναμο κύκλωμα των πόλων υπό μελέτη για την πραγματοποίηση Frequency Response Analysis. Αυτό το κύκλωμα θα αποσαφηνίσει τον αντίκτυπο της εφαρμογής πολλαπλών ειδών καταπόνησης στις παραμέτρους του μοντέλου, διευκολύνοντας το προσδιορισμό της παραμέτρου που επηρεάζεται σε κάθε κύκλο καταπόνησης.

Abstract

Fossil fuels are extensively utilized globally due to their high energy density; however, their combustion releases greenhouse gases, contributing to global warming and, as a result, climate change. Consequently, imperative measures to reduce their usage are achievable through transitioning to green energy. As part of this transition, there is widespread adoption of electric vehicles (EVs), with electric motors serving as their core components. Permanent Magnet Synchronous Motors (PMSMs) are increasingly favoured in EVs due to their exceptional characteristics, including high torque density, elevated efficiency, and compact structure. Nevertheless, their lightweight and small size expose them to various stresses depending on application requirements, potentially resulting in progressive degradation and eventual failure. Stator faults, particularly, pose significant concerns in electric motors due to their rapid evolution into catastrophic breakdowns, often associated with insulation system degradation and failure. This master's thesis aims to apply a combination of stresses to the poles of a permanent magnet motor's stator poles with mounted armature coils. The impact of these stresses will be analysed through impedance spectroscopy employing Frequency Response Analysis (FRA), Nyquist diagrams, Breakdown test and the dissipation factor (tanδ). Concurrently, a detailed equivalent circuit of poles has been developed for impedance spectroscopy purposes. This circuit will clarify the impact of applying multiple stresses on the model's parameters, facilitating the identification of the affected parameter in each cycle of the multistress procedure.

Table of Contents

Acronyms

EVs Electric Vehicles
CPSR Constant Power Speed Range
BLDCs Permanent Magnet Brushless DC Motors
IMs Induction Motors
SRMs Switched Reluctance Motors
PMs Permanent Magnets
PMSMs Permanent Magnet Synchronous Motors
YASA Yokeless And Segmented Armature
AFPMS Axial Flux Permanent Magnet Machines
PDs Partial Discharges
DEV Partial Discharge Extinction Voltage
IFDs Inverter-Fed Drives
SE, DE, ME Static, Dynamic, Mixed Eccentricity
UMP Unbalance Magnetic Pull
ITSC Inter-Turn Short Circuit
FFT Fast Fourier Transform
PSD Power Spectral Density
MCSA Machine Current Signature Analysis
RUL Remaining Useful Life
PAI Polyamide-Imide
PEI Polyester-Imide
IR Insulation Resistance
PI Polarization Index
DF Dissipation Factor
PF Power Factor
PFTU/DFTU Power Factor Tip-Up/Dissipation Factor Tip-Up
PPAs Pulse Phase Analyzers
PMAs Pulse Magnitude Analyzers
DIV Discharge Inception Voltage
Q_m peak PD magnitudes
FRA Frequency Response Analysis
S_k Skewness

Aknowledgements

Chapter 1: Traction Motors for Electric Vehicles (EVs)

Fossil fuels are widely used worldwide due to their high energy density. However, their combustion releases greenhouse gases, contributing significantly to global warming. Power plants, in particular, emit a substantial portion of these gases. Climate change-induced natural disasters, such as storms, wildfires, floods, and droughts, have had severe impacts, causing substantial economic losses. These disasters also pose risks to various aspects of life, including food security, water resources, human health, habitats, and ecosystems [1].

Forecasts [2] suggest a substantial 56% increase in energy demand by 2040. However, persisting with the current reliance on fossil fuels would only exacerbate the situation, leading to a surge in greenhouse gas emissions and worsening climate change. Hence, it's crucial to take decisive action to mitigate these adverse outcomes. Renewable energy sources emerge as crucial players in striving for carbon neutrality, thus curbing global warming and addressing climate change. These sources are highly regarded for their affordability, sustainability, and accessibility, marking a notable shift toward a sustainable energy landscape amidst global environmental challenges. The pressing need to combat climate change and foster sustainable development further drives the momentum toward global renewable energy transition. Envisioning a sustainable energy future involves initiatives like promoting green buildings, fostering sustainable energy practices in industries, and embracing eco-friendly transportation options.

In this context, the widespread adoption of electric vehicles (EVs) stands as a viable solution to tackling environmental and energy crises. EVs utilize electricity as a cleaner substitute for fossil fuels, resulting in emissions-free driving. This positive environmental impact can be further bolstered by sourcing electricity from renewable sources like wind, solar, or biomass. Consequently, the transition to electric mobility not only reduces environmental pollution but also fosters public health benefits and diminishes reliance on fossil fuels, marking a pivotal shift towards sustainable energy practices. Since 2010, the growth rate of EVs has exceeded that of conventional

vehicles, with recent years witnessing a notable surge in global sales. By 2018, the global stock of electric passenger cars had reached 5 million, led by China, followed by Europe and the United States. By the close of 2021, the global EV fleet had expanded to approximately 16.5 million vehicles, showcasing a significant threefold increase from 2018 [3]. The surge in the adoption of electric vehicles (EVs) has spurred a significant expansion of research in this field, notably with a focus on traction motors, recognized as the pivotal component of EV technology.

This chapter focuses on exploring the performance requirements the performance criteria essential for traction motors in EVs (Section 1.1), while also showcasing the designs of these motors, ranging from conventional (Section 1.2) to more special configurations (Section 1.3), commonly employed in the electric automotive sector. These structures are meticulously crafted to fulfil a wide array of performance requirements, as elucidated in Section 1.2. Finally, the scope (Section 1.4) and outline (Section 1.5) of the thesis will be introduced.

1.1 Comprehensive Investigation of Performance Requirements for Traction Motors

In the present era, various electric vehicle models have been developed, each designed to meet specific application needs for EVs. These vehicles are primarily designed for the transportation of individuals or cargo. Consequently, the transportation industry must guarantee a specified safety, usability, and operational efficiency level to align with client expectations. Moreover, adhering conscientiously to the following requirements during the selection and design of traction motors [4], [5] is equally crucial:

- High Efficiency
- High Power & Torque Density
- Fault Tolerance
- Reduced Vibration & Noise
- Limited Volume
- Optimal Cost
- High starting torque and great hill-climbing ability
- Extended CPSR(Constant Power Speed Range): the ratio of the highest speed at which rated power can be developed in high-speed mode while operating within the current rating, divided by the base speed
- High reliability
- Reduced power losses

- Simple Structure

1.2 Structures of Conventional Electric Machines in EVs

Researchers have thoroughly explored various structural designs to meet the specific demands of electrical machines in electric vehicles (EVs). The most important and widely used traction motors in the automotive industry are the following [6], [7]:

1.2.1 Brushed DC Motors

Brushed DC motors (Fig.1.1) use brushes to deliver current to the motor windings through a mechanical commutator- a rotary electrical switch that periodically reverses the current direction between the rotor and the external circuit.
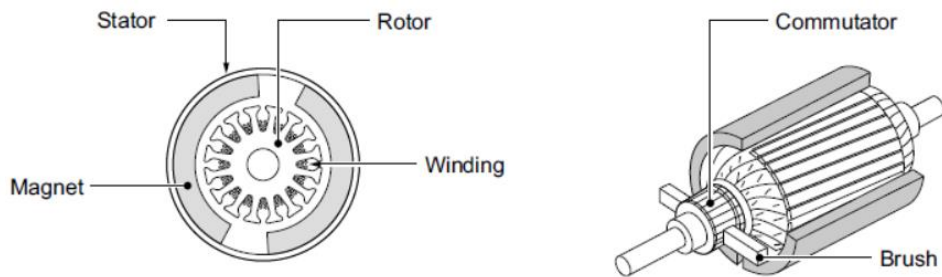
Fig.1.1. Brushed DC motor topology [16]

They demonstrate favourable torque versus speed performance characteristics for electric vehicle (EV) applications, with a high starting torque capability and, ideally, a broad CPSR -qualities that make them a suitable option for traction applications. However, the presence of brushes and commutators impacts the reliability of the motor, requiring frequent maintenance and imposing limitations on its maximum speed. Typically, these motors also exhibit lower efficiency and power density.

1.2.2 Permanent Magnet Brushless DC Motors (BLDCs)

BLDCs (Fig 1.2) utilize an inverter in place of a commutator. Due to the lack of brushes, they can operate at extremely high speeds. Typically, these motors integrate surface-mounted permanent magnets (PMs) on the rotor. The utilization of rare-earth PMs enhances the capability of BLDCs to achieve high efficiency and power density.
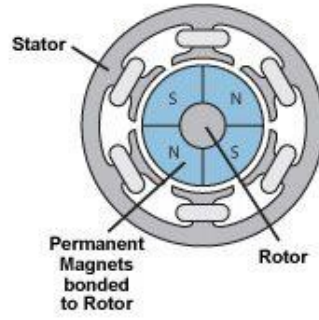
Fig.1.2. BLDC topology [17]

A notable challenge faced by BLDC motors is the constrained Constant Power Speed Range (CPSR), commonly known as the field-weakening range. This limitation is primarily attributed to the heightened back-electromotive force (back-emf) at high speeds—a voltage generated by a running motor that opposes the supplied voltage. Additionally, it is influenced by the reduced inductance associated with the surface-mounted configuration and the constrained control flexibility. Mitigating these challenges can be accomplished through the incorporation of an additional field winding. However, such configurations introduce heightened complexity, and the achievable speed ratio may not align with the specific demands of EV applications.

1.2.3 Induction Motors (IMs)

Induction Motors (Fig.1.3) stand out as one of the most extensively used traction motors in the automotive industry. Induction Motors (IMs) present advantages with their well-established technology, robust structures, cost-effectiveness, high starting torque, and impressive hill-climbing ability [13]-[15]. Furthermore, IMs demonstrate low noise and vibration levels, boast high reliability, and require low maintenance costs. The constant power range of Induction Motors (IMs) can be expanded to approximately 4-5 times the base speed, typically necessary for traction applications. Nevertheless, the feasibility of high-speed and constant power range operation is restricted by the limitations imposed by the pullout torque, which represents the maximum torque achievable by the motor [15]. In Fig.1.4 the IM torque& power-rotor speed curves are presented and variable variations with speed.
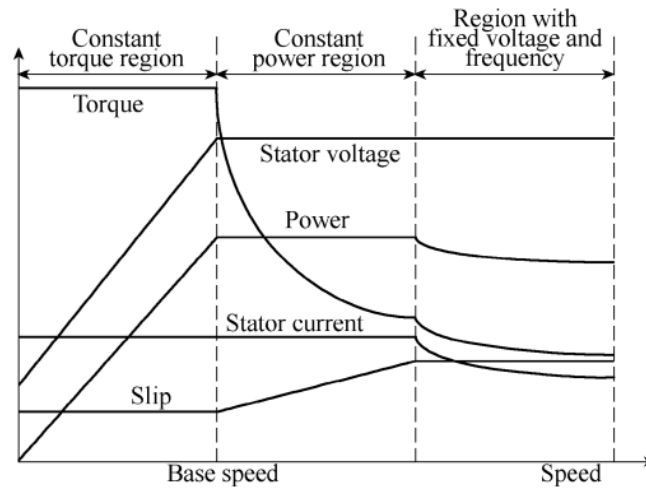
Fig.1.4. IM characteristics-rotor speed [15]

Nevertheless, IMs display drawbacks, including elevated losses, a lower power factor, and reduced efficiency. Furthermore, when compared to Permanent Magnet (PM) machines, IMs tend to have greater weight, increased volume, and less compactness. Addressing these challenges necessitates research endeavours aimed at resolving issues, either through improvements at the design stage or the proposal of innovative control schemes and/or converter topologies.

Fig.1.3. Induction Machine cross-section [5]

1.2.4 Switched Reluctance Motors (SRMs)

Although Switched Reluctance Motors (SRMs) have been in existence since 1814, practical applications of these motors emerged with advancements in power electronic devices. Therefore, they have emerged as a new contender in the automotive industry.

SRMs (Fig.1.5), showcase a typical rotor without excitation coils or permanent magnets (PMs) in the rotor. Some advantages of SRMs include low maintenance and production costs since no excitation is required in the rotor, minimizing rotor losses. Additionally, the motors feature a simple structure and exhibit fault tolerance, low inertia, temperature insensitivity, and robustness. They achieve satisfactory

performance levels and showcase a broad constant power torque-speed characteristic. Due to the absence of coils in the rotor, it can operate at high speeds and generate lower rotor heat. The torque-speed characteristics of SRMs align effectively with typical Electric Vehicle (EV) load profiles, delivering high torque at low speeds and a broad CPSR. These attributes enable manufacturers to eliminate the mechanical transmission components, like gearboxes. Moreover, alongside these advantages, drawbacks such as high acoustic noise and vibrations, torque ripple, and the necessity for a specialized converter topology may be encountered.
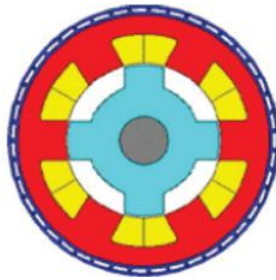
Fig.1.5. Switched Reluctance Motor cross-section [5]

1.2.5 Permanent Magner Synchronous Motor (PMSM)

These motors are being explored as an alternative to traction induction motors (IMs), and are applied in most of the current EVs [15], offering notable advantages such as remarkable power density and efficiency. Moreover, due to the absence of rotor windings, copper losses do not occur, reducing the need for extensive cooling. Similar to BLDCs, they incorporate permanent magnets (PMs) on the rotor. The PMSM can be implemented within a smaller volume for the same speed and power than the SRM. Despite its elevated cost due to the use of rare earth magnets, the PMSM stands as a robust alternative to traction IMs, attributed to its superior efficiency.

Depending on the configuration of the PMs, PMSMs can be classified into two categories (Fig.1.6).
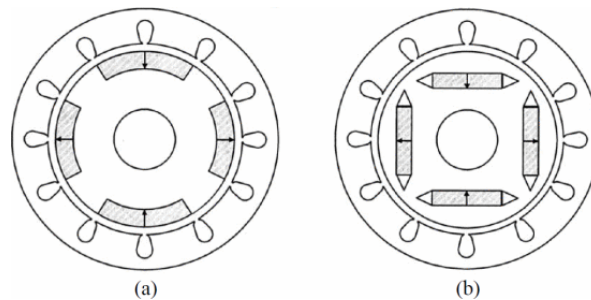
Fig.1.6. PMSM topologies: (a) Surface-mounted magnet motors, (b) Interior magnet motors [6]

The surface-mounted PM topology is easier to design, while the interior PM topology incorporates reluctance torque (the torque generated by the asymmetry of the magnetic circuit in the horizontal and axial axes). Its presence enhances both torque and flux-weakening performance, allowing for a reduction in the PM volume and, consequently, cost [8].

1.3 Special Structures of Traction Motors in EVs-Axial Flux Permanent Magnet Machines (AFPMs)

Frequently, Permanent Magnet Motors in electric vehicle applications are positioned within the wheels to provide direct propulsion. In such instances, these vehicles are referred to as either direct-drive EVs or in-wheel [9].

Direct-drive machines impose stringent requirements on the axial length of electric motors. This configuration has given rise to a new category of electric motors known as Axial Flux Motors [10]. In these motors, the magnetic flux lines run parallel to the axis of rotation, unlike conventional radial flux motors where the magnetic flux is perpendicular to the axis of rotation as can be shown in Fig.1.7.
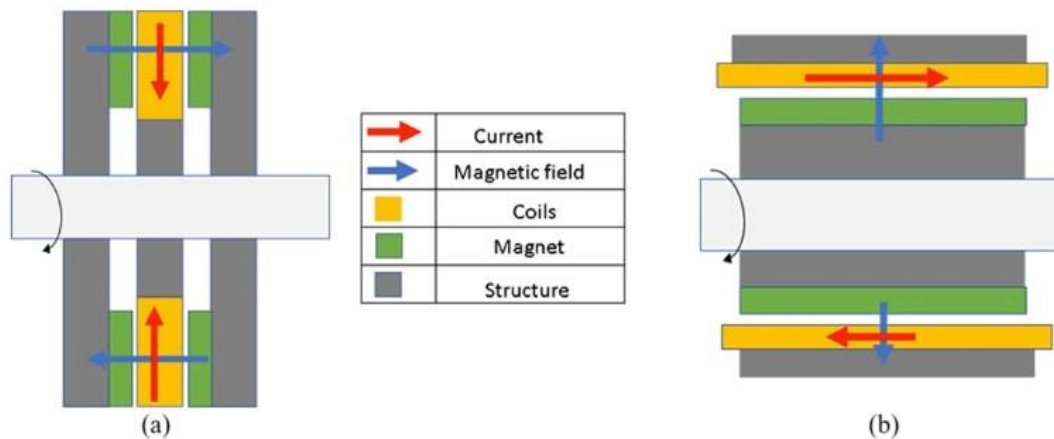
Fig.1.7. Magnetic Field Orientation: (a) Axial Flux, (b) Radial Flux [18]

Axial-flux (AF) permanent-magnet (PM) machines, commonly called AFPM machines, have become a focal point in the automotive industry owing to their impressive attributes: high torque density, elevated efficiency, and a compact structure. Particularly well-suited for high-power density applications where considerations of space and weight are paramount, AFPM machines offer distinct advantages. They require a smaller volume compared to Radial-Flux Permanent Magnet (RFPM) machines, and the significant reduction in the rotor's moment of

inertia makes them especially fitting for applications requiring rapid acceleration and deceleration, such as in the case of racing cars. This makes AFPM machines an ideal choice for addressing the stringent requirements of the automotive sector.

There are two types of AFPM machines the external-stator internal rotor-type (AFIR) and external-rotor internal stator type (TORUS).

1.3.1 Axial Flux Permanent Magner Synchronous Machines

The category of Permanent Magnet Synchronous Motors (PMSM) includes double-sided Axial Flux Permanent Magnet (AFPM) machines with an external-rotor internal-stator configuration, referred to as TORUS (Fig.1.8). In TORUS, magnets on opposing disks can be arranged either in N-N or N-S configurations. The N-S arrangement allows for the removal of the stator back core, resulting in decreased axial length, diminished iron losses, and an amplified power density and efficiency. Conversely, the TORUS N-N topology retains a relatively substantial stator back core to manage the magnetic flux originating from the external rotors.
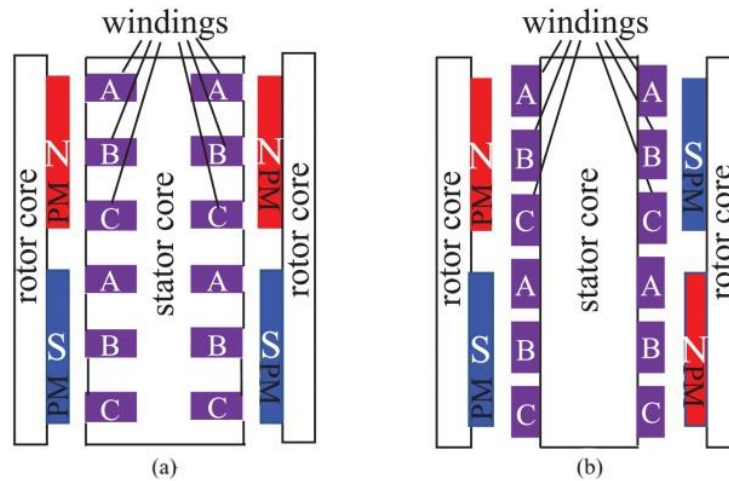
Fig.1.8. AFPM machines TORUS topology: (a) Slotted stator N-N PM TORUS, (b) Slotless stator N-S PM TORUS [10]

1.3.2 Axial Flux Induction Machines – AFIR

Moreover, there are induction motor (IM) topologies that incorporate permanent magnets on the rotor's core, falling under the category of Axial Flux Permanent Magnet (AFPM) machines. These include the external-stator internal-rotor type, characterized by two external stators and an internal rotor, referred to as (AFIR). Concerning the presence of stator slots, they are classified into two categories as shown in Fig.1.9.
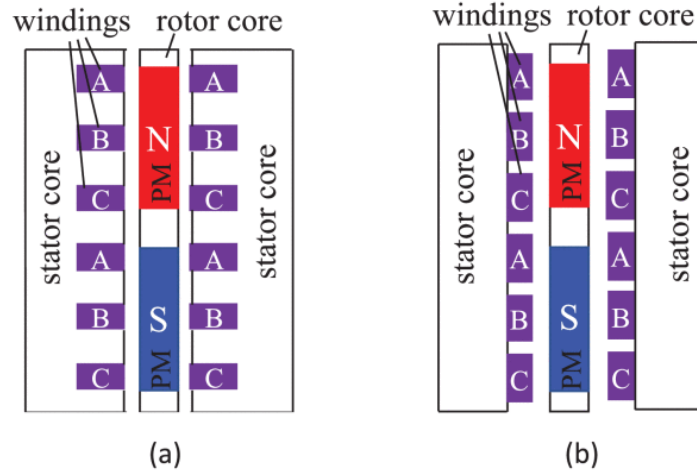
Fig.1.9. AFPM machines AFIR topology: (a) Slotted stator AFIR, (b) Slotless stator AFIR [10]

Both Axial Flux Permanent Magnet (AFPM) machines are well-suited for high-performance drive applications due to their high torque-to-weight ratio and efficiency, showcasing superior power density compared to traditional induction machines. Unlike the AFIR geometry, which utilizes copper exclusively on one surface, the TORUS-type configuration employs copper for torque production on both surfaces of the stator. Consequently, the end windings in the TORUS machine display reduced length compared to the AFIR geometry, resulting in a significant improvement in machine efficiency. Additionally, as outlined in [19], the TORUS topology demonstrates higher power density under conditions of high current density and low electric loading, whereas the AFIR topology excels in conditions of low current density and high electric loading.

1.3.3 Yokeless And Segmented Armature (YASA)

Eliminating the stator yoke from the TORUS N-S type structure and incorporating tooth-wound concentrated windings (CWs) for a segmented stator construction result in the Yokeless And Segmented Armature (YASA) AFPM machine topology (Fig.1.10) [11],[12]. YASA motors are gaining increasing prominence due to their high torque density, compact structure, and low weight, rendering them appropriate for the automotive industry.

Fig.1.10. YASA topology [10]

The coreless design involves the removal of iron from either the stator or rotor, effectively reducing axial length, cutting down on weight, and eliminating core losses and cogging torque (the torque results from the magnetic force between the rotor magnets and the iron teeth of the stator). This leads to a significant increase in torque density and efficiency. Despite these advantages, the coreless geometry places the windings or PMs in the air gap, exposing them directly to magnetic flux. This configuration results in elevated AC copper losses, an increased risk of irreversible PM demagnetization, and an exceptionally low machine inductance, consequently leading to a narrow constant power range.

1.4 Scope

Less work has been performed on the experimental modelling of the actual components with increased complexity to allow for accurate predictions and take into account most real phenomena and manufacturing characteristics. However, such modelling is required to explain data obtained by experimental testing.

In this thesis, an experimentally derived complex model of stator poles, including mounted windings of Permanent Magnet Synchronous Motors (PMSMs), is utilized to facilitate the analysis of data obtained from various accelerated aging processes. Specifically, the study aims to investigate the effects of multistress, encompassing thermomechanical stress induced by thermal cycling, fixed thermal stress, and mechanical stress. The ultimate goal is to evaluate the effectiveness of the impedance spectroscopy method as a sensitive and reliable method for insulation health assessment.

1.5   Outline

Chapter 1 - Traction Motors for Electric Vehicles: Introduces the objectives and scope of the Thesis.

Chapter 2 - Faults in Permanent Magnet Synchronous Motors (PMSMs): Discusses the various types of stresses, collectively known as TEAM (Thermal, Electrical, Ambient, Mechanical) experienced by PMSMs, examines the faults induced by TEAM stresses, explores existing condition monitoring methods for fault diagnosis, and outlines ongoing efforts in the field of prognosis.

Chapter 3 - State of the Art on Electrical Insulation Ageing: Presents an overview of insulation materials used in electric machines, followed by an examination of various diagnostic tools available in the literature for monitoring the condition of insulation, which is influenced by TEAM stresses.

Chapter 4 - Equivalent Model Development and Prognosis-Diagnosis via FRA: Describes the process of developing an equivalent model of the poles under study based on experimental measurements to determine circuit parameters. Verification of model reliability is conducted via impedance spectroscopy and Nyquist diagram comparison with samples of healthy poles. Upon demonstrating model reliability, parameter adjustments are made based on literature review, and frequency response analysis (FRA) is conducted to observe pole behavior during the Multistress process, enabling both diagnosis and prognosis.

Chapter 5 - Experimental Multifactor Ageing: Details the experiments conducted in this thesis, recording their results using impedance spectroscopy, Nyquist diagram, and dissipation factor analysis, and interprets these findings based on the developed model. Additionally, offers recommendations for future research.

Chapter 2: Faults in Permanent Magnet Synchronous Motors (PMSMs)

This Chapter Explores Stress Factors Encountered by Electric Machines (Section 2.1), Proceeding with an Analysis of Errors Arising from These Stresses (Section 2.2). Subsequently, Techniques for Condition Monitoring and Diagnostics will be Investigated to Assess Machine Health via Fault Signatures (Section 2.3). Finally, Existing Literature Efforts in Developing Fault Prognosis Methods will be Discussed (Section 2.4).

2.1 Aging Stresses [20],[21]

In automotive applications, electric machines are designed to be lightweight and small, with the goal of increasing torque and power-to-volume ratio. However, these desirable features frequently imply a reduction in the quantity of copper, steel, and insulation used in the motor. Consequently, the motor becomes subjected to substantial stresses, significantly impacting the insulation's lifespan. These stresses further exacerbate the degradation and ageing of motor components, potentially resulting in unforeseen catastrophic failures. These stress factors are classified as TEAM (Thermal, Electrical, Ambient, and Mechanical) stress, each of which will be detailed in subsequent sections.

2.1.1 Thermal Stress

This is the typical cause of insulation degradation and the reason for the ultimate failure in electric machines. Therefore, the design of a winding insulation system must be designed considering its behavior when subjected to thermal stress. When the operating temperature rises significantly due to the I^2R losses in the copper and exceeds the insulation material threshold, a chemical reaction known as oxidation occurs [22]. The oxidation process results in increased fragility in the insulation system, potentially causing delamination of the groundwall. The groundwall is the insulation that separates the copper conductors from the grounded core of the stator. Delamination refers to the separation of groundwall layers, either due to a reduction in bonding strength or the failure of the impregnating mesh.

Thermal lifetime is approximated by the Arrhenius rate low [23] given by Eq.2.1:

$$L = Ae^{\frac{B}{T}} \qquad \text{(Eq.2.1)}$$

where L is the life of insulation in hours, A, and B, are the material constants and T is the temperature in Kelvin. It is noteworthy that below a threshold temperature, which depends on the insulation material used, thermal stress does not occur. Nevertheless, as the temperature increases, the lifetime decreases.

Since in the automotive industry, the motors used have a compact size and low weight, their peak power exceeds their rated power frequently. Furthermore, due to continuous starting and stopping procedures, they undergo rapid temperature fluctuations during their operation. They may perform under full load with elevated temperatures for a few hours and then with no load at low temperatures. Hence, their winding temperatures follow a cycle between extremely high and low temperatures. This type of Thermal Stress is called Thermal Cycling [24] and it may have noteworthy implications in the insulation system.

Thermal Cycling leads to insulation deterioration due to different expansion coefficients of copper and insulation. As mentioned earlier, the primary source of heat is the I^2R losses that occur in copper, causing it to heat up faster than the insulation. Consequently, when the machine is quickly subjected to operate under full load, the copper expands to a greater extent than the insulation in the axial direction. This results in the so-called shear stress between the copper and groundwall insulation, posing a risk to their bond, and potentially leading to delamination in the insulation. The possible occurrence of delamination creates air gaps in the insulation, which can lead to partial discharges causing erosion in the insulation.

2.1.2 Electrical Stress

Power frequency electrical stress may contribute to the ageing of the insulation if Partial Discharges (PDs) are displayed. PDs are small electric sparks that appear either within the air pockets or on the surface of the insulation, assaulting the insulation and leading to the breakdown of the chemical bonds of the organic elements within the insulation. Over time, PDs are likely to cause holes in the insulation of the organic elements comprising the groundwall, leading to serious faults.

The impact of stress level on the insulation life is represented by the inverse power model (Eq.2.2):

$$L = cE^{-n} \qquad \text{(Eq.2.2)}$$

where the life of insulation in hours denoted as L, is determined by the material constant c, the electrical stress inside the insulation material E (measured in kilovolt/millimetre), and the power low constant n. The power low constant varies between 9 and 12 for the insulation materials used in electric machines. In case the parameter E assumes a value fluctuating between 10 and 20, then in combination with the value of n it will result in a reduction in the insulation lifespan on the order of thousands. Moreover, n can be considered constant for a specific material leading to the development of an exponential model for the insulation lifespan (Eq.2.3):

$$L = ae^{bE} \qquad \text{(Eq.2.3)}$$

where a, and b are constants.

When the applied electrical stress does not exceed a certain threshold called the partial discharge extinction voltage (DEV), ageing phenomena do not occur. Thus, (Eq.2.3) can be alternatively expressed as follows, taking into account the DEV (Eq.2.4):

$$L = c(\bar{E} - E_0)^{-n} \qquad \text{(Eq.2.4)}$$

where E_0 is the threshold that specifies the existence of ageing.

Electrical stress ageing can occur when multiple repetitive voltage surges are applied across the turn insulation in random-wound stators of synchronous or induction machines. These surges are often generated by inverter-fed drives (IFDs) employing electronic switching devices with pulse width modulation technologies (PWM).

In the case of random-wound machines, these pulses during inverter-fed operation can induce the occurrence of Partial Discharges (PDs) [25],[26], even though the nominal operating voltage of these machines is low (440V), leading to insulation deterioration. Moreover, it is possible that voltage surges may not cause PDs. In this case, the electron emission, caused by the unbalanced surface of the copper, will break the chemical bonds of the insulation, resulting in its corrosion.

As for the windings of modern machines, the electric stress occurs through PDs generated by voltage surges produced by an excitation system that utilizes electronic switches.

2.1.3 Ambient Stress

Ambient stress can be induced by various environmental elements surrounding the motor, such as chemicals, humidity levels, moisture, abrasive particles in cooling air, dirt, debris, and oil from the bearings. Often, these factors act in conjunction with other stresses to induce ageing effects. For instance, certain chemicals like ozone and acids have been observed to degrade insulation and diminish its mechanical strength. Additionally, the combination of moisture, oil, and dirt can deform the insulation to make it partially conductive, allowing electric stress to generate currents on its surface. Furthermore, the presence of oil, moisture, and dirt in the stator and rotor poses a risk of disrupting the cooling system, leading to thermal stress and consequent insulation deterioration.

Ambient stress may indeed impact the ageing of the machine and should be considered a significant factor in its deterioration. However, establishing a clear relationship demonstrating its contribution to ageing can be challenging.

2.1.4 Mechanical Stress

In automotive motor applications, two primary sources of mechanical stress exist, yet an analytical equation linking their influence on insulation lifespan remains elusive. The first source originates from their lightweight and compact design, enabling higher rotational speeds without compromising power delivery. Consequently, the rotors endure significant centrifugal forces, posing a risk of insulation corrosion or damage.

The second source of mechanical stress is caused by the application of power frequency current to the windings, leading to their bending and compression. Consequently, the windings, slot wedges, and inter-windings will loosen, the magnetic force will make them vibrate at twice the power frequency (Eq.2.5), and the insulation of the groundwall will deteriorate. Beyond windings, vibration can also be observed in cases where the machine is composed of permanent magnets. In such instances, it can lead to the demagnetization of these magnets, causing severe damage.

$$F = \frac{cI^2}{d}\left(\frac{kN}{m}\right)$$

$$I = A\sin\omega t$$

$$F = \frac{cA^2(1-\cos2\omega t)}{2d}\left(\frac{kN}{m}\right) \qquad\qquad (Eq.2.5)$$

where *c*: constant, *d*: width of stator slot, *t*: time

In the case of water-cooled machines, vibrations and other types of mechanical stress can either lead to coolant leakage or induce a chemical reaction between water ions and material insulation (hydrolysis), potentially leading to the decay of the insulation.

Moreover, the mechanical stresses exerted on the bearings of high-speed rotating engines in Electric Vehicles (EVs), combined with the development of high temperatures, result in electrical discharges. These discharges are responsible for the formation of cracks, holes, and ignition on the surface of the bearing, leading to bearing failure.

2.1.5 Multi-factor Stress

This type of stress constitutes a combination of two or more individual stresses discussed earlier. Through this method, the ageing of insulation occurs at a much faster rate. However, in this case, developing a mathematical model that describes the insulation's lifespan as a function of multistress becomes highly complex, if not impossible.

2.1.6 Accelerated Aging Test

Accelerated testing involves applying two or more stresses to hasten the ageing process, thereby minimizing the time to failure. This shortened timeframe is crucial for swift advancements in insulation systems, as waiting 15-20 years for a component to fail before redesigning becomes impractical. Detailed implementations of such testing methodologies found in the literature will be comprehensively presented in Section 3.2.

2.2 Faults in PMSMs

The diverse array of stresses outlined in Section 2.1 significantly contributes to the degradation and ageing of Permanent Magnet Synchronous Motors (PMSMs),

potentially resulting in faults and, in the worst-case scenario, triggering unexpected catastrophic failures.

Faults in PM machines can be categorized into two types (Fig.2.1), as indicated by [27]-[29]: rotor-related faults and stator-related faults. Rotor faults encompass magnetic demagnetization, bearing faults, eccentricity, and unbalanced magnetic pull (UMP), which are collectively referred to as both magnetic and mechanical faults. Stator-related faults, alternatively known as electric faults, are associated with winding faults.
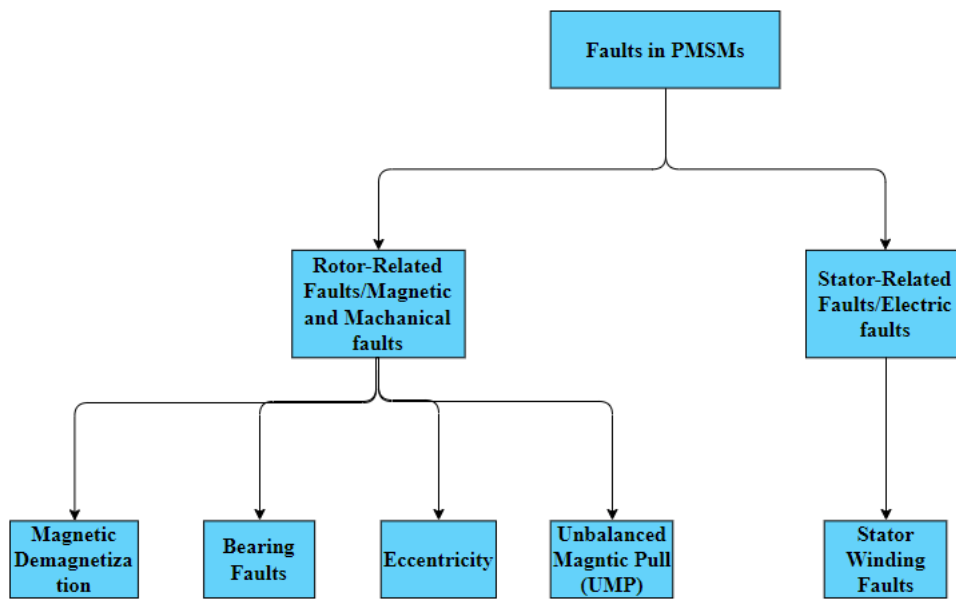
Fig.2.1: Faults in PMSMs

2.2.1 Magnetic and Mechanical Faults

2.2.1.1 Magnetic Damage & Demagnetization

PMs are the most crucial component of Permanent Magnet Synchronous Motors (PMSMs) and simultaneously the main cause of faults, as the PMs may get damaged and irreversible demagnetized. Such faults may arise from various factors such as corrosion, manufacturing cracks, electrical stress, thermal stress, and mechanical stress.

In Fig.2.2, a typical demagnetization characteristic can be observed [30]. If the operating point of the magnetic material is located below the knee point K, even if the external demagnetization field H_a is reduced or removed, the operating point can't reach its original B-H characteristic and will follow the recoil line L_a. As long as the

value of the external demagnetization field does not exceed the value of H_a, then the operating point of the magnetic material continues to coincide with the recoil line L_a. However, in the case where an external demagnetizing field H_b higher than H_a is applied, then again, the operating point of the magnetic material will change, and there will be a lower knee point b as well as a new recoil line b. Thus, the change in the operating point leads to the elimination of the previous demagnetization curves, indicating that a strong external electric field may cause the irreversible demagnetization of PM. This electric field may be caused by a high short circuit current.
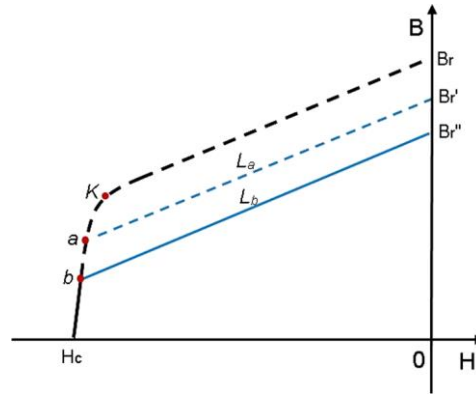
Fig.2.2. Irreversible demagnetization due to working point below knee point [30]

In Fig.2.3, it can be concluded that the demagnetization curves are very sensitive to the rise in temperature. As the temperature increases, the region surrounded by the B-H curve becomes smaller, and when the temperature significantly rises, the irreversible demagnetization of the PM is highly probable.
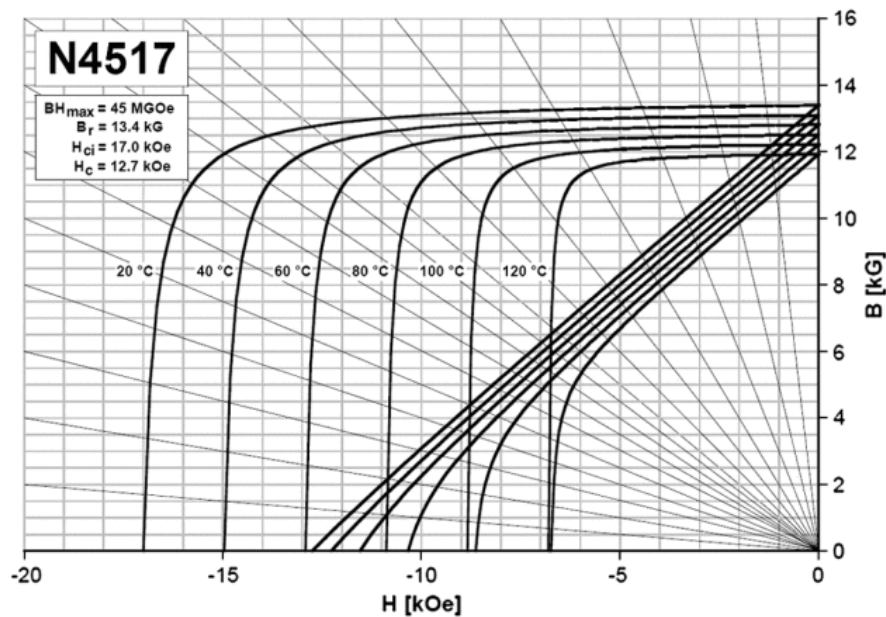
Fig.2.3. Effect of temperature on the B-H characteristic of a PM material [30]

When demagnetization occurs, it may lead to diminished or imbalanced rotor flux, overloads, vibration, and rotor faults. It also may hurt the performance efficiency and reliability of the machine. Thus, it is imperative to conduct condition monitoring for Permanent Magnets (PMs) to ensure the anticipated efficiency and reliability.

2.2.1.2 Bearing Faults

According to Fig.2.5, bearing faults (rolling and sliding) account for 41% of faults in low-voltage AC machines and 13% in high-voltage. They primarily result from improper motor assembly, inadequate lubrication, motor overloading, and ageing. These faults may lead to eccentricity failure of the motor.

2.2.1.3 Eccentricity

In a healthy machine, the rotor aligns centrally with the stator core, and the rotor's center of rotation aligns with the stator core's geometric center. Eccentricity results from the uneven gap between the rotor and stator. It can be categorized into three types: Static, Dynamic, and Mixed. Static eccentricity (SE) occurs when the axes of rotation of the rotor and stator do not align, and the rotor rotates in a fixed position within the motor around its center. In this case, air gap uniformity is disturbed but it doesn't change during the rotor's rotation. Dynamic eccentricity (DE) occurs when the centers of the stator and rotor are aligned, but the rotor does not rotate around its center. Air gap uniformity is also disturbed here but changes as the rotor rotates. Mixed eccentricity (ME) is the existence of static and dynamic simultaneously.

In Fig.2.4, different types of eccentricity are illustrated in the cross sections of the stator and rotor. O_s represents the symmetry centre of the stator, O_ω is the symmetry center of the rotor, and O_r indicates the rotation centre of the rotor. β_s is the initial angle of static eccentricity (SE), β_d is the initial angle of dynamic eccentricity (DE), β_m is the transfer angle of ME, and θ is the mechanical angle of the motor.

In SE illustrated in Fig.2.4a, it is noticeable that O_ω does not align with O_s, signifying that the position of the minimum air gap length remains constant in space. Consequently, the SE ratio δ_s (Eq.2.6) remains constant for all angular positions of the rotor.

$$\delta_S = \frac{|O_S O_\omega|}{g} \qquad \text{(Eq.2.6)}$$

where g represents the uniform air gap length, and O_s, O_ω the static transfer vectors.

For DE as depicted in Fig.2.4b, O_s aligns with O_ω, yet the rotor does not rotate around O_ω; instead, the minimum air gap moves along with the rotor. Consequently, the DE ratio δ_d (Eq.2.7) remains constant for all angular positions of the rotor, but its angle changes.

$$\delta_d = \frac{|\boldsymbol{O_\omega O_r}|}{g} \qquad \text{(Eq.2.7)}$$

where g represents the uniform air gap length, and $\boldsymbol{O_\omega}$, $\boldsymbol{O_r}$ the static transfer vectors.

In the case of ME as shown in Fig.2.4c, which is a combination of SE and DE, the ME ratio is given by Eq.2.8:

$$\begin{cases} \delta_m = \frac{|\boldsymbol{O_s O_r}|}{g} = \frac{|\boldsymbol{O_s O_\omega}|}{g} + \frac{|\boldsymbol{O_\omega O_r}|}{g} = \sqrt{\delta_s{}^2 + \delta_d{}^2 + 2\delta_s\delta_d cos\theta} \\ \beta_m = tan^{-1}\frac{\delta_d sin\theta}{\delta_s + \delta_d cos\theta\sigma} \end{cases} \qquad \text{(Eq.2.8)}$$

The minimum air gap length g in this case is related to θ and is given by Eq.2.9:

$$g(t) = r_s - \delta_m g cos\left(\frac{\omega t}{p} - \beta_m\right) - \sqrt{r_r{}^2 - \delta_m^2 g^2 sin\left(\frac{\omega t}{p} - \beta_m\right)} \qquad \text{(Eq.2.9)}$$

where $g(t)$ represents the air gap length, r_s is the stator radius, r_r is the rotor radius, p denotes the pole pair number, and ω stands for the supply frequency.
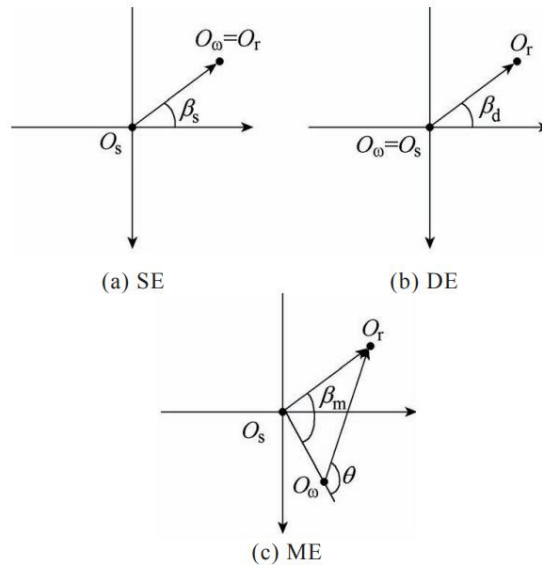
Fig.2.4: Stator and rotor cross-section positions [31]

The presence of eccentricity can lead to uneven radial forces between the stator and rotor. This phenomenon is referred to as unbalanced magnetic pull (UMP). UMP may lead to friction phenomena between the stator and rotor, which can cause damage

to the motor assembly. Its existence can lead to high vibrations, audible noise, and damage to bearings.

2.2.1.4 Unbalance Magnetic Pull (UMP)

UMP can be induced either by the presence of eccentricity or non-uniform magnetization of the PMs. In most machines, the occurrence of these phenomena is unfortunately inevitable, so UMP always manifests to some extent. Its existence can lead to high vibrations, audible noise, and damage to bearings. Hence, it is necessary to take into consideration the existence of UMP both in the machine design process and in condition monitoring.

2.2.2 Electrical faults-Stator Winding Faults

Stator winding faults are among the most prevalent causes of failures in AC motors, accounting for between 36% and 66% of all failures, as illustrated in Fig.2.5. These faults in PMSMs are mainly short circuits caused by insulation damage [29], [32]. Insulation damage occurs due to factors such as abrasion or overheating of the winding caused by electrical or mechanical stress and excessive motor loads. This type of damage is highly destructive, starting with an inter-turn short circuit (ITSC) in adjacent turns of the windings. This initial fault can rapidly lead to damage in subsequent coils, potentially evolving into a phase-to-phase or phase-to-ground short circuit.

Consequently, ITSCs can result in motor failure and emergency shutdown. Repair or replacement of the damaged machine is then necessary, incurring high costs. Thus, this type of fault is particularly critical for electric vehicle applications, as it may compromise human safety. Detecting inter-turn short circuits at an early stage is crucial to prevent the fault from spreading and ultimately causing the machine to fail. However, identifying ITSCs is considered extremely challenging, as detection is only feasible at an initial stage where the potential for preventing the entire phase or winding is still possible. Additionally, it is noteworthy that the inter-turn short circuits may cause irreversible demagnetization of the PMs.

Fig.2.5: AC machine failures [29] (a) low-voltage, (b) high-voltage

2.3 Condition Monitoring & Fault Diagnosis

Condition Monitoring is a process that involves monitoring the operational parameters of a physical system. By analysing changes in these parameters, potential failures in the system can be identified. There are two primary categorie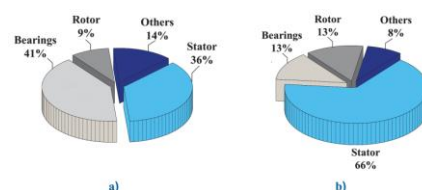s of Condition monitoring: Offline and Online. Offline Condition Monitoring necessitates taking the machine out of service for inspection, while Online Condition Monitoring is conducted during machine operation.

Online monitoring boasts several advantages over offline methods. Firstly, it mitigates the loss of electrical energy production and reduces machine inspection costs by eliminating the need to halt machine operation. Moreover, online monitoring allows for a more detailed examination of the machine's condition. Lastly, it enables the use of appropriate alarms to notify maintenance personnel when an issue occurs [33].

By utilizing data obtained through condition monitoring, fault diagnosis is carried out to detect, locate, and identify faults, while also monitoring the development of faults from defects to failures. Accurate condition monitoring and fault detection at an early stage, can significantly decrease unscheduled machine downtime, reduce expensive repair costs, and enhance production efficiency. Signals, such as phase currents and voltages, speed, torque, noise, flux density, acoustic emission, and vibration, are investigated for their frequency components [34]. The section that follows provides a description of the condition monitoring and fault diagnosis methods found in the literature.

Fault detection can be classified into three categories: time-domain analysis, frequency-domain analysis, and time-frequency analysis [35], [36].

- Time-domain methods primarily rely on statistical analysis, utilizing signal parameters such as peak values, RMS, or mean values etc.

- Frequency-domain analysis methods will be analysed in the present master thesis. This analysis involves sampling the signal and applying the Fast Fourier Transform (FFT) algorithm. The resulting frequency resolution, at a fixed sampling frequency F_s, is inversely proportional to the time acquisition period T_w, representing the available duration of the signal. It becomes evident that achieving either high-time resolution or high-frequency resolution is feasible through FFT. Consequently, Fourier analysis is inherently tied to steady-state operation. The widely adopted

diagnostic method known as machine current signature analysis (MCSA) has experienced considerable growth, attributed in part to its straightforward implementation.

In classical Fourier analysis, signal power can be determined by integrating the Power Spectral Density (PSD), calculated as the square of the absolute value of the Fourier-transform coefficients. Unlike classical MCSA proposals, PSD studies focus on faulty frequency bands, eliminating the need to concentrate fault detection on a specific fault signature.

- Time-frequency analysis presents a thorough representation of a signal, encapsulating 3-D aspects of time, frequency, and amplitude to effectively unveil transient effects within the signal. The Wigner distribution stands out as a widely employed time-frequency analysis technique, alongside additional methods such as the wavelet transform and the Hilbert–Huang transform, contributing to the diverse array of approaches in signal analysis.

2.3.1 Demagnetization Fault Detection

Multiple signals are used for the detection of demagnetization faults, such as stator current, zero sequence and current components, back electromotive force, axial flux, vibration, noise, and torque. In Table 2.1, the methods for processing these signals are summarized, describing how they recognize demagnetization faults. Moreover, Table 2.1 encompasses fault signatures (where applicable), denoting the harmonics associated with the respective type of fault. The table also provides a comparison of the positive and negative aspects exhibited by each method.

Diagnostic Signal	Method	Description	Fault Signature	Advantages	Disadvantages
Stator Current	FFT	According to MCSA, the presence of a demagnetization fault is indicated by an observed increase in the amplitude of harmonics as defined in *Eq. 2.10*.	$f_{demag} = f_s(1 \pm \frac{k}{p})$ k=1,3, 5... (Eq.2.10)	• Non-invasive • Partial Demagnetization fault can be detected • Online	• Steady-state Condition is required • Influenced by other faults • Low or medium sensitivity
Zero sequence current component (ZSCC)	FFT	The (ZSCC) is given by $i_{zsc} = i_a + i_b + i_c$ where i_a, i_b, i_c are phase currents. The demagnetization fault can be detected by the fault severity index k which is given by: $k = \frac{I_{V(faulty)}}{I_{V(healthy)}}$ In healthy conditions, k equals 1, while in the case of demagnetization faults, k is different from 1. This indicator is calculated for ν=3, representing the third harmonic [37].		• Partial Demagnetization fault can be detected • Uniform Demagnetization faults can be detected • Online • High sensitivity	• Steady-state Condition is required • Invasive • Influenced by other faults
Zero sequence voltage component (ZSVC)	FFT	The fundamental fault degree in the ZSVC method is given by: $V_{0,m} = -k\frac{d\lambda_{pm}}{dt}$ where k is the demagnetization degree and λ_{pm} the phase flux linkage. In healthy machines k=1. In the case of demagnetization ZSVC phase voltage is reduced as the faulty degree k is heightened [38].		• Partial Demagnetization fault can be detected • Online • High Sensitivity	• Invasive • Steady-state Condition is required • Influenced by other faults
back electromotive force (bemf)	FFT	The appearance of a demagnetization fault diminishes the back electromotive force (bemf). Due to the demagnetization fault, the number of effective PMs is lower than the total number of PMs in the machine [38]		• Partial Demagnetization fault can be detected • Non-invasive	• Steady-state Condition is required • Offline • Medium Sensitivity
Axial flux	FFT	Fluxgate sensors effectively monitor the leakage flux		• Partial Demagnetization	• Steady-state Condition is required

		surrounding permanent magnet synchronous motors. The flux spectra of electric machines encompass crucial information for the monitoring and characterization of magnet defects, providing direct insights into fault identification and the progression of these faults.		• fault can be detected • Uniform Demagnetization faults can be detected • Online • Not influenced by other faults • High Sensitivity	• Invasive • Additional coils are necessary for measurements
Vibration	FFT	Vibration signals, acquired through the use of vibration equipment (sensors), undergo FFT transformation for the detection of demagnetization faults. This involves comparing the resulting spectrum with the corresponding spectrum of the machine under healthy operating conditions.		• Partial Demagnetization fault can be detected • Non-invasive • Online • Not influenced by other faults	• Steady-state Condition is required • Vibration and Noise Equipment are required • Medium Sensitivity
Acoustic noise and torque	FFT	Demagnetization faults tend to modify noise and torque signals. Therefore, it is crucial to measure these signals using sensors and subject them to FFT analysis to observe the harmonic content of these quantities.		• Partial Demagnetization fault can be detected • Non-invasive • Online • Not influenced by other faults	• Steady-state Condition is required • Vibration and Noise Equipment are required • Medium Sensitivity

Table 2.1: Frequency Domain methods for detecting Unbalanced Magnetic Pull [29]

2.3.2 Unbalanced Magnetic Pull (UMP) Detection

Analytical models presented in [39] offer assistance in identifying the origins of Unbalanced Magnetic Pull (UMP), such as rotor eccentricity, and quantifying vibration frequencies. Rotor eccentricity alters air-gap permeance, introducing extra harmonics into the air-gap flux patterns generated by rotor magnets and stator winding currents. Consequently, UMP can be represented by aligning harmonics within these modified air-gap flux patterns.

2.3.3 Bearing Fault Detection

Various signals, such as mechanical vibration, noise, stray magnetic flux, rotational speed, and stator current, can be used to measure bearing faults. A comprehensive overview of the different methods employed for detecting bearing faults is presented in Table 2.2.

Diagnostic Signal	Method	Description	Fault Index	Advantages	Disadvantages
Stator Current	FFT	FFT analysis is carried out on the stator current, and through Motor Current Signature Analysis (MCSA), the harmonics specified by *Eq.2.11* reveal the appearance of eccentricity.	$f_b = f_s \pm k f_u$ (Eq.2.11) f_u: Characteristic damage frequency of the bearing $$\begin{cases} f_{bc} = \frac{1}{2} f_r \left(1 - \frac{D_b}{D_c} cos\beta\right) \\ f_{or} = \frac{N_b}{2} f_r \left(1 - \frac{D_b}{D_c} cos\beta\right) \\ f_{ir} = \frac{N_b}{2} f_r \left(1 + \frac{D_b}{D_c} cos\beta\right) \\ f_{re} = \frac{D_c}{D_b} f_r (1 - (\frac{D_b}{D_c} cos\beta) \end{cases}$$ (Eq.2.12) where f_r: rotational frequency, $k = 1,2,3,..$, N_b represents the number of rolling elements, D_b denotes the diameter of the rolling element, D_c signifies the bearing pitch diameter, β represents the working angle of the bearing, and f_{bc}, f_{or}, f_{ir}, and f_{re} denote the frequencies associated with specific failures, namely, bearing cage, outer race, inner race, and rolling element.	• Non-invasive • Aging in process of lubricated bearing can be detected • High Sensitivity	• Sensitive to low speed and torque variations, • Only one type of bearing damage can be detected • Only simulation is used • Steady-state Condition is required
Stator Current – Extended Park's Vector Analysis (EPVA)	FFT	The components of stator current are given by: i_α $= \sqrt{\frac{2}{3}} i_a - \sqrt{\frac{1}{6}} i_b$ $- \sqrt{\frac{1}{6}} i_c$ $i_\beta = \sqrt{\frac{1}{2}} i_b - \sqrt{\frac{1}{2}} i_c$ where i_a, i_b, i_c are the phase currents. In healthy machines, the components of the Park's vector form a circle, but in the	$k f_u$ (Eq.2.13) $k = 1,2,3,..$, f_u: Characteristic damage frequency of the bearing (Eq.2.12)	• Development of an Electromechanical model for fault detection in rolling bearings.	• Only simulation is used

		presence of a fault, the Park vector transforms into an elliptical shape [40]. The fault index of EPVA is given by *Eq.2.13*			
Vibration	FFT	An FFT analysis is conducted on vibration signals collected from sensors, and the harmonics specified by *Eq.2.14* are examined to detect bearing faults.	$f_b = kf_u \pm lf_r$ $k = 1,2,3,$ and $l = 0,1$ (Eq.2.14) f_u: Characteristic damage frequency of the bearing (Eq.2.12) f_r: rotational frequency	• Non-invasive • Robust to variations in load torque and speed • aging in the process of lubricated bearing, and mechanical damage can be detected • High Sensitivity	• Steady-state condition is required • Vibration and Noise equipment for measurement are required
Stray Magnetic Flux		The stray flux refers to the magnetic field lines extending beyond the core body of the stator. Monitoring the stray flux around the motor is achieved using a fluxgate sensor located on the housing [41]. The frequencies associated with bearing faults are determined by *Eq.2.15*.	$f_{bf} = |kf_s \pm mf_u|$ (Eq.2.15) where f_s: supply frequency, k, and m: harmonic order, and f_u: Characteristic damage frequency of the bearing (Eq.2.16)	• Non-invasive • Robust to variation in load torque and speed • Capable of detecting magnetic asymmetry • Mechanical damage can be detected • Provides more information compared to the current analysis	• Only one type of bearing damage can be detected • Additional coils are necessary for measurements
Rotation Speed, Vibration & Stator Current	FFT	In this approach, a comparative analysis is conducted between speed and current signals, with the vibration method serving as a reference. The frequencies indicative of bearing faults align with the values defined in *Eq.2.16*.	kf_u (Eq.2.16) where $k = 1,2,3..,$ f_u: Characteristic damage frequency of the bearing (Eq.2.16)	• Mechanical damage can be detected • Broad speed range	• Only one type of bearing damage can be detected • Only one type of bearing damage can be detected • Vibration and Noise equipment for measurement are required

Table 2.2: Frequency Domain methods for detecting bearing faults in PMSMs [29]

2.3.4 Eccentricity Detection

The assessment of the type of eccentricity is primarily conducted using the stator current with the application of FFT or PSD. Nevertheless, other signals such as stator voltage, mechanical vibrations, noise, rotation speed, load torque, and airgap flux are also employed for eccentricity detection. In Table 2.3, all detection methods based on the aforementioned signals are presented, along with their fault signatures indicating the harmonics associated with eccentricity faults, as well as the advantages and disadvantages of each method.

Diagnostic Signal	Method	Description	Fault Index	Advantages	Disadvantages
Stator Current	FFT	The primary diagnostic signal to detect eccentricity is the stator current through the motor current signature analysis (MCSA) [32]. According to this method by monitoring the stator current the additional frequency components due to eccentricity f_{ecc} are given by *Eq.2.17*. Alternatively, the eccentricity faults are given by *Eq.2.18,* and *Eq.2.19*.	$f_{ecc} = f_s\left(1 \pm \dfrac{2k-1}{p}\right),$ $k = 0,1,2,...$ or 3rd and 5th harmonics (Eq.2.17)	• Non-invasive, • SE, DE, ME	• Steady-State condition required
			$f_{ecc} = f_s\left(1 \pm \dfrac{k}{p}\right),$ $k = 0,1,2, ...,$ p = number of pole pairs, f_s: supply frequency (Eq.2.18)	• Non-invasive, • Not influenced by other faults	• Only DE can be detected, • Steady-State condition required
			$f_s - f_r$ where f_s: supply frequency, f_r: rotational frequency (Eq.2.19)	• Non-invasive	• Only DE can be detected • Steady-State condition required • does not distinguish between errors in DE, Demagnetization, and UMP
	PSD	PSD is performed on the stator current and the harmonic components derived from *Eq.2.20*, *Eq.2.21*, *Eq.2.22* are examined using the MCSA method.	$f_{ecc} = f_s\left(1 \pm \dfrac{l}{p}\right),$ $l = 1,3,5, ... ,$ f_s: supply frequency, p: number of pole pairs (Eq.2.20)	Non-invasive	• Steady-State Condition required • only SE and DE can be detected
			$f_{ecc} = f_s\left(1 \pm \dfrac{2k-1}{p}\right),$ $k = 0,1,2,..,$ f_s: supply frequency, p: number of pole pairs (Eq.2.21)	Non-invasive	• Steady-State Condition required • only SE and DE can be detected
			$f_{mixed} = {2kf_s}/{p}$ f_s: supply frequency, p: number of pole pairs (Eq.2.22)	Non-invasive	• Steady-State Condition required • ME can be detected only at specific loads

Signal	Method	Description	Signature	Invasiveness	Advantages/Disadvantages
Vibration	FFT	Vibration within the motor was observed by installing sensors on the stator yoke, aiming to detect vibration occurring at different levels of eccentricity faults [42]. The harmonics indicating the presence of eccentricity are provided by *Eq.2.23*	$(2pk \pm 1)th\ order,$ $k = 1,2,3..$ p: number of pole pairs (Eq.2.23)	Non-invasive	• SE, DE can only be computed through simulation • DE is detectable only experimentally
Noise	FFT	FFT is applied to the noise signal originating from the sensors, and the resulting noise spectrum is analyzed at frequencies specified in *Eq.2.24.*	$(2pk \pm 1)\ th\ order,$ $k = 1,2,3..$ (Eq.2.24)	Non-invasive	• Only SE, and DE can be detected either through experimental methods or simulation
Voltage	PSD	The PSD of the stator voltage is calculated, and the harmonic content of frequencies given by *Eq.2.25* is analyzed.	$f_{SE} = f_s \pm f_r$ where f_r: rotational frequency, f_s: supply frequency (Eq.2.25)	Non-invasive	• Only SE can be detected
Airgap Flux	FFT	The spectrum of the airgap flux is observed, with particular focus placed on the frequencies outlined in *Eq.2.26.*	3rd and 5th harmonics (Eq.2.26)		• Only DE can be detected • Invasive • Additional Coils are required
Load Torque	PSD	The Power Spectral Density (PSD) of the load torque is computed, and the harmonic content at frequencies specified in *Eq.2.27* is examined.	$f_{SE} = f_s \pm f_r$ where f_r: rotational frequency, f_s: supply frequency (Eq.2.27)		• Only SE can be detected
Rotation Speed	PSD	The PSD of the rotational speed is determined, and the harmonic content at frequencies defined by *Eq.2.28* is analyzed.	$f_{SE} = f_s \pm f_r$ where f_r: rotational frequency, f_s: supply frequency (Eq.2.28)		• Only SE can be detected

Table 2.3: Frequency Domain methods for detecting bearing faults in PMSMs [29]

2.3.5 Winding Fault Detection

Given that winding faults are prevalent in AC machines, various signals can effectively identify them. Table 2.4 presents several methods for detecting winding faults, particularly in their initial stage when they manifest as ITSC faults. It outlines the respective signatures of these methods, along with their associated advantages and disadvantages, as documented in the literature.

Diagnostic Signal	Method	Description	Fault Signature	Advantages	Disadvantages
Stator Current	FFT	The ISTC fault can be detected by an increase in frequencies corresponding to *Eq.2.29*.	• Odd harmonics • $3f_s$ • $f_{ITSC}\left(1 \pm \frac{k}{p}\right)f_s$, $k = 1,3,5,..$ f_s: supply frequency p: number of pole pairs (Eq.2.29)	• Online • Robust to load and speed variations	• Steady-state condition required
	EPVA [43]	The ITSC fault is observed through an increase in the amplitude of second harmonic, as depicted in *Eq.2.30* $$\begin{bmatrix} x_d \\ x_q \end{bmatrix} = \begin{bmatrix} \sqrt{\frac{2}{3}} & -\frac{1}{\sqrt{6}} & -\frac{1}{\sqrt{6}} \\ 0 & \frac{1}{\sqrt{2}} & -\frac{1}{\sqrt{2}} \end{bmatrix} \begin{bmatrix} i_a \\ i_b \\ i_c \end{bmatrix}$$ where the currents i_a, i_b, i_c: are converted to their components x_q, x_d using the equation. The second harmonic amplitude M_2 of d-q currents is: $$M_2 = \sqrt{x_d{}^2 + x_q^2}$$	$2f_s$ f_s: supply frequency (Eq.2.30)		• Steady-state condition required • Measurements of all phase currents necessary
Stator Current Negative Sequence Components	FFT	The negative sequence current [44] is given by $I_{ns} = \frac{i_a + a \cdot i_b + a^2 \cdot i_c}{3}$ where i_a, i_b, i_c phase currents, I_{ns}: negative sequence current, $a = e^{j\frac{2\pi}{3}}$ In the subsequent phase, spectral analysis of the negative sequence current is executed, and the detection of the ITSC fault becomes feasible within the frequencies specified in *Eq.2.31*.	$f_s, 3f_s$ f_s: supply frequency (Eq.2.31)	• Online • Robust to load and speed variations	• Steady-state condition required • The current of the negative sequence current must be calculated
Stator Voltage	FFT	FFT is employed on the stator voltage, and the resulting frequency spectrum is scrutinized, placing particular emphasis on frequencies defined in *Eq.2.32*.	First 14 harmonics (Eq.2.32)	• Online • Robust to load and speed variations	• Steady-State condition required
Stator Voltage Negative Sequence Component	FFT	The negative sequence voltage [45] is given by $V_{ns} = \frac{u_a + a \cdot u_b + a^2 \cdot u_c}{3}$ where u_a, u_b, u_c: phase voltages, I_{ns}: negative sequence current $a = e^{j\frac{2\pi}{3}}$ After this, spectral analysis of the negative sequence voltage is conducted, and the ITSC fault can be identified at the frequency specified in *Eq.2.33*.	f_s f_s: supply frequency (Eq.2.33)	• Online • Robust to load and speed variations	• Steady-State condition required • Voltage of the negative sequence must be required

Zero Sequence voltage component (ZSVC)	FFT	The ZSVC voltage [46] is derived by: $V_O = \frac{1}{3}(V_a + V_b + V_c) + \frac{1}{3}\mu R_s i_f$ $+ \frac{1}{3}\mu(L + 2M)\frac{dI_f}{dt} - \frac{d\lambda_{PM,0}}{dt}$ where $\lambda_{PM,0} = \frac{1}{3}(\lambda_{PM,a} + \lambda_{PM,b} + \lambda_{PM,c})$ $\lambda_{PM,a}, \lambda_{PM,b}, \lambda_{PM,c}$: phase flux due to PMs R_s: resistance between shorted turns V_f: Voltage of the shorted turns i_f: Current in shorted turns $\mu = {}^{n}/_{N}$ where n: number of shorted turns, N: number of total turns per phase M, L: parameters given by the manufacturer Afterwards, the ZSVC spectrum is observed at the frequencies specified in *Eq.2.34*.	$f_s, 5f_s, 7f_s$ f_s: supply frequency (Eq.2.34)	• Online • Robust to load and speed variations	• Steady-state condition required
Rotational Speed	FFT	The rotational speed spectrum is examined according to *Eq.2.35*.	$2f_s$ f_s: supply frequency (Eq.2.35)	• Online • Robust to load and speed variations • Fault localization is possible	• Steady-state condition required
Active and Reactive Power	FFT	The computation of active or reactive power occurs, and the Inter-Turn Short Circuit (ISTC) fault is identified within the harmonic context defined in *Eq.2.36*.	$2f_s$ f_s: supply frequency (Eq.2.36)	• Online • Robust to load variations	• Steady-state condition required • Active and reactive power must be calculated

Table 2.4: Frequency Domain Methods for ITSC detection in PMSMs [29]

2.4 Prognosis [47]

With the increasing use of electric machines and drives in Electric Vehicles (EVs), there is a growing interest in the field of failure prognosis. Prognostics refers to the ability to detect early signs of precursor or incipient faults (very small faults) in a component, along with having the technology and means to effectively manage and predict the progression of these fault conditions leading to component failure. However, the understanding of this term remains diverse.

Frequently, prognosis is associated with the estimation of Remaining Useful Life (RUL) [48]. Given that fault evolution is a stochastic process influenced by factors with potentially unknown future values, determining the exact moment when a component will fail is deemed impossible. Nevertheless, it is feasible to discern an

extrapolated trend of fault evolution or employ a Probability Density Function to estimate the probability of failure over time.

In other cases, prognosis is associated with predicting the future state during the evolution of a fault. For this purpose, algorithms such as the Kalman Filter and Hidden Markov Model are employed to forecast the state, relying on known conditions. When using these algorithms, the state transition matrix is assumed to be constant, which, however, may not align with reality.

Ultimately, prognosis is often linked with identifying small and transient signals. In such instances, the term "prognosis" is employed because the detected faults comprise brief signals that exist for a short duration, signifying the early stages of faults referred to as incipient faults. The fundamental concept is that specific conditions leading to faults result in short-term fluctuations in the currents of electrical motors. However, the detection of transients aligns more closely with the diagnosis category than with the prognosis.

Chapter 3: State of the art on Electrical Insulation Ageing

Chapter 3 begins with an overview of insulation materials utilized in electric machines (Section 3.1), followed by an exploration of diagnostic tools available in the literature for assessing insulation condition (Section 3.2). Section 3.3 will extensively delve into multifactor ageing experiments conducted on the insulation of electric machines.

3.1 Insulation Materials

Insulation materials are essential for the proper functioning of electric machines, providing electrical isolation between conductors, components, and subsystems through the utilization of a high-resistance medium (TΩ/mm). A diverse variety of materials is used, including polyester, polyamide-imide (PAI), polyester-imide (PEI), mica, asphalt, nylon, and epoxy resins, which find application in various insulation roles, such as turn-to-turn insulation, or coil-to-core and other insulation within a machine's stator and rotor [49]. A classification of insulation materials based on Fig.3.1 follows:
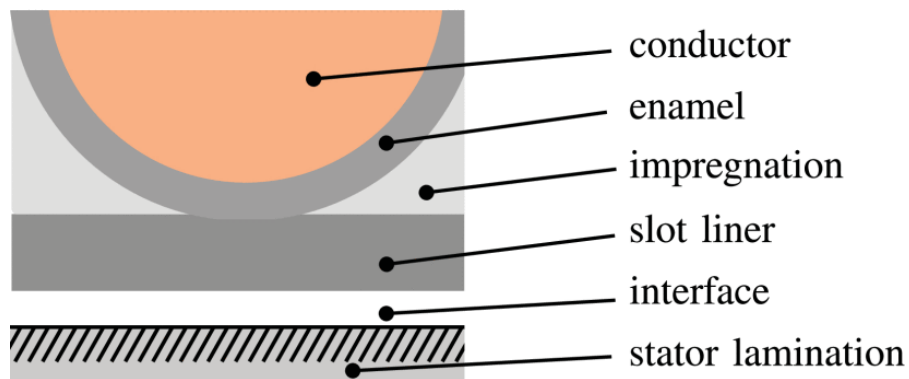
Fig.3.1: Geometry of insulation system [50]

3.1.1 Enamels [51]

Enamels serve as insulation materials in electrical machines, known as primary insulation since they are directly applied to the copper.

Polyimide (PI) enamel is commonly employed as an organic insulating material in environments with exceptionally high thermal conditions.

Polyamide-imides (PAIs) serve as high-temperature insulating materials extensively employed in electrical machines, functioning as an insulating varnish for enameled wires. Notably, their significance extends to the encapsulation of high-temperature machines, as they offer the capability to achieve substantial insulating layers, making them particularly valuable for such applications.

Polyester-imide (PEI) is extensively utilized in the production of enamelled wires, particularly for applications involving lower temperatures. The modification of PEI with THEIC through crosslinking reactions results in improved thermal, mechanical, and electrical properties.
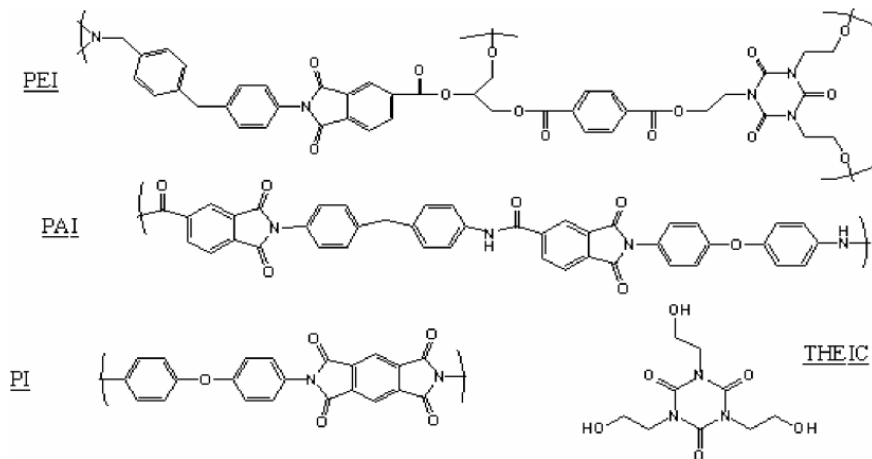
Fig.3.2: Chemical structure of PEI, PAI, PI and THEIC monomer [51]

3.1.2 Winding Impregnation Materials

Bare windings in electrical machines tend to experience vibration and deformation during operation, posing a potential risk of failure. To address this, stator windings are conventionally impregnated with varnish or epoxy to mitigate vibrations during operation. This impregnation process not only diminishes vibration but also enhances the average thermal conductivity of the coils by minimizing air gaps or voids between the strands. Vacuum impregnation represents a more advanced approach to achieving this, as it significantly reduces air voids, leading to improved efficiency and a reduced temperature gradient in the windings. Epoxy resins serve as an alternative impregnation material, offering heightened thermal conductivity, albeit at the expense of lower resistivity and dielectric strength.

3.1.3 Slot Liners

The separation between the winding and stator core is typically ensured by employing a suitable slot liner material in conjunction with winding impregnation. Commonly, slot liners come in the form of film or paper-like sheets, formed to size and placed alongside the winding within the slots of the stator assembly. The materials used for slot liners and impregnation interact during the winding impregnation process, influencing the thermal properties of the entire stator-winding assembly. For instance, the impregnation material may penetrate and fill cavities within the stator-winding assembly, and the slot liner material might absorb some of the impregnation [52].

According to [53] some of the slot liner materials used are the Nomex 410, ThermaVolt and CeQUIN I. ThermaVolt exhibits the highest thermal conductivity among these materials, corresponding to its higher density. CeQUIN I, while having lower stated thermal conductivity, is highly absorbent and requires impregnation for optimal physical properties. Nomex 410 stands out with the highest dielectric breakdown voltage and tensile strength. ThermaVolt and CeQUIN I are categorized as inorganic liners, while Nomex 410 is classified as an organic liner. CeQUIN I, with high inorganic content, is composed mainly of glass fibers and microfibers, inorganic fillers, and less than 10% organic binders. It is noted for fragility during assembly, especially in processes involving mechanical stress. Both CeQUIN I and ThermaVolt are suitable for single-stage assembly with limited mechanical stress, whereas Nomex 410 is robust and allows for repeatable conductor insertion, such as 'winding in situ.' Storage precautions are recommended for Nomex 410 due to its organic composition.

3.2   Diagnostic Tools [20]

The degradation of insulation materials in machines is influenced by various factors that act simultaneously and interact with each other. For instance, electrical stress can lead to temperature increases, triggering chemical and mechanical stresses. Over time, these factors may cause severe degradation in insulation materials, resulting in issues such as partial discharge, reduced dielectric properties, diminished voltage resistance, adhesion problems, delamination, surface erosion, oxidation, and the formation of treeing and micro-cracks. Repetitive partial discharge events significantly accelerate the ageing process, transitioning from intrinsic ageing to rapid extrinsic ageing ultimately leading to catastrophic failure in electric machines. This failure is

characterized by sustained short-circuit conditions, particularly in stator coils, where short circuits can manifest as phase-to-ground, turn-to-turn, and phase-to-phase faults [54].

Therefore, the literature incorporates a variety of electrical insulation tests designed to assess the dielectric, physical, electrical, and chemical properties of insulation. These tests serve the purpose of assessing the insulation's state of health, reliability, and facilitating maintenance planning. They fall into two categories: online and offline. Online testing occurs while the electrical machine is in operation, extracting real-time stresses to monitor insulating material degradation. However, online testing may not reveal all failures within an electrical machine. Therefore, offline tests are essential. In offline tests, methods are applied shortly after the electrical machine is shut down and disconnected from the power supply.

3.2.1 Offline Insulation Tests

Some of the offline insulation tests are summarized in Fig.3.3.

Test	Standard	Test Description
Insulation resistance (IR)	IEEE 43 [10], NEMA MG1 [11]	Contaminations and defects between phase to ground can be found
Polarization index (PI)	IEEE 43	Contaminations and defects between phase to ground can be found
DC high potential test	IEEE 95 [12]	Defects between phase to ground can be found
AC high potential test	NEMA MG1 or IEC 60034	Defects between phase to ground can be found and more effective than DC high potential test
Offline partial discharge	IEC 60270 [13], IEC 62478 [14], IEEE 1434 [15], IEC 60034-27-1 [16], ASTM D1868 [17]	Defects between turn to turn and phase to ground can be found
Dissipation (power) factor	IEEE 286 [18] or IEC 60894 [19]	Contaminations and defects between phase to ground can be found
Surge test	IEEE 522 [20] and NEMA MG1	Defects between turn to turn and phase to ground can be found

Fig.3.3: Offline insulation tests for electrical machines [55]

3.2.1.1 Insulation Resistance (IR) & Polarization Index (PI) [56]

This constitutes the most well-known type of diagnostic test for machine windings. It is also referred to as the Megger test, derived from the name of the company that initially manufactured an instrument for measuring IR (insulation resistance) and PI (polarization index).

The IR test measures the resistance between the copper conductors and the core(ground) located in the stator or rotor by applying DC voltage. In theory, this resistance should be infinite to prevent any current leakage between the copper and the core. However, in the real world, nothing is ideal, so the insulation resistance is not infinite but typically has a very high value. Conversely, a low value suggests a problem in the insulation mechanism.

To mitigate the impact of temperature variations on the measurement, the Polarization Index (PI) test is employed. Specifically, the *PI* (Eq. 3.1) is the ratio of the resistance value measured during the IR test at a DC voltage applied for 10 minutes (R_{10}) to the resistance value measured for 1 minute (R_1)

$$PI = \frac{R_{10}}{R_1}$$

(Eq.3.1)

The measurement of resistance is done using Ohm's law. However, caution is needed because the current does not remain constant throughout the measurement. There are at least 4 currents that can compose the total measurement current, which are described in detail below:

- *Capacitive Current:*

When a continuous voltage is applied to a capacitor, initially a high current flow exponentially decreases. The magnitude of the internal resistance of the source and the capacitance of the capacitor defines the exponential decay (Eq. 3.2):

$$I = I_0 e^{-\frac{t}{\tau}}$$

(Eq.3.2)

where $\tau = RC$. If considering that a form-wound stator coil can have a capacitance between the conductors and the core equal to 1 nF, or a hydroelectric generator a capacitance of 1 μF, then it can be easily understood that the current practically becomes zero in less than 10 seconds. For this reason, the IR measurement was standardized for one minute to disregard the influence of capacitive charging.

- *Conduction Current:*

This current flows due to electrons or ions crossing the insulation, traveling from the conductors of the coil to the core. Conduction current may exist if the insulation has absorbed moisture. Additionally, this current appears if there are cracks or holes in the insulation and contamination is present, creating a galvanic coupling between

the core conductor. This current is constant over time and ideally zero. Modern insulation systems lead, under healthy conditions, the conduction current to zero. Deviation from zero signifies an error.

- *Leakage Surface Current:*

This is a constant current that flows on the surface of the winding insulation. It is due to external contamination factors that cause the conduction of current (oils or moisture mixed with soil, dust, ash, chemicals, salts, etc.). Theoretically, this current should be zero. Elevated values are associated with rapid ageing of insulation as there is electrical conduction and heat. It has been observed that the surface leakage current is high in machines with round rotor windings or in salient pole windings where the excitation winding is exposed.

- *Absorption Current:*

Most dielectric materials in the insulation system contain polarized dipoles. When an external electric field is applied, these dipoles align. The energy for alignment comes from the current provided by the voltage source. When alignment is achieved, the current is then reduced to zero. This current is called polarization current and is a part of the absorption current. Current also flows due to trapped electrons within the layers of the insulating tape. Experience has shown that the absorption current is initially high and tends to zero after approximately 10 minutes in modern groundwall insulation systems.

Among all the individual currents, diagnostic information is contained in the conduction and leakage currents. If only R_1 is measured (1 min), the absorption current has not yet been zeroed. The resistance R_1 depends on temperature; a 10°C increase reduces R_1 from 5 to 10 times. Thus, the Polarization Index is used to mitigate the influence of temperature.

The Table 3.1 outlines the guidelines for DC voltages to be applied during the Insulation Resistance (IR) and Polarization Index (PI) tests. The V_{rated} voltage pertains to the line-to-line voltage for three-phase AC machines and line-to-ground voltage for single-phase AC machines.

Winding Rated Voltage (V_{rated})	Insulation Resistance Test Direct Voltage (V)
<100	500
1000-2500	500-1000
2501-5000	1000-2500
5001-12000	2500-5000
>12000	5000-10000

Table 3.1: Guidelines for DC voltages to be applied during the Insulation Resistance (IR) and Polarization Index (PI) tests [20]

3.2.1.2 Surge Test [57]

Surge test (Fig.3.4) can directly measure the integrity of insulation in any winding topology of a stator or sometimes rotor windings. It is based on the use of high voltage surges between turns. Motors powered by electronic power sources exhibit sudden voltage increases, resulting in imbalanced voltage distribution across the coils. If the appearance time of these spikes is very short, the voltage is sufficiently high, and there is weakness in insulation, then there will be a breakdown, leading to failure. Surge test simulates this phenomenon. The surge test is a type of destructive measurement where the specimen will either pass or be destroyed. If insulation fails the test, it is automatically considered that under real conditions, it would also fail in switching conditions, power converter overvoltage, or dynamic phenomena. Essentially, when testing windings, a fault between turns can be diagnosed due to the change in resonance frequency. The capacitor is charged by a high DC voltage through the winding. When the capacitor is fully charged, the switch is closed. The energy stored in the capacitor oscillates in the circuit. The resonance frequency is given by the following equation (Eq. 3.3):

$$f = \frac{1}{2\pi\sqrt{LC}}$$ (Eq.3.3)

If there is no fault, then the oscillation frequency remains constant. On the contrary, if there is a turn fault, then the circuit experiences a decline in inductance and an increase in resonance frequency. This can be detected on the oscilloscope. The surge test can be applied comparatively across the three phases.
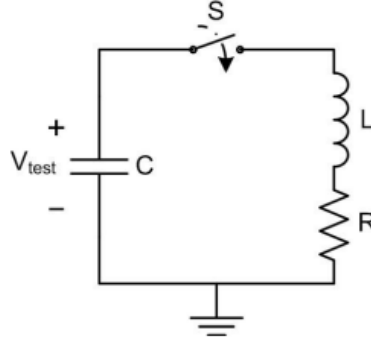
Fig.3.4: Surge test equivalent circuit

3.2.1.3 DC Hipot TEST

The DC high potential test, also known as the DC hipot test, is applied to stator windings. This involves applying a DC voltage that exceeds the peak AC voltage experienced during regular operation. The fundamental concept is that if the winding withstands the high voltage without failure, it is unlikely to experience failure soon due to insulation ageing when returned to service. Failure in the DC hipot test indicates the necessity for repairs or rewinding, as it signifies a puncture in the coil-to-core insulation. Stator windings must successfully undergo a hipot test post-manufacture, often referred to as a commissioning or acceptance hipot. Moreover, end users conduct a low-voltage hipot test on stators that have been in operation, known as maintenance hipot.

A variant of the DC hipot test is known as the DC ramp test. DC Ramp Test method involves a slow and continuous increase of the applied voltage (typically 1kV/min or 2kV/min) to avoid unexpected damage to the insulation [58], [59]. The insulation current versus the applied voltage is recorded in the form of an X-Y plot, providing the capability for continuous observation and analysis of the current response. By applying a ramped voltage, the capacitive charging current I remain constant, as can be inferred from Eq.3.4:

$$I = C\frac{dV}{dt}, V = rt \tag{Eq.3.4}$$

where r: constant and t: time.

Thus, the capacitive current can be neglected, facilitating the easier detection of variations in the measured current. It is also of utmost importance to note that any variation in the rate of rise of the applied voltage will induce a nonlinear change in current, consequently compromising the accuracy of the test results. Therefore, a stable

and well-regulated high-voltage supply is essential. Investigations [60] have shown that the ramped high-voltage DC test method can detect and monitor insulation delamination.

3.2.1.4 AC HIPOT Test

The AC hipot test closely resembles the DC hipot test, differing only in the application of power-frequency voltage (typically 50 or 60 Hz). Occasionally, 0.1 Hz AC, known as very low frequency or VLF, is also utilized. Both acceptance and maintenance versions of the AC hipot test are employed. A modified form of the acceptance test includes a scaled-down AC voltage hipot examination, particularly carried out when a stator winding is immersed or saturated in water. This "sealed" winding hipot test aims to confirm the successful sealing of the stator winding to prevent moisture ingress.

3.2.1.5 Stator Capacitance Tip-Up

This test is an indirect Partial Discharge (PD) test that measures the void content present in the coil-to-core insulation. If the capacitance tip-up increases, this implies the presence of more voids in the insulation. Capacitance can be determined either by measuring each phase separately and connecting the other two to the ground, which is the most effective method, or by measuring the phase-to-phase voltage. To determine the capacitance tip-up, initially, the capacitance corresponding to 20% of the rated voltage of the stator is measured C_{lv}. Subsequently, the voltage is increased to a level of 60% of the line-to-ground voltage for the C_{hv} to be calculated. Thus, the capacitance tip-up is (Eq.3.5):

$$\Delta C = \frac{C_{hv} - C_{lv}}{C_{lv}} \qquad\qquad (Eq.3.5)$$

3.2.1.6 Dissipation Factor (DF) and Power Factor (PF) [61],[62]

Both tests assume insulation behaves differently from ideal conditions, stemming from the capacitance-defined optimal insulation. In practice, insulating material is simulated by a circuit, often in parallel or series, including both lossless capacitance C and resistance R representing dielectric losses.

The loss vector diagram (Fig.3.5) can be illustrated through a graph where the current across the capacitor precedes the voltage by an angle $(\theta < 90°)$. Ideally, θ should be 90° as it stands for an ideal capacitor. However, due to the dielectric losses induced by the resistive part of the insulation, an angle δ formed between θ and 90° which represents the dielectric loss. Tanδ is equivalent to the ratio of the resistive component of the current to the current across the capacitor. Therefore, a higher *tanδ* indicates greater losses in insulation. Tanδ is alternatively referred to as the Dissipation Factor (DF).
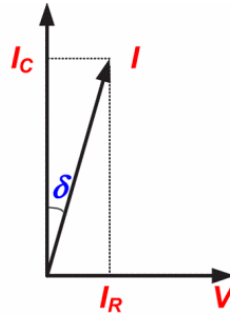
Fig.3.5: Loss Vector Diagram

DF calculates the dielectric losses of the insulation [60]. These losses constitute a property of the insulating material. DF can indicate thermal deterioration, moisture absorption, end-winding contamination, and damage. Thus, the trends of the measured Dissipation Factor (DF) indicate the presence of faults in the groundwall insulation and indicate its health condition.

One way for measuring the DF involves using a balanced bridge-type instrument – typically a Schering Bridge (Fig.3.6). In this setup, a resistive-capacitive circuit (Z_4) is adjusted to match the voltage and loss angle δ measured across the stator winding(Z_1). Subsequently, the DF is computed based on the resistive (R_1) and capacitive (C_1) elements in the bridge that result in a zero voltage.
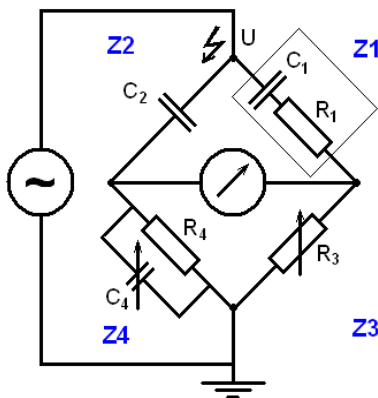
C_1: The capacitor whose capacitance is to be calculated
R_1: A series resistance representing the loss of C_1
C_2: A standard capacitor
R_3: A variable non-inductive resistance
C_4: A variable capacitor
R_4: A non-inductive resistance

Fig.3.6: Schering Bridge [63]

An alternative method for measuring DF is through digital means, involving the measurement of the phase difference between the voltage and current passing through the stator winding, which corresponds to the loss angle δ. The tangent of δ indicates the presence of dielectric loss.

The dielectric loss can be determined not only by DF but also by power factor (PF). *PF* (Eq.3.6) is a measure of real power W [Watts] using a Wattmeter divided by apparent power S [volt-amps (VA)], which is the product of the voltage V applied across the copper and the core of the winding and the current I arising from the applied voltage.

$$PF = \frac{W}{S} = \frac{W}{VI}$$
(Eq.3.6)

The measurements of PF and DF are conducted using power-frequency AC voltage to energize the windings. If a low AC voltage supplies the windings, the measurement may not be reliable because the inductive and capacitive elements of the equipment may introduce power frequency currents into the winding, thereby distorting the measurement. To prevent this phenomenon, a frequency other than 50 or 60 Hz should be selected, or a high power-frequency voltage should be applied to the stator winding.

The correlation between PF and DF as diagnostic methods can be illustrated by Eq.3.7:

$$PF = \frac{DF}{(1+DF^2)^{0.5}}$$
(Eq.3.7)

3.2.1.7 Power (Dissipation) Factor Tip-Up (PFTU) test [62]

The PFTU, or DFTU test, is a way to determine if PDs are occurring in high-voltage stator winding. The PFTU is calculated by assessing the difference in power factor (PF) between two specific test voltages. Manufacturers frequently determine Tip-Up (Eq.3.8) by comparing PF values acquired at the operational voltage (line-to-neutral) PF_{hv} and approximately 25% of that voltage PF_{lv} as shown in the equation. The higher the tip-up, the more energy has been consumed due to the occurrence of PDs.

$$Tip - Up = PF_{hv} - PF_{lv}$$
(Eq.3.8)

3.2.1.8 Partial Discharge Tests [64]

Partial discharges (PD) are like tiny electrical sparks caused by gas breakdown (e.g., in air) within empty spaces or in areas with uneven electric fields. PDs involve a quick movement of electrons across a gas-filled gap. Since each electron carries a charge q, each PD creates a current pulse $i=dq/dt$. Apart from the flow of electron current, there is also a movement of positive ions in the opposite direction, generated when electrons become ionized from gas molecules. The PD current within the void causes a disturbance, leading to the generation of pulse current and voltage that travel away from the PD site. A Fourier transform of a current pulse reveals the creation of frequencies up to several hundred megahertz.

Any sensor, also known as a PD coupling device, that is sensitive to high frequencies can detect the PD pulse currents. In an offline PD test (Fig.3.7), the detection of PD currents typically involves utilizing a sensor-PD coupling device, commonly a capacitor connected to the terminals of the equipment undergoing testing. This capacitor, with a capacitance value ranging between 80 and 1000 pF, is designed to be responsive to high frequencies, allowing it to effectively capture PD pulse currents resulting from electron emissions during PD occurrences. The output from this capacitor then triggers a detector, which converts the PD pulse currents into voltage. This detector, often referred to as an RLC detector, exhibits either resistive or inductive-capacitive behavior, functioning as a low-pass filter. It integrates the PD pulse current, generating a signal magnitude proportional to the apparent charge transfer caused by PD. This detection method proves highly effective, as the extent of insulation deterioration correlates with the quantity of electrons and ions impacting the insulation.

1. HV Supply
2. Test Object
3. PD Coupling Capacitor (sensor)
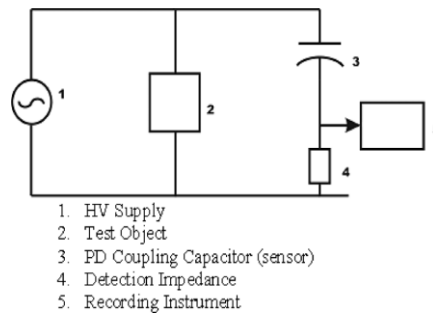4. Detection Impedance
5. Recording Instrument

Fig.3.7: Offline PD Test Setup

Regarding the recording instruments used in offline test methods (Fig.3.7), electronic equipment has replaced traditional methods by utilizing digital technology

to measure signals from sensors and PD detectors. Analog approaches are being supplanted by more sophisticated means. Digital oscilloscopes, Pulse Magnitude Analyzers (PMAs), and Pulse Phase Analyzers (PPAs) are now commonplace for PD measurement. Digital oscilloscopes provide a standard method, offering detailed measurements of the peak apparent charge. An even more advanced approach involves PMAs, utilizing a digital circuit to count the number of pulses per second and display a graph illustrating pulse count versus pulse amplitude. A variation of this method is the Pulse Phase Analyzers (PPAs), which, in addition to counting pulses, record the voltage corresponding to each PD pulse. PPAs present a graphical representation in 2 or 3 dimensions, illustrating the pulse count rate in relation to pulse magnitude and pulse phase position.

The offline Partial Discharge (PD) test entails a methodical elevation of applied voltage, while simultaneously monitoring PD pulses using some of the recording instruments presented in the current section. The voltage level at which initial PD occurs is termed the Discharge Inception Voltage (DIV). Subsequently, the voltage is raised to a specified level, with the winding energized for 10 to 15 minutes, during which peak PD magnitudes (Q_m) are recorded. Q_m can be measured in picoCoulombs (pC), millivolts (mV), milliamperes (mA), and decibels (dB). pC is determined through a laboratory PD measurement device and corresponds to the apparent number of electrons involved in the discharges. mV is measured when using an oscilloscope or PMA (which also counts the number of PD pulses). mA is applicable when PD pulses are measured with a high-frequency (ferrite core) current transformer and displayed on an oscilloscope. dB is used if a frequency spectrum analyzer records the pulses. This crucial "soak" or "conditioning" period is essential due to heightened PD in the initial minutes, attributed to space charge effects and gas pressure build-up in voids. The voltage is then gradually reduced, and the voltage at which PD becomes imperceptible is termed the Discharge Extinction Voltage (DEV). Although DEV is generally lower than DIV, the presence of high values for both DIV and DEV is considered highly advantageous.

3.2.1.9 Frequency Response Analysis

The Frequency Response Analysis (FRA) technique is widely used in power transformers and other electrical machines due to its high sensitivity. It's a straightforward method for assessing machine condition by introducing a voltage signal with varying frequency. By analysing how the machine's parameters respond to these frequency changes, valuable insights are gained. FRA unveils information about the machine's internal parameters, often described metaphorically as a "black box." The interpretation of FRA results requires a reference point, typically the response of a healthy machine under similar conditions. By comparing the frequency response of the machine under examination with this reference, deviations or abnormalities can be identified. Additionally, FRA has been applied in poles [98].

The FRA is a diagnostic method that involves injecting a voltage with varying frequency into one side of the winding and measuring the response on the opposite side. The voltage gain, H, is determined by the values at the input (V_{in}) and output (V_{out}) of the winding, respectively (Eq.3.9).

$$H(j\omega) = \frac{V_{out}}{V_{in}}$$

(Eq.3.9)

The voltage gain is commonly depicted in decibels (Eq.3.10) using a Bode diagram plot.

$$H_{dB} = 20 \cdot log_{10}|H(j\omega)|$$

(Eq.3.10)

The FRA analyser produces a sinusoidal voltage of 1.44 V amplitude, ranging frequencies from 20 Hz to 20 MHz. A computer is then utilized to capture the voltage transfer function, enabling the measurement of input and output voltages.

A subcategory of FRA is impedance spectroscopy, which studies the variation of impedance with variations in frequency.

3.2.1.9.1   Impedance Spectroscopy & Nyquist Diagram

Impedance spectroscopy has attracted an increased interest in recent years for monitoring the health condition and assessing the state of machine components, such as insulation and materials [65]-[67]. This is attributed to its non-destructive nature. The specimen undergoes measurements across a broad range of frequencies and is characterized based on its behaviour, as indicated by the amplitude and phase response at resonance frequencies. The derivation of impedance enables its representation as a

complex transfer function, expressed as an electrical V/I function. This allows for its depiction through Bode and Nyquist diagrams.

Nyquist Diagrams map the trajectory of the impedance vector's geometric locus during the frequency variation [68]. The vertical axis represents the imaginary part of the complex impedance, while the horizontal axis represents the real part. This configuration facilitates the analysis of the frequency pattern of impedance across both low and high-frequency ranges.

3.2.2 Online Insulation Tests

3.2.2.1 Partial Discharge [64]

This monitoring system actively identifies electrical pulses associated with stator winding PD during the regular operation of the motor or generator. It closely parallels the offline PD test in various aspects. Online PD monitoring can be carried out periodically or continuously.

An online PD monitoring system should include the following equipment:

- A sensor intended for the identification of PD current and its subsequent conversion into voltage.

- Instrumentation designed for the comprehensive characterization of PD signals, encompassing the determination of PD event count, magnitude, polarity, and AC phase position. Additionally, the instrumentation may assist in distinguishing PD from ambient electrical noise.

- Software, human expertise, or a combination of both employed to transform PD data into valuable insights about the condition of the insulation system.

The PD monitoring system records detected PD pulses using monitoring systems like oscilloscopes, PMAs, and PPAs. For effective interpretation of results, three options exist: a) trending the Qm over time on the same machine, b) comparing Qm with identical machines, c) assessing Qm against similar machines with specific constraints. In each case, the monitoring method employed should remain consistent.

Conducting on-line testing presents significant challenges, primarily due to heightened electrical interference caused by the test object's connection or proximity to the power system. This interference stems from various sources, such as power tool operations, poor electrical contacts, and electrostatic precipitators. These sources

generate sparks or discharges, producing current pulses that closely resemble partial discharge (PD) signals. Effectively distinguishing this noise from genuine PD signals becomes imperative. The misinterpretation of noise as PD can result in a false indication of insulation deterioration, compromising the reliability and credibility of the PD test. The literature has introduced various patterns designed to differentiate PD from noise and identify the root causes of PD occurrences, particularly in instances where diverse mechanisms have faced failures. Some of these patterns are the following:

- *Statistical Analysis:*

It is based on calculating the mean, standard deviation, skewness, and kurtosis to identify the shapes and positions of PD pulse patterns versus the phase angle. The values of these quantities are specific to each PD mechanism and each type of noise. Any potential changes in their values lead to the formation of PD patterns versus phase angle. It is noteworthy that, this method is effective only if there is a single cause that triggers PDs.

An alternative but not commonly used way to apply this method is through the mixed-Weibull probability distribution, where each PD mechanism or noise source has its own distribution. This method can be employed even in cases where multiple causes may cause PD.

- *Neural Networks:*

This method is based on the recognition of PD pulse current [69]. It is not widely used to date, but it is continuously evolving and has been characterized as having a low error probability in pattern recognition. Nevertheless, it entails a relatively high computation time. The data received by the neural network from the measurement device includes pulse shapes, the time interval between successive pulses, the phase position, and the magnitude of the phase polarity. After receiving the data, the neural network is trained by analyzing the PD data originating from a PD mechanism. Once the learning process is completed, the neural network is capable of identifying the cause of various PD patterns.

- *Fractal Analysis:*

It is based on the analysis of the shapes of objects and categorizes three-dimensional patterns derived from a Pulse Phase Amplitude (PPA). It analyzes patterns originating from multiple PD mechanisms.

- *Wavelet Transform:*

This method is used to reduce the impact of noise. Similar to neural networks, it is not yet widely adopted, but it requires less computation time. It is a type of software that takes PD and noise pulses as input from an A/D converter, which digitizes them. Subsequently, the software receives these digital signals and is trained to transform, process, and perform an inverse transformation on them. The outputs of this software include a PPA (Pulse Phase Amplitude) plot that is free from noise.

- *Fuzzy Logic [70]:*

This approach is a pattern recognition technique, applied independently or in tandem with neural networks or time-frequency clustering. PD occurrence in a void is influenced by numerous random variables. Fuzzy logic is used to characterize PD, applying vague rules like associating big pulses with large voids. While fuzzy logic has been applied to PD patterns since the 1990s, it's often limited to defining void size rather than addressing diverse failure and noise processes. Implementing fuzzy logic requires numerous rules, and knowledge of real-world insulation systems is often unknown.

- *Time vs Frequency Clustering*

This method uses an A/D converter oscilloscope. Then, it transforms the data and generates a time versus frequency graph. In this graph, PD and noise sources form clusters, and fuzzy logic is used to recognize these clusters. Subsequently, each PD or noise pulse is associated with one of the clusters. This way, PPA plots can be created, having eliminating the PD and noise sources.

3.2.2.2 Thermography

In this method, infrared thermal imaging cameras operate within the infrared spectrum, capturing the emitted energy from heated objects in correlation with their temperature. By assessing the normal surface temperature of equipment, abnormal hotspots can be easily pinpointed. Modern thermal imaging cameras are equipped with

computers to directly display surface temperatures and facilitate comparisons between current and past images, enabling the identification of thermal changes.

While thermography has limited applicability in motors during operation due to inaccessible key areas, it proves useful in detecting significant issues like severe cooling system blockages. When observing only the machine surface, a comparison of present images with stored images taken under similar operating conditions can offer a general indication of temperature changes. Discrepancies in temperature within specific areas compared to the entire machine's past images may indicate issues such as local blocked cooling passages in the stator or an imbalance in phase-to-phase voltage, causing one phase to operate at a higher temperature than the others.

3.3   Multifactor Ageing Tests

Exploring the performance of insulation systems under a range of stresses (Section 2.1) is paramount in the electrical machines industry for optimizing design and quality, thereby improving their ability to withstand the effects of ageing. These investigations fulfil several objectives, including the development of novel insulating materials, assessment of insulation systems, qualification processes, post-production acceptance tests, and the diagnostic evaluation of high voltage machine insulation conditions, coupled with estimating the residual lifetime.

An exceptionally effective approach to evaluating the ageing endurance of an insulation system is through the implementation of accelerated ageing tests, which involve multifactor ageing techniques. In these assessments, ageing stresses are applied at levels significantly exceeding normal service conditions, or at a faster rate of change, resulting in a hastened process of deterioration and breakdown occurring within hours or days, rather than years. Manufacturers routinely employ accelerated ageing tests incorporating thermal, electrical, ambient and mechanical stresses to guide the design of innovative insulation systems. In this chapter, methods of multifactor ageing found in the literature will be presented, which involve the application of two or more types of stress.

Typically, the accelerated ageing test involves a comparison of the candidate system's behaviour with that of a well-established reference system with proven service life. Beyond assessing the lifetime in these tests, diagnostic measuring methods

(discussed in Section 3.2) offer valuable insights into alterations in electrical and dielectric properties resulting from the ageing processes in the tested insulation system.

In the current section, various accelerated ageing tests found in the literature will be presented, dividing them into the categories of accelerated thermal stress, electrical-thermal stress, electrical-thermal-mechanical stress, thermal-ambient-mechanical stress, and electric-mechanical-thermal-ambient stress. The test specimens that will undergo multifactor ageing procedures are stator bars, formettes, statorettes and twisted pairs. For each type of ageing test, the experimental setup procedure will be briefly described, followed by an emphasis on interpreting the results obtained from diagnostic tools.

3.3.1 Accelerated Thermal Aging [71]-[74]

The Accelerated thermal ageing method relies on functional tests to thermally evaluate the insulation system of electrical machines. Thermal stress is deemed the primary ageing factor, with mechanical and environmental stresses serving as diagnostic factors to ascertain the ageing process.

Standard 60034-18-31(Fig.3.8a) offers a straightforward and detailed process for evaluating sample ageing. The procedure starts with applying initial mechanical stress, including vibrations at 60 Hz frequency and an acceleration of 1.5 g for one hour. Subsequently, the samples undergo a 48-hour exposure to humidity ranging from 95% to 100%. Additional diagnostic measurements, such as Insulation Resistance (IR), Partial Discharge tests (PDIV), Dissipation Factor (DF), and Capacitance measurements (IC), are recommended, with the flexibility to choose other measurements as per the norm. Following this, a diagnostic test is carried out, specifying voltage for AC high potential tests and impulse voltage tests according to IEC 60034-15. Lastly, thermal exposure occurs in cycles within an oven, with predefined periods interspersed with breaks for diagnostic measurements. The standard specifies the temperature and duration of each cycle, aiming for approximately 10 thermal exposure cycles. The end-of-life of a sample is determined when it fails the proof test.

According to an alternative protocol within the same standard, IEC 60034-18-34 (Fig.3.8b), an initial quality control phase involves subjecting specimens to vibrations at 60Hz and an acceleration of 1.5 g for one hour. This step aims to identify

weaker samples, which are subsequently eliminated from the test procedure. Following this, the specimens undergo a thermal cycling test, exposed to temperatures ranging from 30 degrees Celsius up to the Temperature Index. The Temperature Index is a numerical representation derived either mathematically or graphically from the thermal endurance graph, corresponding to the temperature in degrees Celsius. The thermal endurance graph, in turn, visually depicts the thermal endurance relationship, plotting the time to failure against the reciprocal of the absolute test temperature [17]. Diagnostic tests, including IR, DF, PDIV, IC, and other chosen tests, are conducted after a specific number of cycles, as illustrated in Fig.3.8. Finally, the specimens are subjected to thermal endurance tests where a voltage exceeding that expected in operation is applied to the insulation system. The time to failure is measured and compared with a reference system.
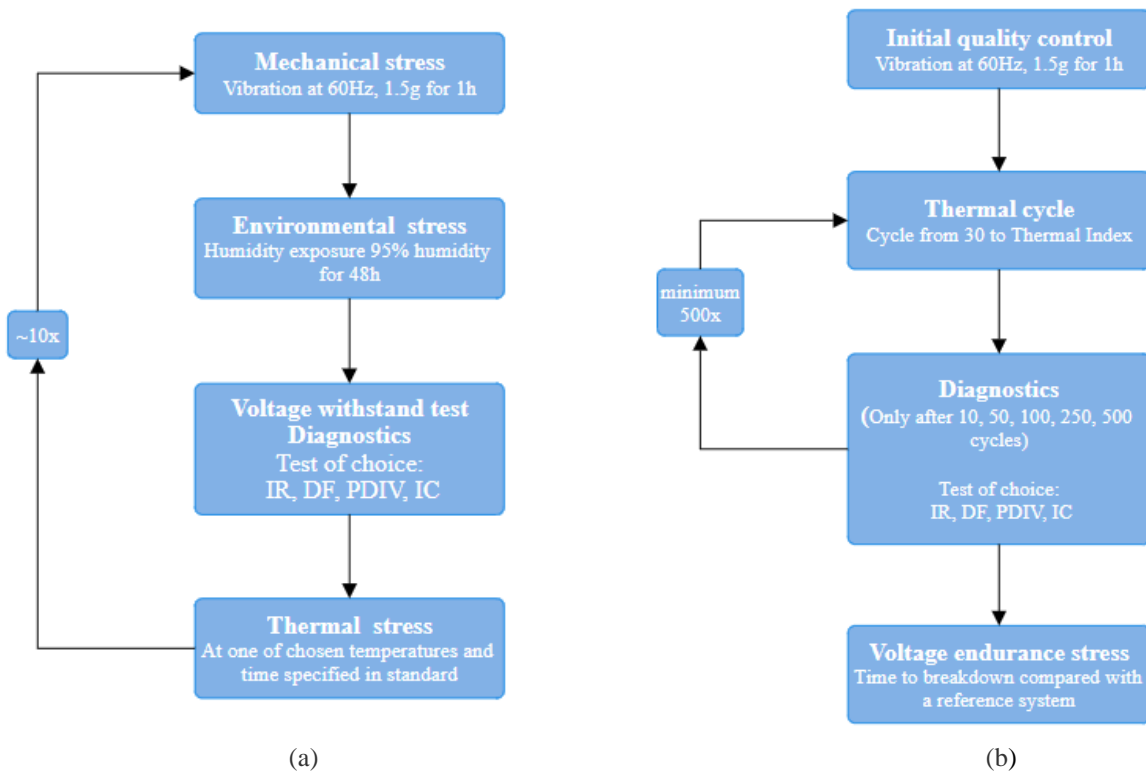

(a)   (b)

Fig.3.8: (a) Testing Protocol for Electrical Insulation System Qualification per IEC 60034-18-31, (b)Testing Protocol for Electrical Insulation System per IEC 60034-18-34 [72],[73]

In [71], an instance of the aforementioned thermal evaluation protocols for electrical insulation systems is demonstrated (Fig.3.10) using a formette (Fig.3.9). Formette is a wound model frequently employed in thermal assessment tests for

machine insulation systems. It replicates the magnetic core and mechanical supports, ensuring accurate simulation of operational conditions during testing.
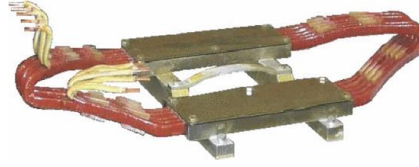

Fig.3.9: Formette Coils as a Model for Electrical Insulation

Initially, the insulation system undergoes mechanical stress, where the sample is placed on a shake table and exposed to vibration at a frequency of 60Hz, with a peak-to-peak amplitude of 0.3mm and acceleration of 1.5g for one hour at room temperature ($23°C$). Subsequently, the sample is subjected to environmental stress through exposure to humidity ranging between 95% and 100% relative humidity for 48 hours. Non-destructive diagnostic tests follow, focusing on Insulation Resistance, PD (Partial Discharge) test, and Dissipation Factor. For assessing the insulation condition and determining its lifespan, alternative and impulse voltage tests are applied. Finally, the samples are transferred to ovens at temperatures specified in the diagram. After all these stages, the presented procedure is repeated.
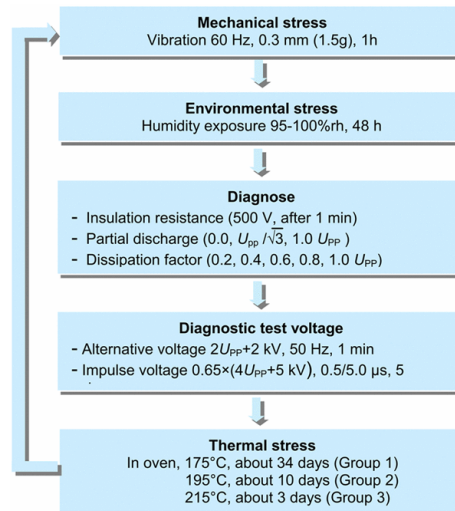

Fig.3.10: Procedure for Accelerated Thermal Ageing Test [71]

a) *Diagnostic Test Voltage*: The results indicate End-of-Life in the insulation system subjected to Accelerated Thermal Ageing, revealing Breakdown occurrences. Breakdowns under alternative voltage occurred in the coil-to-core insulation, while those under impulse voltage affected both the coil-to-core and turn insulations.

Lifespan estimation involved plotting lifetime against temperature and comparing the insulation system under investigation with a known reference system. The breakdown in the insulation, leading to failure, is caused by thermal deterioration due to thermal stress.

b) IR test: The findings reveal a slight decrease in insulation resistance over ageing cycles, with a relatively low rate of change. This suggests a minimal rate of decomposition for the bonding materials of insulation systems.

c) Dissipation Factor: DF exhibits a distinct shift in its response to applied voltage during the initial cycle, influenced by insulation drying and post-curing. Furthermore, an initial increase in the dissipation factor (low-voltage tan δ) suggests a combination of polarization and conducting losses, attributed to chemical reactions that break down high-weight epoxy molecules, generating lower-weight polar molecules and intensifying dielectric losses. Insulation humidity contributes to an enhanced initial dissipation factor value, indicative of intricate interactions. As ageing cycles progress, the dissipation factor rises with test voltage in both insulation systems, associated with delamination formation within the main insulation or at copper conductor interfaces due to thermal stress. The increasing ageing cycles result in more air-filled voids and delaminations within the insulation, leading to heightened partial discharge activities and increased ionization losses.

d) Capacitance: The alterations observed in capacitance curves are marked by an initial decrease in capacitance and an amplified reliance on voltage. These changes are linked to the development of delamination within the insulation and the subsequent activities of partial discharge (PD). The initial decline in capacitance results from the sum of solid insulation and air-filled voids. However, at elevated voltages, only the capacitance of the solid insulation persists, attributed to void shorting induced by PD.

e) DF tip-up and ΔC: Both quantities increase with the growing number of ageing cycles. If the change in DF is minor from cycle to cycle, it signifies a reduction in the appearance of air-filled voids and delaminations. Conversely, an increasing change in DF indicates higher energy consumption due to the emergence of partial discharges (PDs).

f) Partial Discharge: PD measurements are sensitive to changes in insulation systems during ageing. Symmetrical PD patterns suggest discharges are primarily

within coil-to-core insulation. Increased partial discharge activity is observed with ageing cycles. After a certain point, the magnitude of the highest PD pulses stabilizes. As ageing progresses, there is a shift from small to lower amplitude discharges, and a "hollow" in the PD pattern expands, indicating an increase in discharges with higher values. The formation of delaminations within the main insulation, influenced by thermal expansion behaviour, is a key factor in increased PD activities and deterioration.

Comparisons of PD quantities reveal an overall increase in both the total number of PD pulses and transferred charge per second with ageing, suggesting a potential rise in discharge sites. The number of PD pulses per second stabilizes after the initial ageing cycles, indicating a consistent number of discharge sites. Concerning the total transferred charge per second, it either continues to increase or remains stable after the initial rise.

3.3.2 Electrical-Thermal Stress

In [89], a concurrent electrical and thermal stress test was conducted on twisted pair (TP) specimens. Twisted pair specimens have been prepared using enamelled wires insulated with conventional and nanocomposite enamels (Fig.3.11).
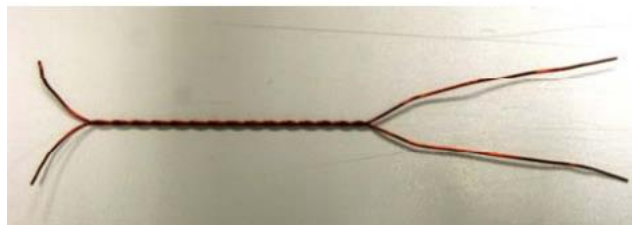

Fig.3.11: Twisted pair specimen [89]

Initially, the specimens undergo an electrical strength evaluation wherein a 50Hz sinusoidal voltage is applied, gradually increasing in amplitude at a rate of 500V/s until enamel breakdown occurs. Subsequently, the breakdown voltage is recorded as the test outcome.

The aging procedure test setup is illustrated in Fig.3.12. The arbitrary waveform generator produces low and high-frequency PWM waveforms, while the Arbitrary Waveform Amplifier for Dielectric Test (AWADIT) amplifies the resulting waveforms generated by the Arbitrary Waveform Generator.
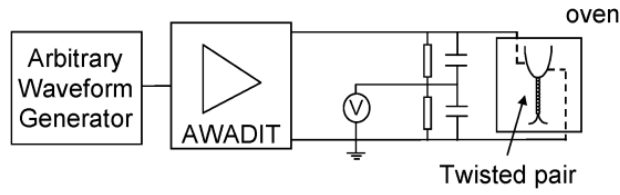
Fig.3.12: Twisted Pairs ageing test set-up [90]

Electrical ageing tests were conducted using various voltage waveforms with amplitudes exceeding the PDIV level. Throughout the tests, the specimens were maintained at a fixed temperature to investigate the combined effect of thermal stress on enamel lifetimes. A comparison of the results highlighted the influence of both enamel type and applied voltage waveform on the outcomes.

In [91], breakdown voltage and accelerated multistress ageing were conducted by combining electrical stress with high-frequency pulsating voltage and thermal stress through elevated temperatures. The twisted pair specimens were positioned in an air-circulating oven to enable testing at controlled elevated temperatures.

The breakdown voltage was determined by incrementally increasing the voltage at a rate of 50V/s until the sample broke down. The results suggest a significant decrease in insulation breakdown voltage when subjected to high temperatures and frequencies.

3.3.3 Electrical-Thermal-Mechanical Stress

The ageing process of electrical machine insulation results from chemical and physical degradation due to thermal, electrical and mechanical stresses. These stresses lead to irreversible alternations to the insulation system. Electrical stresses arise from applied voltage, transient voltages, partial discharge phenomena, and injected space charge. Variations in load current introduce cyclic thermal stresses and alter the temperature gradient across the insulation wall. Mechanical stresses, affecting the stator bars, involve cyclic bending, tension, torsion, and compression.

The implementation of multi-stress ageing allows for the application of more moderate stresses, resembling real-world service conditions and providing valuable insights into stress endurance-life characteristics. Simultaneous exposure to thermal, mechanical, and electrical stresses can either directly interact (synergize) or indirectly interact in ageing mechanisms. Synergism occurs when combined stresses result in a different ageing effect compared to applying individual stresses sequentially. In

practice, synergistic behaviour is prevalent, while instances of consistent ageing effects, regardless of simultaneous or sequential stress application, are rare [81].

This type of multistress has been applied either on stator bars (Section 3.3.3.1) or formettes (Section 3.3.3.2).

3.3.3.1 Electrical-Thermal-Mechanical Stress on Stator bars

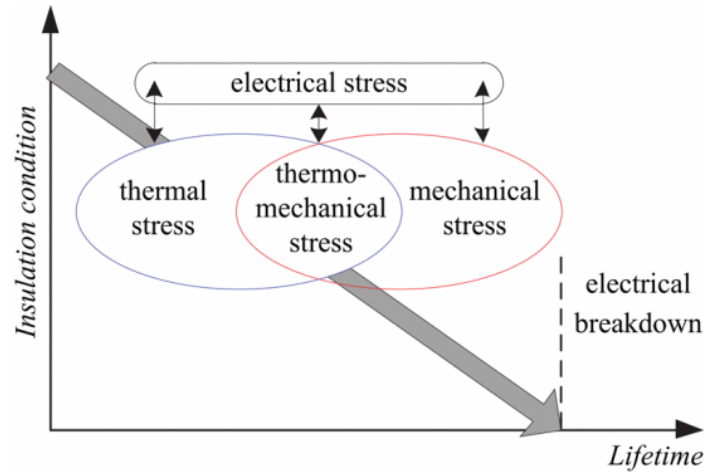• In [75],[84] electrical, thermal and mechanical stress act simultaneously and synergistically. The ageing process of the insulation system can be shown in Fig.3.13:

Fig.3.13: Aging mechanism of electrical insulation on stator bars [75]

Despite electrical breakdown serving as the final failure mechanism and indicating the end of the lifespan of electrical insulation materials, electrical stress does not constitute the primary ageing factor. Instead, the breakdown process is primarily linked to thermal and mechanical stress. Consequently, the foremost ageing factor is the thermal degradation of the binder resin due to thermal stress, augmented by mechanical stress induced by vibration and thermomechanical stress stemming from variations in the thermal expansion coefficients of the materials involved.

The synergy effect of thermal and mechanical stress accelerates the ageing process of the electrical insulation system, leading to a shortened lifespan. This interaction exerts a greater impact on the insulation system compared to the mere summation of individual ageing factors due to their nonlinear characteristics (Fig.3.14).
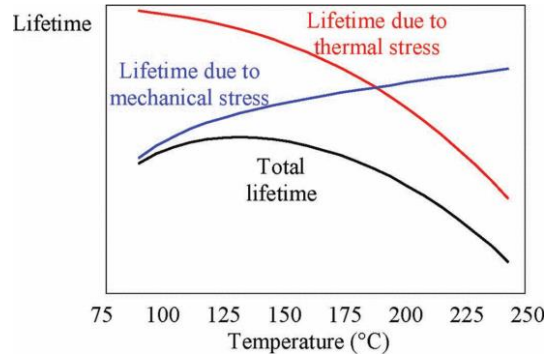
Fig.3.14: Lifetime as Influenced by Thermal, Mechanical, and Their Synergistic Interaction [84]

The ageing process under thermal, mechanical, and electrical stress typically leads to an initial extension of the lifetime until a specific temperature threshold is surpassed, triggering a sudden decline thereafter.

These trends are primarily driven by the progressive thermal degradation of organic matter on one front, while on the other, they are influenced by the diminishing internal stress and the formation of cracks in the binder resin at elevated temperatures.

The diagnostic procedure for assessing electrical insulation can be outlined as follows:
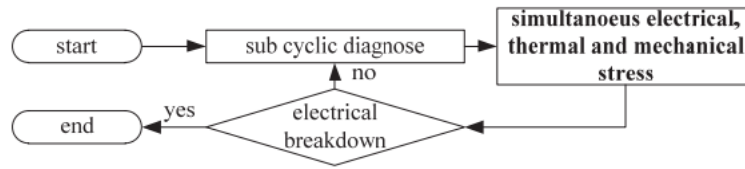

Fig.3.15: Diagnostic Testing Procedure for Electrical Insulation [75]

The diagnostic tools utilized for condition monitoring of electrical insulation encompass:

a) Amplitude-frequency spectrum: The emphasis was on the behaviour of the peak, which shifts to lower frequencies as the multistress ageing time increases, while its amplitude also increases throughout the multistress ageing process.

b) tanδ: The dissipation factor, represented as a function of relative voltage V_{test}/V_r, exhibits an increase as the multistress ageing time extends.

c) Partial Discharge: The phase-resolved PD pattern was observed by leftward skewness in phase and polarity symmetry, indicating the likelihood of delamination and voids. Skewness (S_k) characterizes the asymmetry of a distribution relative to the

normal distribution, with $S_k = 0$ indicating symmetry, $S_k > 0$ suggesting asymmetry with a larger left side, and $S_k < 0$ indicating asymmetry with a larger right side.

- In [80], [81], [83], a thorough three-phase multi-stress methodology is employed. It utilizes a model stator to evaluate the performance of two new stator bars subjected to simultaneous electrical, thermal, and mechanical stresses. To monitor the insulation condition, the following diagnostic tests were conducted at room temperature.

a) Partial Discharge Tests: Results include discharge intensity in the three-phase model stator bars, recording partial discharges in voids within the bars, slots, and exposed stator bar ends. Maximum charge transfer ΔQ_m values increased before and after the ageing test for bars from both tested groups under twice the rated applied voltages. These values are associated with discharges in voids within the insulating systems. Additionally, ΔQ_m values indicate a reduction in PDIV during ageing. The decrease in PDIV post-aging test implies an inverse correlation between ΔQ_m and PDIV, suggesting higher ΔQ_m values correspond to lower voltages where PD pulses become detectable. The reduction in PDIV and the rise in ΔQ_m in partial discharge pulses suggest some deterioration in the stator bar specimens.

However, these changes don't accurately predict the remaining lifetime in the stator bars. Previous attempts to correlate partial discharge intensity with insulation life failed, as establishing a reliable PD intensity threshold for predicting insulation failure proved challenging. Even close to insulation failure, PD pulse intensity may increase, remain constant, or decrease. Stator bar insulation degrades slowly. Stator bars often operate with some level of partial discharge, and even when the semiconducting layer is eroded, there may be little or no visible sign of insulation sublayer damage.

Changes in PDIV and ΔQ_m values recorded at room temperature on stator bar specimens before and after accelerated ageing tests didn't align with ac breakdown strength values on the stator bars. This confirms that decreases in PDIV and increases in ΔQ_m are not reliable indicators of the remaining life of aged bars. In contrast, the ac breakdown voltage (Vb) of the stator bar is a useful indicator of the ageing rate. It can be employed to shorten accelerated ageing data for bars that haven't experienced

failure, indicating the end of their lifespan when the breakdown voltage reaches the level of the operating voltage.

b) Breakdown Voltage: The breakdown voltage diagnostic method illustrates the average AC breakdown voltage for aging bars and the actual AC breakdown voltages of two temperature-monitoring bars. A significant decrease in the average ac breakdown voltage is observed when the bar specimens undergo a more intense thermal load cycle and elevated mechanical stress as a result of the heightened thermal stress. However, the extent of this difference compared to untested virgin bars is uncertain, as they were not available for testing. The comparison is based on AC breakdown values from the temperature-monitoring bars, which experienced the same thermal cycles as the specimen bars in both groups and were not subjected to voltage stress. This comparison reveals a slightly lower average ac breakdown voltage in the bar specimens, suggesting the presence of ageing in both bars.

The slight reduction in the specimen, although noticeable, suggests that the remaining life expectancy of bars AC breakdown voltage of the is still considerable, even with the rigorous thermal load cycling. This indicates the resilience of the insulating system in the tested stator bars. Despite the partial degradation due to partial discharges, there seems to be no significant damage to the insulating system, highlighting its robustness. While the occurrence of partial discharges indicates ongoing degradation, the recorded discharge intensity does not exhibit a clear correlation with the remaining life of the stator bars.

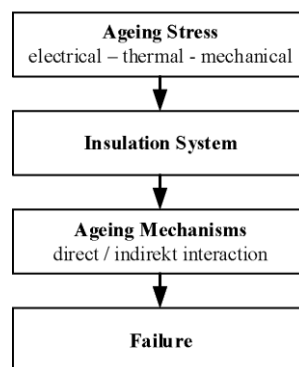- In [78] the ageing procedure of the insulation system is depicted in Fig. 3.16:

Fig.3.16: Ageing Procedure

The setup for the accelerated ageing test includes a mechanical stress exciter, a circulating air oven for thermal stress, and a single-phase transformer for electrical stress (Fig.3.17).
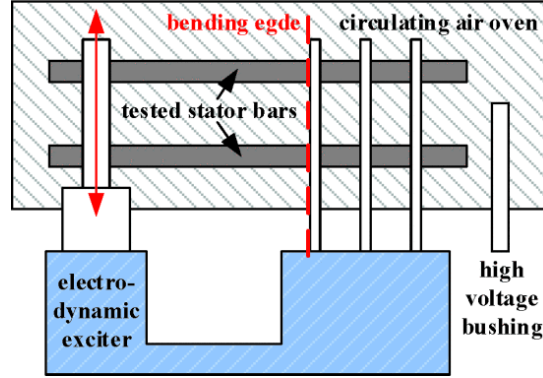

Fig.3.17: Test Set-Up

The primary ageing factors in this process involve mechanical and thermomechanical ageing, with electrical voltage utilized solely for determining the end of the lifespan through electrical breakdown. In this study, diagnostic tools were not employed to monitor the insulation system's condition. Instead, the authors estimated the lifetime data of multifactor ageing, using the natural logarithm of lifetime *ln(L)* as a function of mechanical and thermomechanical stresses. They arrived at a correlation *ln(L) = f(x,y)*, where *x* represents deflection (mm) related to mechanical stress, and *y* denotes temperature (Celsius). The study explored scenarios where either x remained constant while y changed or vice versa, observing the effects on lifetime. Additionally, they developed a lifetime model, *f(x, y, z) = ln(L),* incorporating thermal, electrical, and mechanical stress variables along with deflection *(x in mm)*, temperature *(y in Celsius),* and voltage *(z in V).* The authors employed bootstrap distribution to evaluate the impact of each ageing method.

- The same ageing test procedure as described in [78] was implemented in [76]. In this test, mechanical stress levels were adjusted by varying alternating bending amplitudes, while electrical and thermal stresses were held constant. The diagnostic method used to assess insulation condition involved amplitude-frequency analysis.

Amplitude-frequency characteristic: The main peaks in the amplitude-frequency graph were split in the case of aged samples at high frequencies, accompanied by a reduction in amplitude. This split is attributed to cracking and delamination.

- In [86] the procedure entails the concurrent application of electrical and thermal stress, followed by the application of thermomechanical and mechanical vibration stresses. Thermal stress is induced by placing specimens in an oven, while electrical stress is applied using a transformer. Mechanical vibration stress is applied using a sinusoidal vibration with a frequency of 100Hz and an amplitude of 1mm (peak-to-peak). Thermomechanical stress, on the other hand, is induced through thermal cycling.

The consequences of these stresses include thermal degradation from prolonged exposure to high temperatures, insulation abrasion due to vibrations induced by magnetic fields, thermomechanical degradation from sudden load fluctuations, and electrical degradation resulting from PD within air gaps in the coil-to-core insulation. Non-destructive testing was conducted on specimens following a complete ageing cycle.

a) Partial Discharge: Analysis of PD quantities showed an increase in specific PD-derived parameters with ageing, suggesting a transition from small to larger insulation defects over time. This implies that initially, small defects are more common, but as ageing continues, larger defects become predominant. Furthermore, the morphology of voids within the coil-to-core insulation evolves over time, transitioning from a flat to a narrow configuration, potentially manifesting as treeing— a phenomenon characterized by the formation of gas-filled channels branching out from pre-existing voids, cavities, and manufacturing imperfections. These channels propagate through the material, facilitated by various mechanisms such as partial discharge (PD) occurring at regions of elevated electrical stress [87]. The presence of treeing poses a significant risk, as it can lead to deterioration of the insulation and ultimately cause electrical breakdown or failure.

b) Dissipation Factor: The characteristic of the dissipation factor versus the applied voltage is shown in Fig.3.18:
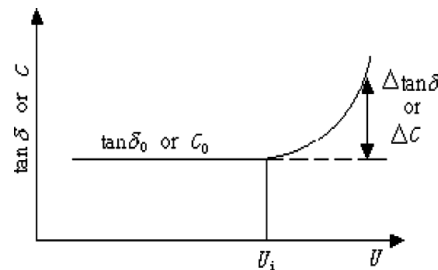

Fig3.18: Illustration of Dissipation Factor and Capacitance Increase with Applied Voltage

To make the above graph more understandable, the parameters C_0 and $tan\delta_0$ pertain to capacitance and dissipation factor under low voltage, while parameters C_e and $tan\delta_e$ relate to capacitance and the dissipation factor under nominal operating conditions. Lastly, ΔC and $\Delta tan\delta$ represent the increase in capacitance and dissipation factor, respectively, as derived from the equations C_e-C_0/C_0 and $\Delta tan\delta=(tan\delta_e-tan\delta_0)/tan\delta_0$.

The dissipation and capacitance of the specimens increased with increasing applied voltage at different temperatures. The observed curves resemble those in Fig.3.17, suggesting partial discharge (PD) within the coil-to-core insulation of stator bars under operational voltages, regardless of the temperature. Additionally, the tip-ups of the dissipation factor and capacitance increase with ageing.

- In [85] a synergistic combination of thermal, mechanical, and electrical breakdown is presented. This test identifies the end of the component's lifetime through the occurrence of electrical breakdown resulting from these stresses. The ageing process was conducted on two types of coils: backup coils and dummy coils. The condition of the insulation system was assessed through the dissipation factor and partial discharge pattern analysis.

a) Dissipation Factor (DF): Under normal operating conditions, the impact of applied voltage on the system is minimal. The variance in tan δ values observed in the backup coil before and after multiple ageing cycles is attributed to moisture and post-curing effects on the insulation during this timeframe. Additionally, for backup coils, there is a slight decline in tan δ as the load cycle number increases. Notably, a difference in the tan δ versus voltage profile is noticeable between service-aged and backup coils. In service-aged coils, tan δ increases at operation voltage, indicative of a greater presence of voids and delaminations compared to backup coils, where tan δ remains constant. This rise is linked to the activity of partial discharge (PD).

b) Partial Discharge: Initially, the PD levels detected in the backup coils exceeded those in the service-aged coils, possibly due to moisture content. Subsequently, both backup and service-aged coils exhibited considerable variability in PD magnitudes during the initial thermal cycles, likely caused by static charge accumulation in voids. As time progressed, the PD magnitudes declined, potentially

indicating a shift in discharge mechanisms. The disappearance of PD activity after a certain number of load cycles may be attributed to pseudo-glow discharge occurring in enclosed cavities, which poses challenges for detection with conventional PD detectors. Following 200 thermal cycles, there was an upsurge in PD magnitude observed in the service-aged coils, indicating the onset of PD activity at specific weak points within the insulation. Eventually, during further testing, the insulation of the service-aged coil punctured, possibly due to an increase in voids and delaminations. During the off-cycle, PDIV was measured every 50 thermal load cycles for both the backup and service-aged coils. Initially, the backup coil displayed a lower PDIV than the service-aged coil. However, after 150 and 200 thermal cycles, the PDIV values for the backup coils were observed to be higher compared to those for the service-aged coil.

- In [88], the study introduces a multifactor ageing test, the sequence of which is illustrated in Fig.3.19:
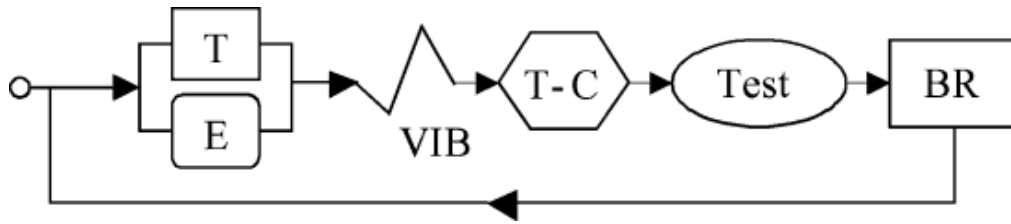
Fig3.19: Test sequence of accelerated ageing test, T: thermal stress, E: electrical stress, VIB: mechanical vibration, T-C: thermal cycling test, Test: Test parameters, BR: breakdown test [88]

The multistress ageing process involves the simultaneous application of thermal and electrical stress, achieved through an oven and a transformer, respectively. Mechanical vibration stress is then applied to the specimens using a sinusoidal vibration force at 100Hz. Subsequently, the specimens undergo thermal cycling in another oven. After each ageing cycle, some of the samples are subjected to breakdown testing to determine their breakdown voltage.

a) Partial Discharge: This study highlights the crucial role of statistical parameters in evaluating insulation ageing, elucidating distinct patterns during multistress ageing. Specifically, the skewness values of PD distributions undergo a shift from positive to negative as ageing progresses, where lower skewness values signify more pronounced insulation ageing. Furthermore, while the maximum PD

magnitude q_{max} typically increases with ageing, its utility as a sole indicator is diminished due to significant dispersion in test results.

b) Breakdown Test: An observable trend of decreasing breakdown voltage is evident throughout multistress aging, despite the significant variability observed in the breakdown test results. This finding serves to confirm the efficacy of multistress accelerated ageing techniques.

3.3.3.2 Electrical-Thermal-Mechanical Stress on Formette

As described in [82] is an accelerated test setup that simultaneously exposes test coils in formette to electrical, mechanical, and thermal aging. Mechanical stress is administered through a shaker table with a maximum payload capacity of 2500 lbs. Thermal stress is induced by multiple strip heaters on both sides of each slot to replicate operational conditions. Electrical stress is applied using either a power supply delivering 60 Hz of AC power or a high-frequency pulse generator, allowing for a comparison of their effects. Following the ageing process, diagnostic tools are utilized to evaluate the insulation condition.

a) PF tip-up: The findings reveal that the tip-up value is greater for HF results than for 60 Hz results. Nevertheless, the variations in tip-ups for the insulation material under the same test conditions (HF or 60 Hz) are negligible.

b) Partial Discharge Tests: PD values in mV for various insulation combinations (S1-S3) consistently remained low during testing at the 60 Hz power frequency. However, when subjected to HF impulses, one insulation group exhibited significantly higher values, despite employing the same insulation combinations as in the 60 Hz power frequency tests. This highlights the more pronounced impact of HF testing on insulation compared to power frequency testing at 60 Hz.

c) Hot spot temperatures: This metric denotes the highest temperature recorded in the monitored coils during the multi-stress testing with different insulation configurations(S1-S3). Notably, minimal differences were observed when using the 60 Hz power frequency source. In contrast, under HF test conditions, all coil temperatures substantially increased, revealing more significant variations between materials.

The findings suggest that while many selected insulation systems passed individual tests, the percentage of coil failures notably rose in the simultaneous test group. This affirms that the simultaneous stress test is a more rigorous evaluation, providing a superior representation of real operating conditions where mechanical, thermal, and electrical stresses occur concurrently.

3.3.4 Thermal-Ambient-Mechanical Stress

In [79] statorettes were chosen as the testing apparatus. They comprise a single coil of magnet wire wound around an appropriate number of turns within a small frame featuring two slots (Fig.3.20).

Fig.3.20: Statorette

All statorettes undergoing testing are immersed in dielectric oil, an integral component of the design that requires careful consideration. Placed within a pressure vessel, the temperature and pressure are meticulously controlled to specific levels. These thermal and pressure stresses are endured by the statorettes for a predetermined duration, which begins with a 21-hour exposure period. Following exposure, the test set is extracted from the pressure vessel and allowed to cool to a consistent ambient temperature. Subsequently, the statorettes are subjected to mechanical stress by vibrating at a specified rate and magnitude for a set period. Currently, this involves vibrating at 60Hz with an approximate amplitude of 8 mils peak to peak for 20 minutes. After the exposure and cooling phases, a diagnostic assessment is conducted on the statorettes. This diagnostic evaluation involves subjecting each unit to a voltage check. The objective of this test is not to induce electrical ageing of the insulation but rather to verify that the thermal damage sustained has not exceeded a predetermined threshold. Statorettes that successfully withstand the short-term test are reintroduced into the pressure vessel for another round of exposure. This process is iterated until all statorettes within a test set eventually fail. All the procedure described is summarized in Fig.3.21:
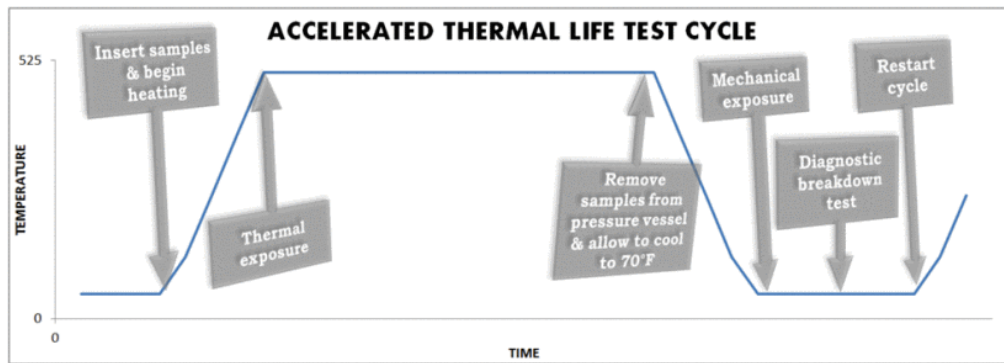
Fig.3.21: Test sequence

The authors examined the insulation condition by constructing a plot depicting the lifetime of insulation as a function of temperature, as well as generating a normal distribution of its lifespan.

3.3.5 Electric-Mechanical-Thermal-Ambient Stress

In a multifactor accelerated ageing experiment outlined in [77], coils were exposed to electrical stress, mechanical stress, temperature variations, and fluctuations in ambient humidity. These factors, with electrical stress being the primary cause of insulation ageing, substantially contribute to the ageing process. Following each sub-period of the experiment, non-destructive measurements were conducted. The test sequence, depicted in Fig.3.22, encompassed 22 periods.
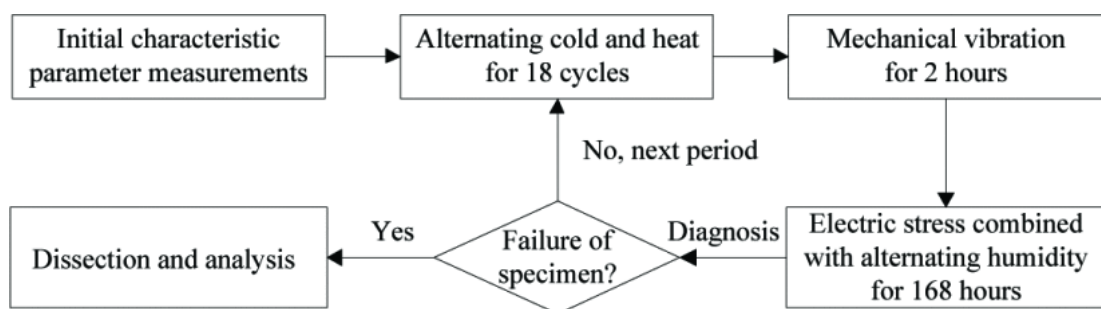
Fig.3.22: Multifactor ageing test procedure

At the end of each multi-factor accelerated ageing period, which involved two coils, several non-destructive diagnostic tests were conducted, including assessments of the Dissipation Factor, Insulation Resistance, and PDIV.

a) Dissipation Factor: Following a large number of ageing cycles, during which there was a notable increase in applied voltage due to electrical stress, the dissipation

factor exhibited a significant rise. The coil showing the greatest increase in DF also displayed the weakest insulation system.

b) Insulation Resistance: The insulation resistances of the two specimens were measured using DC voltage, and their values were compared across ageing cycles. Analysis of the provided figure revealed that electrical stress did not notably hasten the decline in insulation resistance during the initial 16 periods. However, thereafter, the resistance decreased significantly, dropping by four orders of magnitude in one coil and by four in the other.

c) PDIV: The amplitude of the PDIV is not evident for either specimen in each ageing period. Throughout the entire ageing cycle, the PDIV only experienced a slight decrease.

Chapter 4: Equivalent Model Development and Prognosis-Diagnosis via FRA

Permanent magnet motors need to handle high currents in the armature winding to sustain a high torque density, making the health of the insulating system critical. For the current project, segmented stator poles and their mounted armature (Fig.4.1) have been disassembled to study their behaviour under multiparametric ageing (Chapter 5) using offline methods such as Impedance Spectroscopy and Nyquist diagrams. Observing the poles' behaviour during the ageing process provides insight into how their health is affected by real ageing conditions. However, it is not always feasible to determine the underlying cause behind the motor's ageing and potentially catastrophic failure. To address this, an equivalent model of the poles was constructed (Section 4.1) based on experimental measurements, providing a highly accurate approximation of their healthy state. This model enables the assessment of the poles' performance during their construction process to ensure they meet expected standards. Additionally, by observing parameter variations through Impedance Spectroscopy and Nyquist diagrams, the model can provide information on which parameters of the equivalent circuit lead to the corresponding waveform resulting from the ageing of the specimens, facilitating both prognosis and diagnosis.
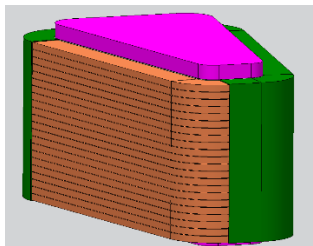
Fig.4.1: Stator poles with the mounted armature coil

4.1 Development of Equivalent Pole Model

To establish a comprehensive equivalent model of the pole (Fig.4.2), a series of experimental measurements were undertaken to calculate all necessary parameters required (Table 4.1).
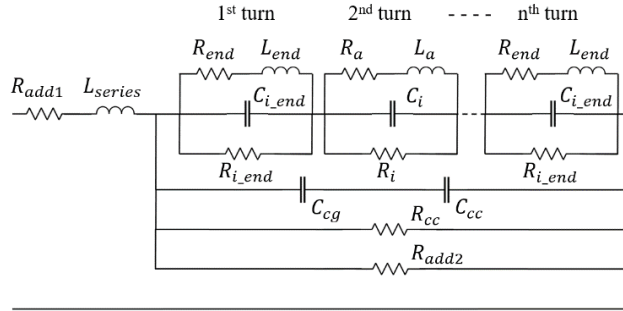
Fig.4.2: Equivalent Model of Pole

R_{add1}	Additional resistance due to the circuit wiring.
L_{series}	In-series inductance due to the instrument augmented by 1 turn's inductance.
R_{end}	Internal turn resistance of the first and last turns of the coil.
L_{end}	Inductance of the first and last turns of the coil.
C_{i_end}	Capacitance between the 1st and 2nd turn of the coil.
R_{i_end}	Insulation resistance between 1st and 2nd turn of the coil.
R_a	Internal turn resistance.
L_a	Single turn inductance.
C_i	Capacitance between two turns of the coil.
R_i	Insulation resistance between two turns of the coil.
C_{cg}	Added capacitance aiming at measurement correction
C_{cc}	Capacitance between the core and coil.
R_{cc}	Insulation resistance between the core and the coil.
R_{add2}	Shunt resistance of the impedance spectroscopy

Table 4.1: Equivalent Circuit Parameters

All intermediate turns exhibit shared characteristics concerning resistance R_a, L_a, C_i, and R_i, except for the end turns (first and last turn), which are influenced by end effects. Experimental measurements were conducted to determine the characteristics of the intermediate turns. Furthermore, a concise overview of the estimation of end effects, along with a discussion on additional parameters arising from the measurement setup, is included.

4.1.1 Intermediate Turn Parameters

- *Internal turn resistance - R_a*

The coil's internal resistance was measured using an ohmmeter. However, given the high frequencies reached by the impedance spectroscopy measurements, the skin effect [92] must be accounted for. Therefore, the resistance was calculated for each frequency step, as depicted in Fig.4.3. Here, l represents length, σ denotes conductivity, ρ signifies resistivity, w indicates width, t stands for thickness, and δ represents the skin effect depth $\delta = \frac{1}{\sqrt{\pi f \mu \sigma}}$. The critical frequency at which the skin effect occurs is calculated as: $f_{se} = \frac{4}{\pi \mu \sigma} \left(\frac{w \cdot t}{w+t} \right)^2$.
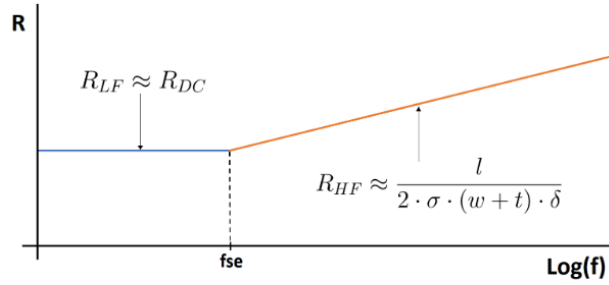
Fig.4.3: Skinn effect impact on internal resistance

- *Coil Inductance (L_a):*

The coil inductance was determined using an impedance spectroscopy analyser. A total of 95 poles were measured to ensure robust statistical analysis, and the average inductance was calculated for incorporation into the model.

- *Insulation Capacitance between Turns (C_i):*

To calculate the capacitance between coil turns, a series of 10 copper bars, each coated with PAI insulation and derived from the same coil wire, was employed. The procedure unfolds as follows: a pair of these bars is inserted into dedicated ducts within a specially crafted enclosure (Fig.4.4). Positioned perpendicular to one another, they create a square contact area, facilitated by their identical width. This configuration permits both vertical movement of the first bar and horizontal movement of the second, thereby establishing multiple points of contact. Stripped of their PAI insulation at the ends, these bars function as electrical contact points for the impedance spectroscopy electrodes.
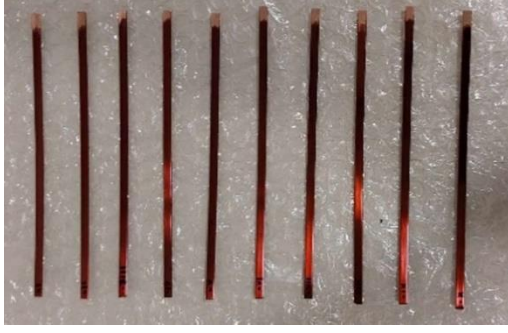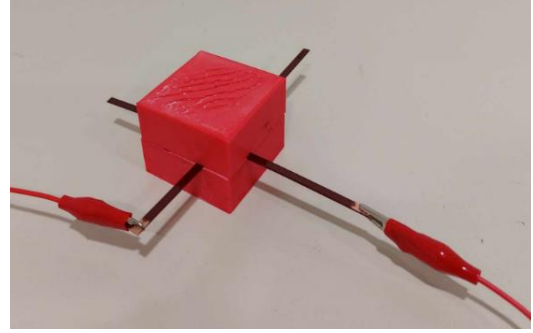
Fig: 4.4: (a) Copper wire specimens, (b) Capacitance measurement between turns set-up

Impedance spectroscopy, along with its corresponding phase, was conducted based on 80 measurements taken (Fig.4.5). A frequency of 80 kHz was uniformly chosen for all samples because, at this frequency, the phase closely approximates -90°, indicating ideal capacitor behaviour in the circuit. Therefore, by obtaining the impedance value X_c using the equation $|X_c| = \frac{1}{\omega C}$, where $\omega = 2\pi f$ and C represents capacitance. Thus, the equation can be solved for $C = \frac{1}{\omega |X_c|}$ and the average capacitance values across the sample set can be determined.
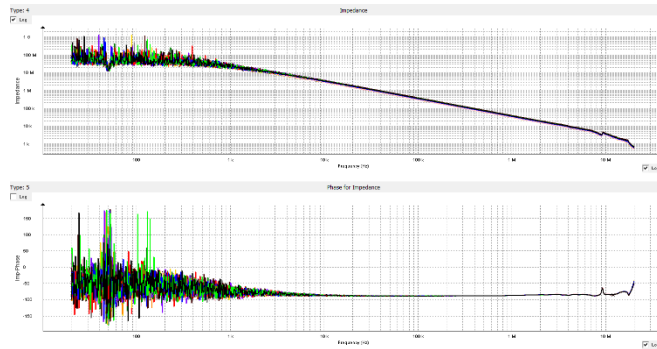
Fig. 4.5. Impedance spectroscopy of the contact area between couples of bars

- *Turn-to-Turn Insulation Resistance (R_i):*

For the purpose of this measurement, a set of 10 bars was utilized, divided into 5 pairs. Each pair of bars was placed inside a shielding case in parallel ducts, with a copper thin plate positioned atop, intersecting both bars. Subsequently, each pair of bars was connected in parallel, with their ends short-circuited on one end, and on the other end, they were in contact with the copper plate. The measurement setup (Fig.4.6) was established by connecting the terminals to the short-circuited end and to the copper plate. This connection was made to reduce their combined resistance R_t, as the insulation resistance was too high to measure accurately. The measurement result provides information on both resistances. To find the resistance of each bar, it was

assumed that the resistances of the bars are equal, considering they are made of the same material and have same dimensions. Thus, by equating the two parallel resistances $R_t = \frac{R_{i1}R_{i2}}{R_{i1}+R_{i2}} = \frac{R_i^2}{2R_i} = \frac{R_i}{2}$, we obtained the resistance value for each bar R_i.

For the resistance measurements of the bars, a Megohmmeter 15kV was employed, with the IR test setting adjusted for a duration of 8 minutes to ensure precise measurement and stabilize the resistance value (Fig.4.7).
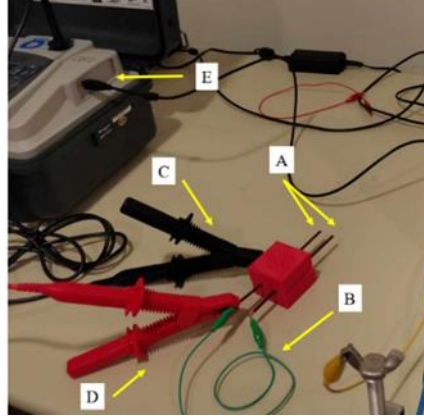

Fig. 4.6: Insulation Resistance Measurement set-up: A) the two copper bars, B) the short circuit at one end of the bars, C) electrode connected to the copper plate on top of the bars, D) electrode connected to the shorted end of the bars and E) the Megohmmeter producing high voltage.
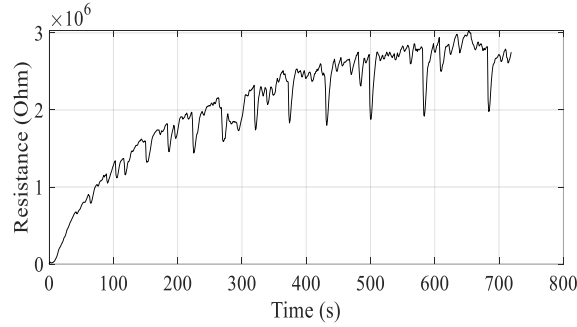
Fig.4.7: Insulation Resistance Test measurement

- *Insulation Resistance between Coil and Core (R_{cc}):*

The poles were positioned above the copper plate, and the terminals of the Megohmmeter were connected, with one at the stripped end of the coil and the other at the pole's contact point with the copper plate. For the measurement, the IR test setting was chosen, and the measurement time was set to 14 minutes, as within that time frame, the resistance stabilized for all the pole samples measured. Statistical analysis was conducted on the results from 95 poles, and the mean resistance value was determined with the aim of integrating it into the model.

- Insulation Capacitance between Coil and Core (C_{cc}):

The same test setup used for the R_{cc} measurement was also employed for the calculation of C_{cc}. However, instead of using a Megohmmeter, impedance analyser was utilized. The impedance and phase diagrams were examined similarly to the C_i measurement, and the capacitance was calculated such that the phase angle approximates ~-90°.

4.1.2 End-Turn Parameters

- C_{iend}: The capacitance of the end turns, which varies due to the fringing effect, is derived from Eq.4.1 according to [93]

$$C = \frac{\varepsilon_0 \varepsilon_r w l}{g} + \frac{\pi \varepsilon_0 \varepsilon_r (l+w)}{\ln\left(\frac{\pi}{2}\left(1+\frac{g}{t}\right) + \sqrt{\frac{\pi^2}{4}\left(1+\frac{g}{t}\right)^2 - 1}\right)} \qquad (Eq.4.1)$$

where: w and l are the width and length of the capacitor plates respectively, g is the distance between the plates and t is the thickness of the plates

- L_{iend}: The end turns of coils do not complete a full turn, resulting in a difference in inductance from the intermediate turns by a factor k_L, $L_{iend} = k_L \cdot L_a$

- R_{iend}: The end turns of coils do not complete a full turn, resulting in a difference in resistance from the intermediate turns by a factor k_R, $R_{iend} = k_R \cdot R_a$

4.1.3 Additional Parameters

Finally, utmost importance was placed on calculating parameters corresponding to the experimental equipment, including the additional resistance due to circuit wiring R_{add1}, in-series inductance due to the instrument augmented by one turn's inductance L_{series}, added capacitance for measurement correction C_{add}, and the shunt resistance of the impedance spectroscopy R_{add2}.

4.1.4 Frequency Response Analysis

After calculating all the parameters comprising the equivalent circuit, frequency response analysis was performed using the impedance spectroscopy method (Fig.4.8). The real and imaginary parts of the impedance spectroscopy were then utilized to construct Nyquist diagrams (Fig.4.9). Subsequently, these plots were compared with

the corresponding ones obtained from experimental measurements conducted over healthy poles to verify the accuracy of the model.

The low-frequency resonance (peak) refers to the point where the inductive and capacitive reactions are approximately equal, while the high-frequency resonance (spike) is attributed to the asymmetries of the end-turns.
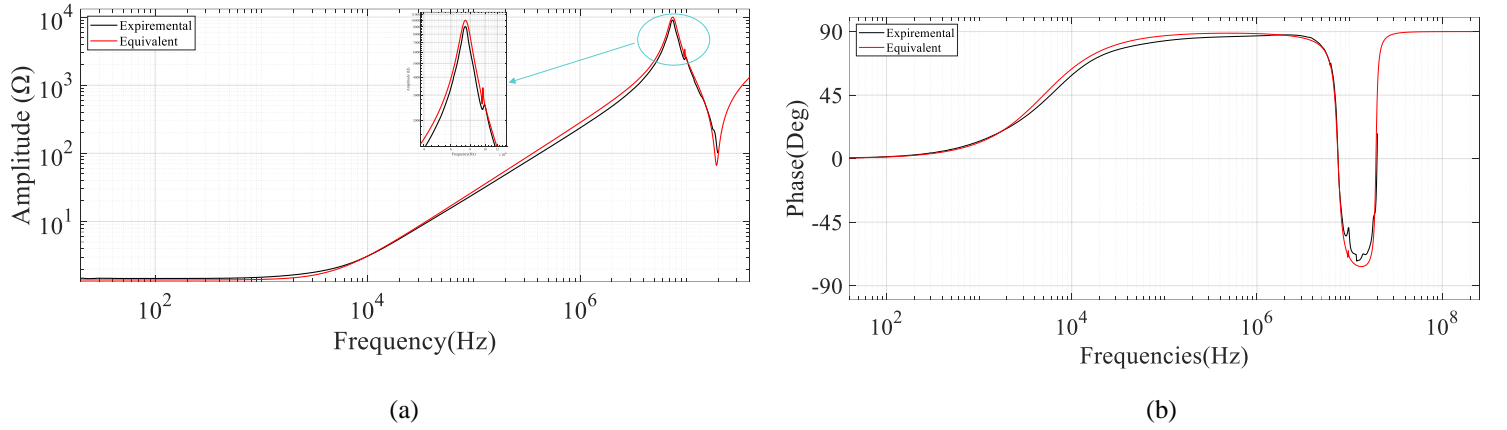

(a)   (b)

Fig.4.8: Impedance spectroscopy of the complete equivalent circuit model (red) and the experimentally measured pole (black) where: a) the impedance and b) the phase.
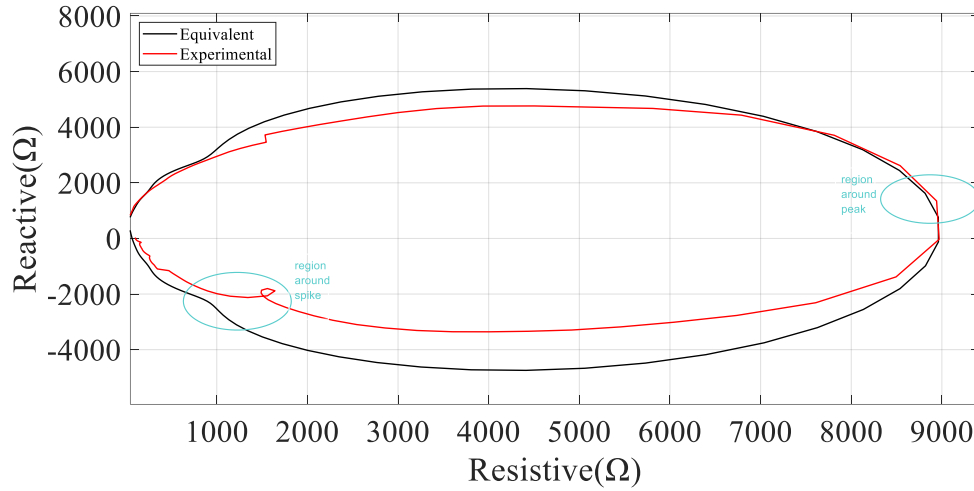
Fig.4.9 Nyquist Diagram of the complete equivalent circuit model (red) and the experimentally measured pole (black).

4.2   Frequency Response Analysis with Varied Equivalent Model Parameters for Prognosis and Diagnosis

In this section, an illustration will be provided of how the changes in parameters resulting from the aging, as detailed in Section 5 (derived from literature search), will influence the behavior of the equivalent model in impedance spectroscopy and Nyquist plots. This analysis aims to facilitate prognosis and diagnosis.

4.2.1 R_{cc} variations

The resistance may decrease until reaching a critical point, and then increase due to the introduction of air bubbles into the insulation, a result of delamination. The decrease in resistance will result in a reduction in both the width of the peak and the spike area. Conversely, an increase in resistance will lead to an increase in both the width of the peak and the resonance. All these changes can be seen in (Fig.4.10a, and Fig.4.10b). Regarding the Nyquist diagram, a decrease in impedance is observed as resistance decreases and an extension when the resistance increases again (Fig.4.10c). Moreover, there is no observed shift either in the Nyquist diagram or in the impedance spectroscopy.

(a)

(b)
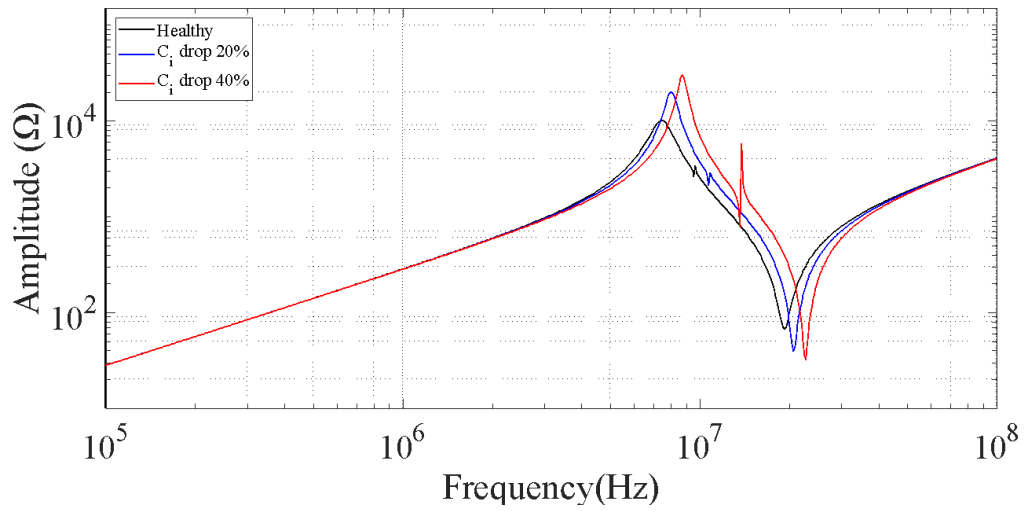
(c)
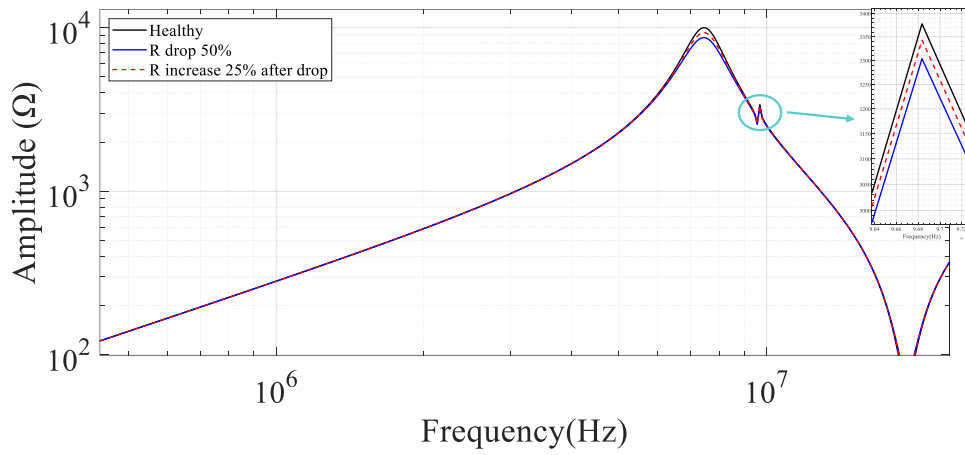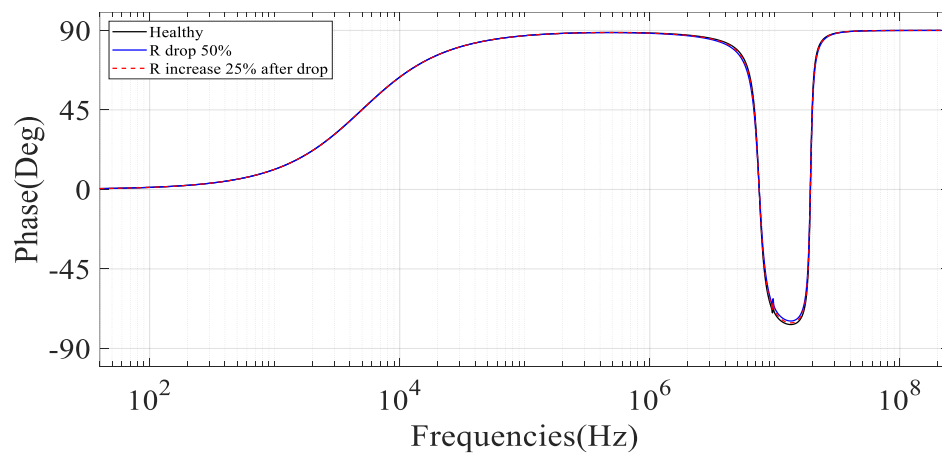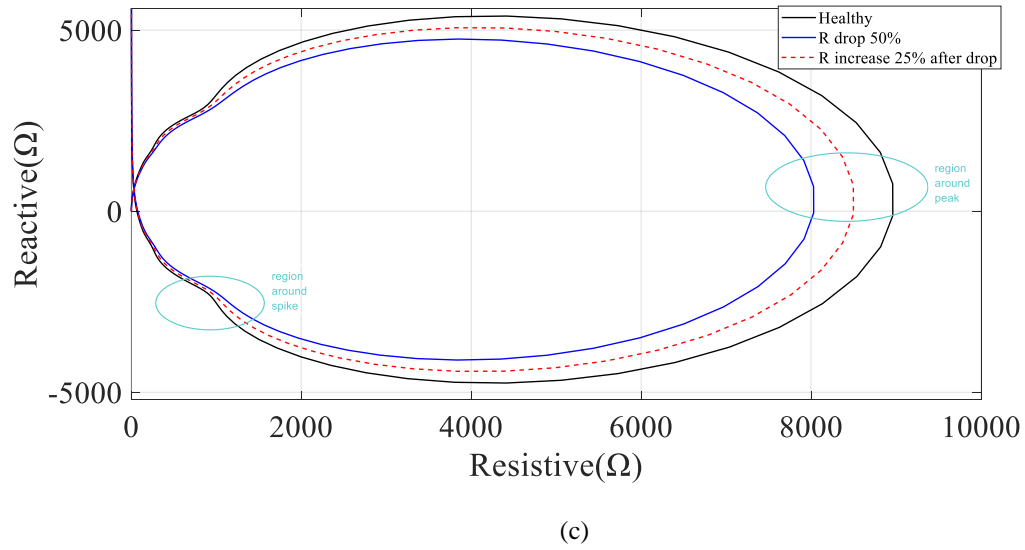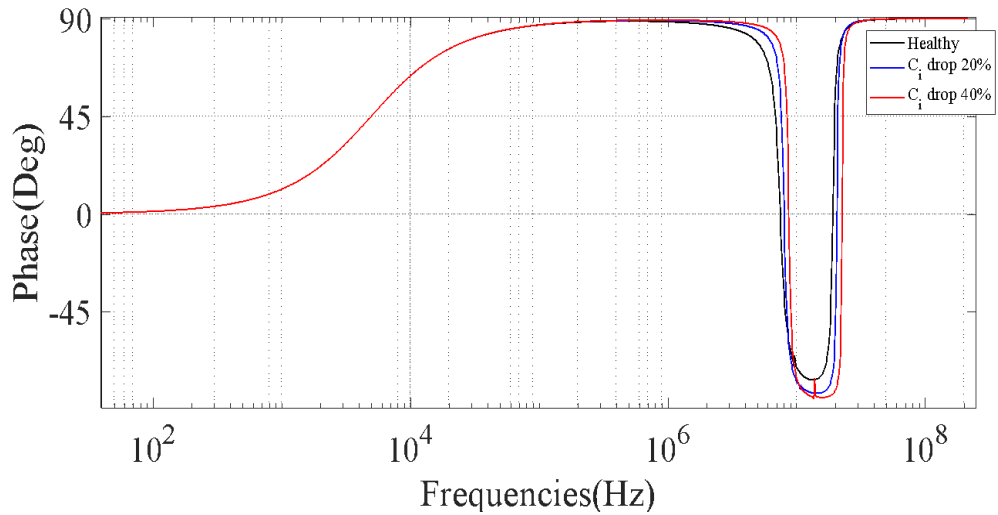
Fig.4.10: Impedance spectroscopy & Nyquist plot where: a) the impedance, b) the phase and c) the Nyquist Plot.

4.2.2 C_{cc} reduction

A reduction in coil-to-core capacitance may occur as a consequence of insulation overheating, leading to undesirable delamination or desiccation of the insulation material. This phenomenon introduces air or gas within the insulation, consequently reducing the effective dielectric constant. Consequently, this decline in capacitance will augment the capacitive behaviour of the circuit, given that capacitance is inversely proportional to capacitive reactance.

Implication on Impedance Spectroscopy Results (Fig.4.11a, Fig.4.11b):σ

- The low-frequency resonance (peak) shifts to the right, accompanied by a simultaneous upward displacement.

- The width of the high-frequency resonance (spike) increases.

Implication on Nyquist Plot Results (Fig.4.11c):

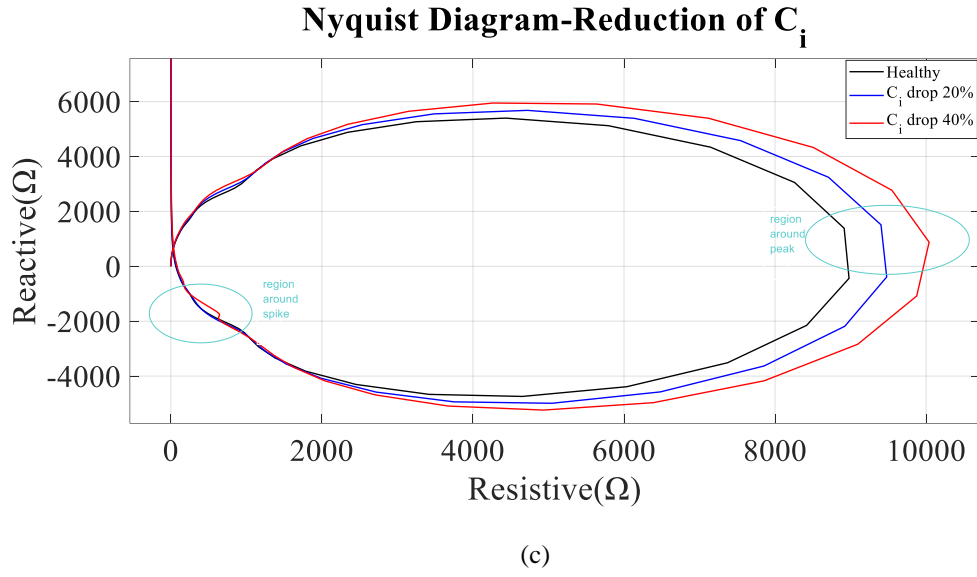- The ellipsis expands.
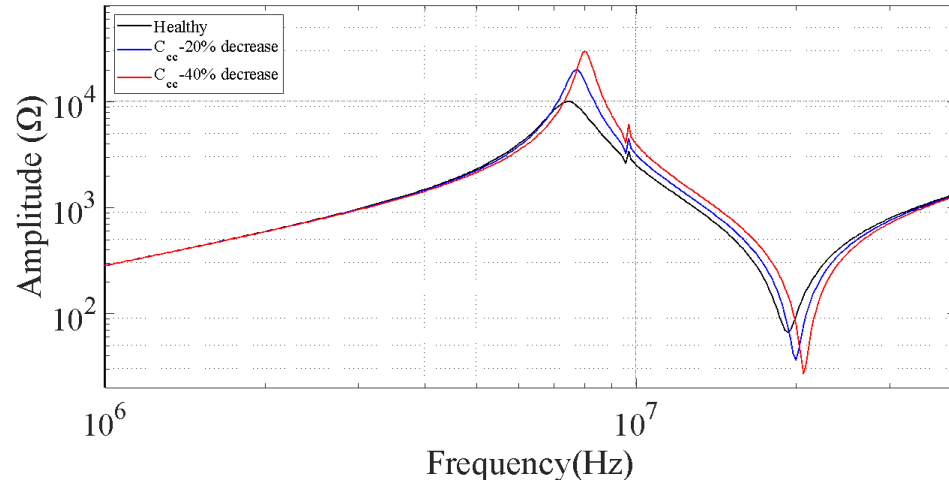
(a)
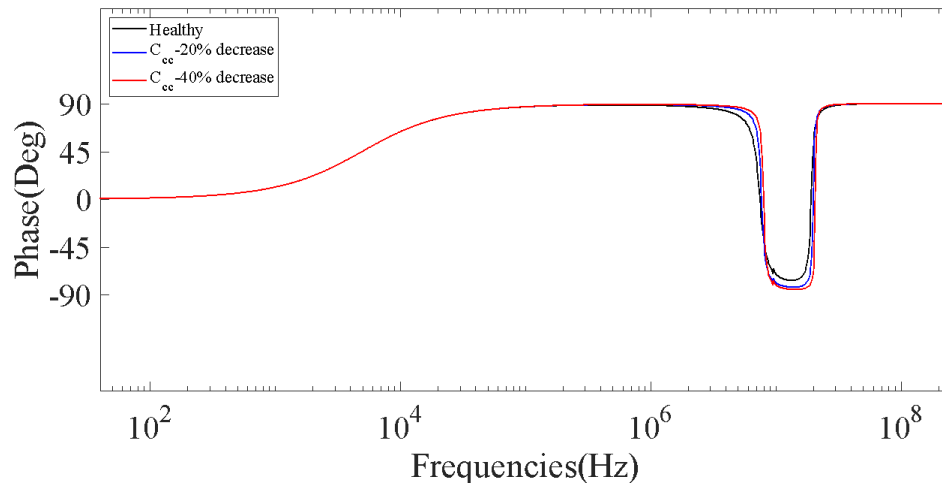
(b)
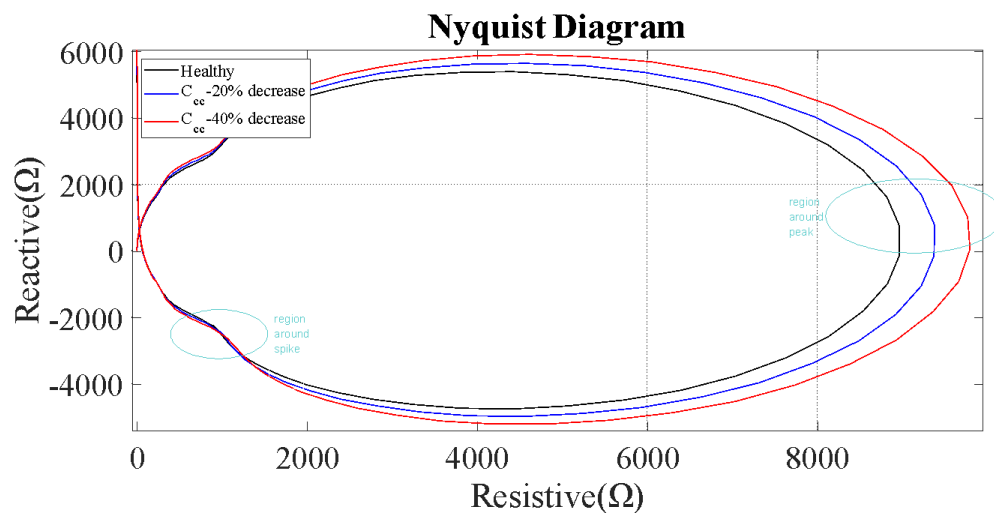
(c)

Fig.4.11: Impedance spectroscopy & Nyquist plot in case of C_{cc} reduction where: a) the impedance, b) the phase and c) the Nyquist Plot.

4.2.3 C_{ins} reduction

The turn-to-turn capacitance may decrease due to air being introduced between the turns of coils. The consequences of this change are apparent in the impedance spectroscopy results (Fig.4.12a, Fig4.12b), which indicate a concurrent right shift and increase in amplitude the characteristic curve and an expansion of the Nyquist diagram (Fig.4.12c), accompanied by a simultaneous downward displacement of the ellipse.

(a)

(b)

Nyquist Diagram-Reduction of C_i

(c)

Fig. 4.12: Impedance spectroscopy & Nyquist plot in case of C_i reduction where: a) the impedance, b) the phase and c) the Nyquist Plot.

4.2.4 L_a variations

The inductance may change in case of an inter-turn fault since the current direction will change in the faulty turn due to Faraday's law of induction. However, the exact mechanism of inductance variation due to an actual short circuit is out of the scope of this master thesis investigation and will not be influenced by the ageing methods employed in Section 5.

4.2.5 R_{ins} reduction

The reduction of R_{ins} due to ageing has not had an impact on both Impedance spectroscopy and Nyquist plots.

4.2.6 C_{iend} reduction

If the outer coil turn is bent, possibly induced by mechanical vibration, it can lead to an increased distance between the first and second turns, causing air to fill the gap due to the bending. Consequently, this will result in a reduction of the capacitance C_{iend}. From the impedance spectroscopy results (Fig.4.13a and Fig.4.13b), a right shift is observed in the case of low resonance (spike). This change is also depicted in the Nyquist diagram (Fig.4.13c), where the component with the lowest capacitance exhibits less capacitive behaviour, as it shifts more towards the upper left.
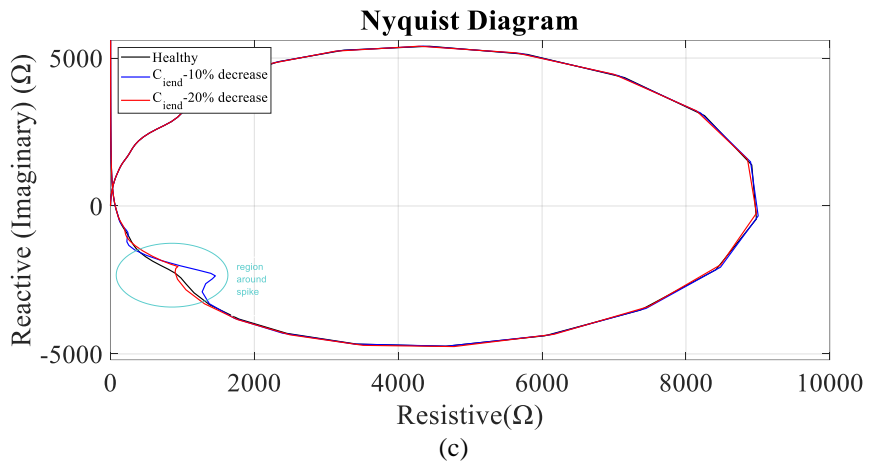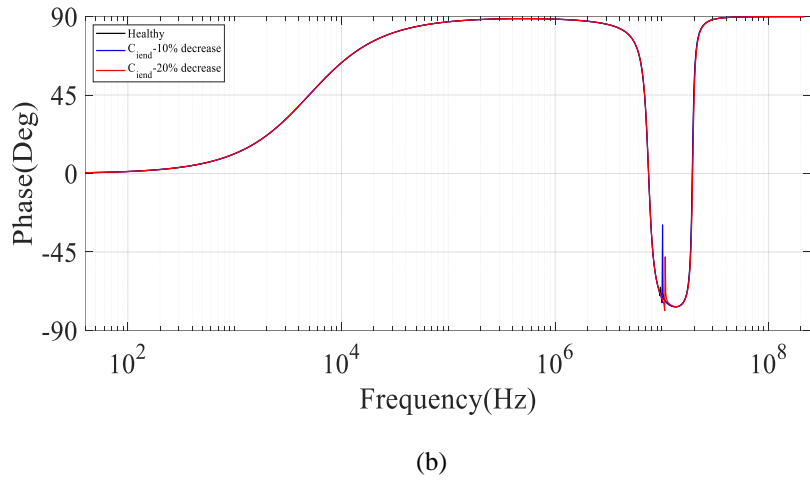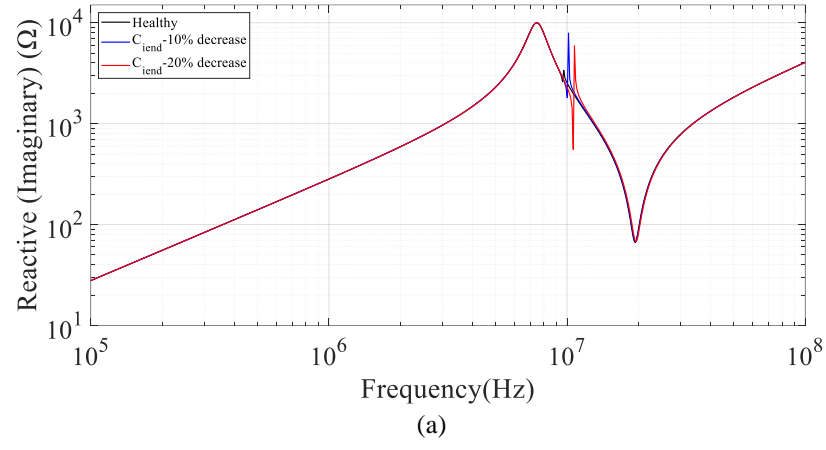
(a)

(b)

(c)

Fig. 4.13: Impedance spectroscopy & Nyquist plot in case of C_{iend} reduction where: a) the impedance, b) the phase and c) the Nyquist Plot.

Chapter 5: Experimental Multifactor Ageing

In this chapter, the impact of multistress ageing on the poles under investigation will be examined. Section 5.1 will outline the general procedure for implementing multistress on the studied poles and describe the experimental test setup used. Section 5.2 will present the results of the multistress experiments conducted, while Section 5.3 will discuss the overarching findings regarding the behaviour of poles during ageing . Lastly, Section 5.4 will discuss potential areas for future research.

5.1   Experimental Setup and Multistress Procedure
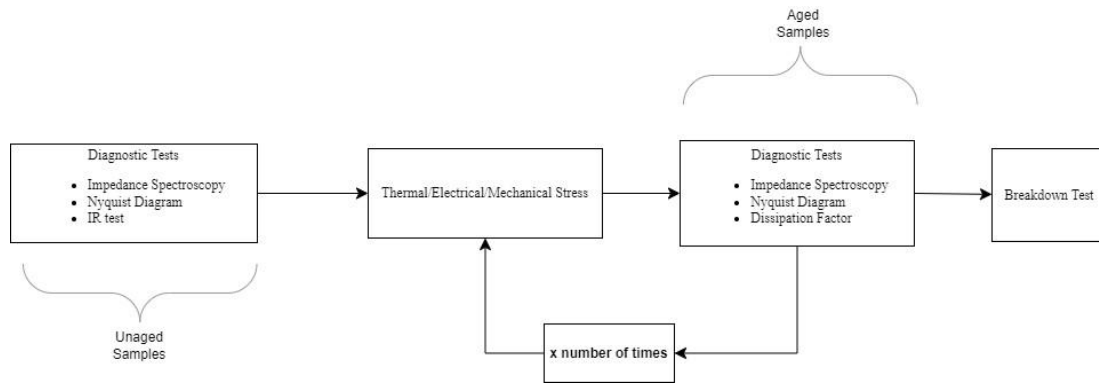
Fig.5.1: General Multistress Procedure

<u>Diagnostic Tests:</u> The tests were conducted at two stages: firstly, during the initial, unaged state of the specimens deemed as healthy, and subsequently following the application of stress resulting in ageing. Impedance spectroscopy determined the pole's equivalent impedance and phase in relation to frequency. Then, utilizing it through the Nyquist curve with the representation of the real and imaginary parts of the impedance provides additional information regarding the circuit's behaviour. Both tests do not affect the measurement. As for the IR test used to find the resistance between the pole and the core of the stator, it influences the overall resistance and more specifically the capacitance due to the absorption current confusing the capacitance meter, resulting in a capacitance reading that is much larger than it actually is. Therefore, the influence of the IR test must be taken into account, and impedance spectroscopy and the Nyquist diagram should be performed again since the pole's

characteristics have changed, and it is no longer in its healthy state. As for tanδ, it does not affect the measurement and is carried out separately by each stress cycle to show how its characteristic varies with frequency in each cycle. To find the relationship leading to the calculation of tanδ as a function of frequency increase, the following study was conducted [94]-[97]:

In terms of frequency f and angle θ, the complex AC impedance Z^* can be expressed in terms of real Z' and imaginary Z'' components through the relationship

$$Z^* = Z' - iZ''$$

where:

The interrelation between the dielectric constant ε', representing the relative dielectric constant (ε_r) indicating the degree of polarization, and the dielectric losses ε'', signifying the imaginary permittivity representing the dielectric loss factor, can be elucidated through the dissipation factor *tanδ* (Eq.5.1). This relationship enables the utilization of the real and imaginary impedances calculated previously, thus giving the dissipation factor ultimately as the ratio of these impedances and consequently as a function of frequency.

$$\varepsilon' = Z'/2\pi f C_0(Z'^2 + Z''^2)$$
$$\varepsilon'' = Z''/2\pi f C_0(Z'^2 + Z''^2)$$

$$tan\delta = \frac{\varepsilon''}{\varepsilon'} = \frac{Z''}{Z'} \qquad (Eq.5.1)$$

Breakdown Test: This test was conducted to assess the efficacy of the multistress procedure and also to apply electric stress. The DC ramp mode was implemented with a step of 1000V/min. However, the interpretation of the results necessitates statistical analysis, incorporating the Normal Distribution and/or Weibull Distribution. The likelihood function of the Weibull Distribution is represented by its Probability Density Function (PDF), as defined in Eq. 5.2, while the PDF of the Normal Distribution is derived from Eq. 5.3.

- Weibull Distribution:

$$f(x|a,b) = f(x) = \begin{cases} \frac{b}{a}\left(\frac{x}{a}\right)^{b-1} e^{-\left(\frac{x}{a}\right)^b}, if\ x \geq 0 \\ 0,\ if\ x < 0 \end{cases} \qquad (Eq.5.2)$$

$$a = \left[\left(\frac{1}{n}\right)\sum_{i=1}^{n} x_i^b\right]^{\frac{1}{b}}, b = \frac{n}{\left(\frac{1}{a}\right)\sum_{i=1}^{n} x_i^b log x_i - \sum_{i=1}^{n} log x_i}$$

where x represents the Breakdown Voltage,thus $x \geq 0$

- Normal Distribution:

$$f(x|\mu.\sigma) = \frac{1}{\sigma\sqrt{2\pi}}e^{\frac{-(x-\mu)^2}{2\sigma^2}}, x \in \mathbb{R} \qquad (Eq.5.3)$$

$$\mu = \sum_{i=1}^{n}\frac{x_i}{n}, \sigma^2 = \frac{1}{n-1}\sum_{i=1}^{n}(x_i - \mu)^2$$

where x represents the Breakdown Voltage,thus $x \geq 0$

Thermal Stress (Cycling): The experiments are carried out in oven to replicate the thermal fluctuations experienced by insulating materials during motor operation under varying loads, albeit with minimal deviations. Specifically, temperatures fluctuate between their minimum and maximum values, with a variation of 40 °C, over a duration of eight minutes. The temperature range is chosen to either remain within the operational limits of the windings to simulate normal operating conditions or surpass the maximum operational limit (220°C) to simulate accelerated ageing. Each complete thermal stress process lasts for 6 hours in the case of normal ageing circumstances, while it lasts 3 hours for accelerated ageing.

Thermal Stress(Fixed): To get some information about the thermal ageing impact on the poles, a series of fixed thermal stress cycles was planned. This group of tests aims to provide the actual degradation outcome due to elevated temperature operation without the impact of thermomechanical effects that are present in thermal cycling stressing. This test is conducted in an oven for 6 hours, maintaining a constant temperature throughout.

Mechanical Stress: Besides the fixed thermal stress and thermomechanical stress resulting from thermal cycling, it is important to investigate the impact of mechanical stress as well. Mechanical stress can be of many types and is mainly caused by the various forces developed inside the machine and acting on the conductors. For that purpose, a special device has been developed and shown in Fig.5.2. The device consists of an inverter-fed induction motor, the rotation of which is transformed into linear oscillation.

The inverter is responsible for regulating the frequency of power supplied to an AC motor, thereby controlling the motor's rotation speed. In the absence of an inverter, the AC motor would run at full speed immediately upon power supply activation, rendering speed control unattainable and limiting the motor's applicability. Utilizing an inverter to modulate the speed and acceleration of an AC motor broadens the scope of its applications compared to a motor operating at a fixed speed. In this test setup, a single phase of the inverter's three phases was utilized and connected to the motor. The frequency of the inverter was set at 5Hz. The resulting motor speed is calculated to be 258 rpm through a tachometer. As a control method, V/f control is chosen to regulate the induction motor by supplying a predetermined current to the coil to produce a specific torque output. Consequently, there exists a proportional relationship between the voltage and frequency, which is referred to as the V/f characteristics.
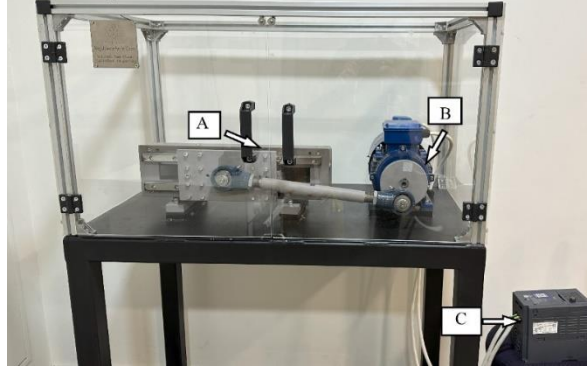
Fig.5.2. Mechanical Stress Test Set-Up, where A: Mechanical Vibration Device, B: Induction Motor, C:Inverter

The transformation of the rotational to linear movement mechanism is depicted in Fig.5.3, wherein the radius R of the disk actuated by the motor, and the length L_δ of the rod are illustrated. The linear oscillation has an amplitude of 40mm, with its acceleration and velocity (Fig.5.4) derived from the following relationships.

$$u_p = R \cdot \omega \cdot \left(sin\omega t - \frac{R}{2L_\delta} \cdot \frac{sin2\omega t}{\sqrt{1-\left(\frac{R}{L_\delta}\right)^2 \cdot sin^2\omega t}} \right) \qquad (Eq.5.4)$$

$$a_p = R \cdot \omega^2 \cdot cos^2\omega t - \frac{R^2}{2L_\delta} \cdot \omega^2 \left(\frac{2cos2\omega t}{\sqrt{1-\left(\frac{R}{L_\delta}\right)^2 \cdot sin^2\omega t}} + \frac{\frac{1}{2}\left(\frac{R}{L_\delta}\right)^2 \cdot sin^2 2\omega t}{\left(\sqrt{1-\left(\frac{R}{L_\delta}\right)^2 \cdot sin^2\omega t}\right)^3} \right) \qquad (Eq.5.5)$$

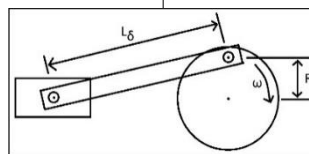Fig.5.3: Linear movement mechanism

R/Lδ	up(m/sec)	ap(m/sec2)
0.090909	0.000000	26.543852
0.090909	0.053070	26.516626
0.090909	0.106030	26.434896
0.090909	0.158773	26.298511
0.090909	0.211188	26.107225
0.090909	0.263165	25.860704
0.090909	0.314593	25.558534
0.090909	0.365362	25.200239
0.090909	0.415357	24.785290
0.090909	0.464465	24.313129
0.090909	0.512571	23.783186
0.090909	0.559558	23.194904
0.090909	0.605311	22.547761
0.090909	0.649710	21.841298
0.090909	0.692636	21.075148
0.090909	0.733970	20.249061
0.090909	0.773592	19.362934
0.090909	0.811382	18.416845
0.090909	0.847220	17.411077
0.090909	0.880987	16.346149
0.090909	0.912566	15.222845
0.090909	0.941840	14.042237
0.090909	0.968697	12.805713
0.090909	0.993027	11.514996
0.090909	1.014723	10.172162
0.090909	1.033683	8.779660
0.090909	1.049810	7.340320
0.090909	1.063015	5.857359
0.090909	1.073213	4.334392
0.090909	1.080328	2.775420
0.090909	1.084293	1.184835
0.090909	1.085050	-0.432599
0.090909	1.082549	-2.071758
0.090909	1.076752	-3.727179
0.090909	1.067633	-5.393081
0.090909	1.055177	-7.063402
0.090909	1.039380	-8.731826
0.090909	1.020255	-10.391820
0.090909	0.997823	-12.036680
0.090909	0.972123	-13.659566
0.090909	0.943204	-15.253554
0.090909	0.911132	-16.811681
0.090909	0.875986	-18.326992
0.090909	0.837858	-19.792593
0.090909	0.796853	-21.201698
0.090909	0.753093	-22.547679
0.090909	0.706709	-23.824116
0.090909	0.657847	-25.024842
0.090909	0.606664	-26.143991
0.090909	0.553329	-27.176042
0.090909	0.498021	-28.115856
0.090909	0.440930	-28.958720
0.090909	0.382254	-29.700376
0.090909	0.322199	-30.337059
0.090909	0.260978	-30.865519
0.090909	0.198811	-31.283048
0.090909	0.135921	-31.587501

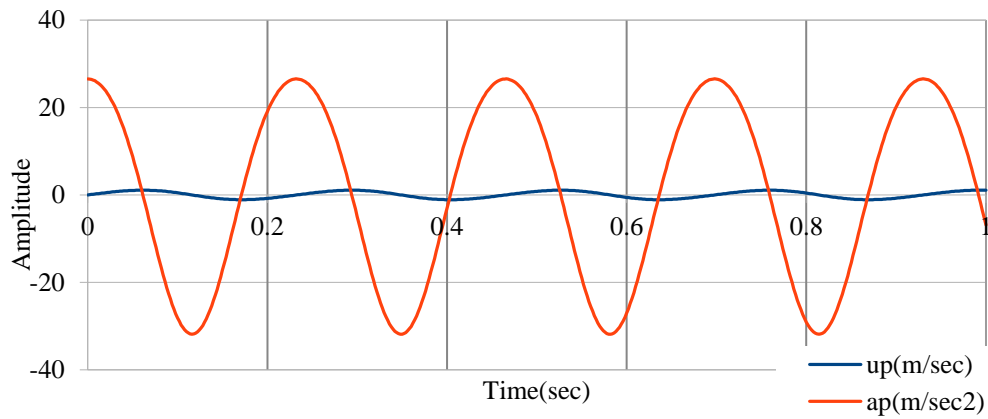Table 5.1: Acceleration and Velocity Calculation

Fig.5.4:Acceleration and Velocity of Mechanical Vibration

This pulsating linear movement is provided to a wagon holding 6 poles that are connected in series and shorted. The wagon is moving inside a C-shaped iron chamber which holds a series of magnets along the movement of the wagon (Fig.5.5). Therefore, the poles are not only subjected to a mechanical vibration due to the induction motor but also an EMF is induced due to Faraday's law, leading to an eddy current and in turn Laplace forces at twice the frequency of the oscillation(Eq.2.5).
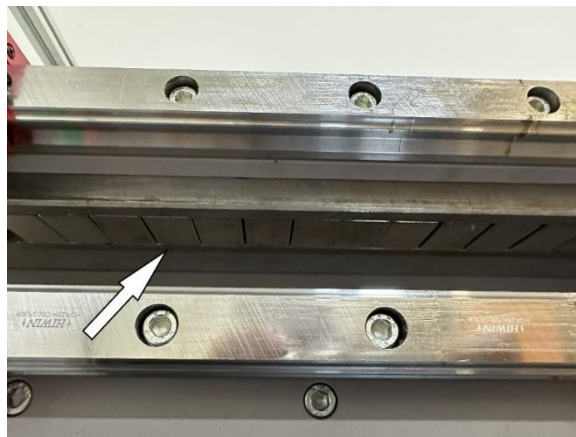

Fig.5.5: Series of magnets inside the C-shaped chamber

5.2   Multistress Experiments and Results

Three multistress procedures were conducted on three distinct sets of poles. The first two involved alternating thermal-mechanical stress, with the distinction that an additional cycle of thermal stress was applied in the second procedure, intensifying its impact. Conversely, the third test incorporated mechanical stress application following multiple cycles of thermal cycling.

5.2.1 Alternating Thermal-Mechanical Stress

The initial group subjected to multistress ageing comprises six poles. The multistress procedure is shown in Fig.5.6. Thermal and electrical-mechanical stresses are the primary ageing factors, with diagnostic tests utilized to assess the ageing process. Breakdown tests are conducted to elucidate how the ageing process impacts breakdown voltage. The accelerated ageing process parameters are shown in Table 5.2.
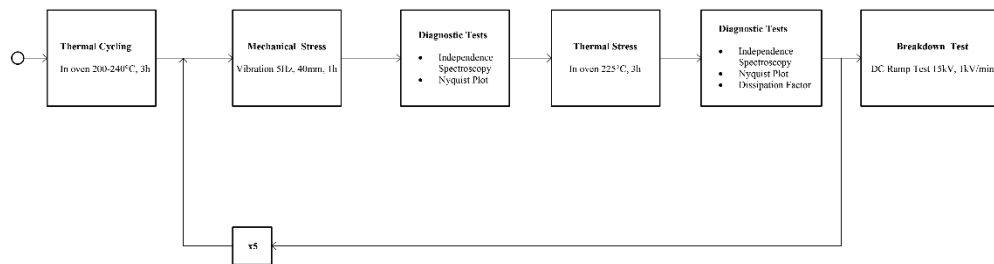

Fig.5.6: Test Procedure

| Stress Type	Duration(hrs)	Stress Parameters
Thermal Cycling	3	200-240°C
Mechanical	1	5Hz (motor)
Thermal Stress-Fixed	3	225°C
Mechanical	1	5Hz (motor)
Thermal Stress-Fixed	3	225°C
Mechanical	1	5Hz (motor)
Thermal Stress-Fixed	3	225°C
Mechanical	1	5Hz (motor)
Thermal Stress-Fixed	3	225°C
Mechanical	1	5Hz (motor)

Table 5.2: Multistress Parameters

The impedance and phase-amplitude across the frequency spectrum are illustrated in Fig.5.7a and Fig.5.7b, respectively. The low-frequency resonance (peak) is situated within a frequency range of 6.9-7.6MHz, while the high-frequency resonance (spike) is observed in the frequency range of 10-10.1MHz. The Nyquist diagram is presented in Fig.5.7c, with the peak indicated by a '+' symbol, nearly aligned with the real axis on the right-hand side of the plot, while the spike region is delineated by the encirclement that appears.
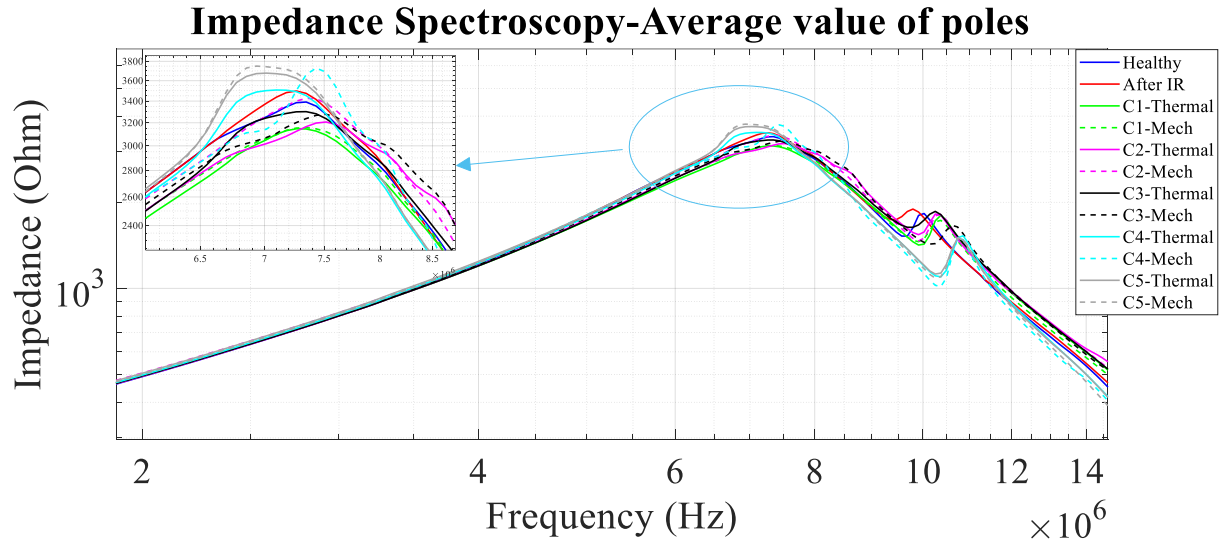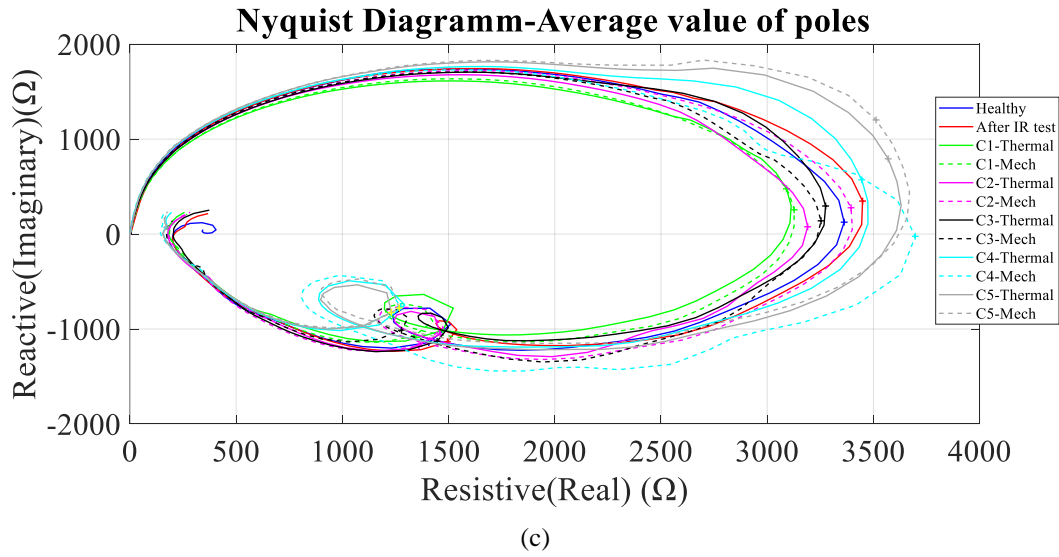

(a)
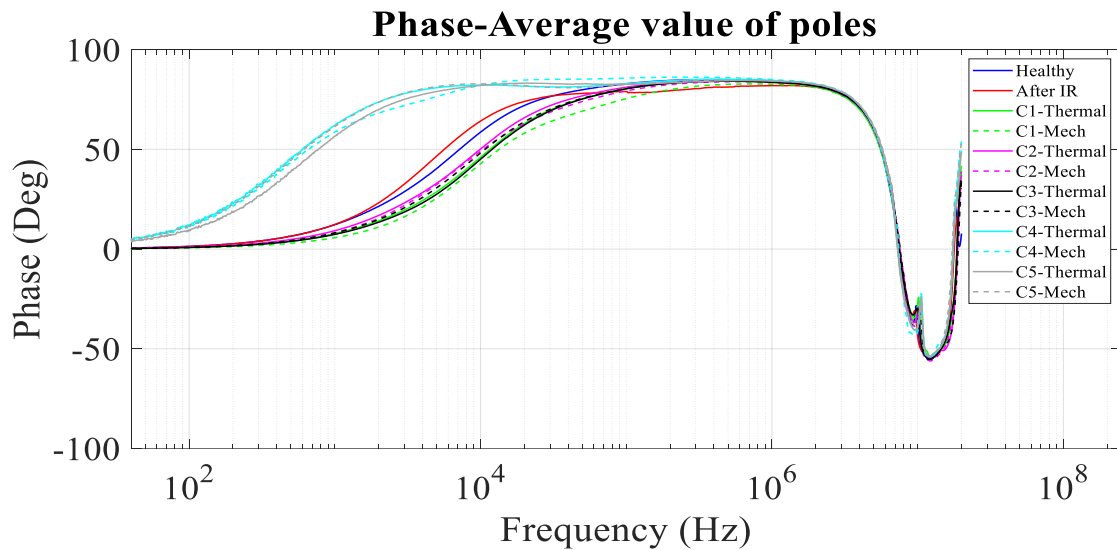
(b)

Fig.5.7: Comparative FRA results, where: (a) Impedance Spectroscopy, (b) Phase, (c) Nyquist Plot

For a better interpretation of the results, the displacements of the peak and the spike between thermal and mechanical stress were depicted in Fig.5.8, and Fig.5.9. Additionally, the magnitudes and phases of these displacements were extracted, along with representations of real and imaginary parts impedance, as summarized in Table 5.3 and Table 5.4 accordingly.
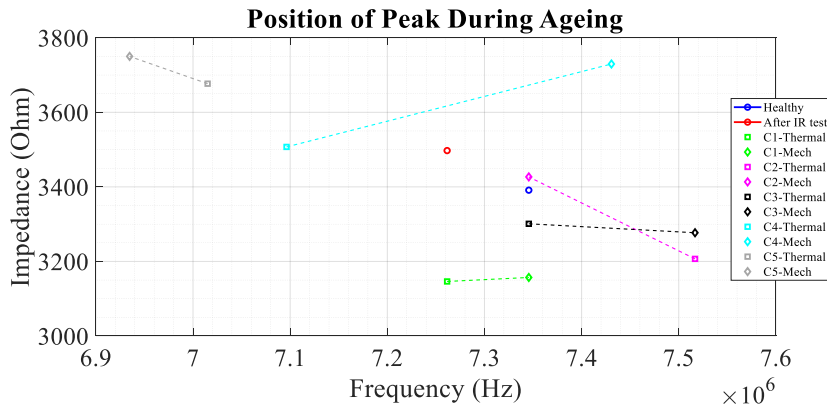

Fig.5.8: Low-Frequency Resonance (Peak) Positions

Cycle	Frequency (Hz)	$\|Z\|{\angle}\varphi$ (Ω)	Real (Ω)	Imag (Ω)
Healthy	7345650	3391.1538∠1.854°	3362.335	124.93
After IR	7261560	3497.369∠5.227°	3448.924	347.274
C1-Therm	7261560	3146.256∠8.33°	3090.86	476.28
C1-Mech	7345650	3157∠4.44°	3127	256
C2-Therm	7516750	3206.849∠1.6469°	3190.44	77.25
C2-Mech	7345650	3426.75∠4.5°	3394.624	277
C3-Therm	7345650	3300.96∠5.159°	3274.94	295.34
C3-Mech	7516750	3276.95∠2.148°	3253.508	139.47
C4-Therm	7096270	3507.18∠9.29°	3445.115	571.36
C4-Mech	7430710	3729.65∠0.15°	3697.027	-23.8
C5-Therm	7015040	3676.818∠11.95°	3569.601	792.39
C5-Mech	6934740	3750.04∠17.669°	3512.516	1201.93

Table 5.3: Low-Frequency Resonance (Peak)

The effect of the IR test is not negligible and leads to an increase in the angle, attributable to the fact that the absorption current confounds the capacitance meter, resulting in a capacitance reading much larger than its actual value. Simultaneously, the resistance increases. Subsequently, during the first cycle of Thermal Stress, the impedance decreases significantly, and the Nyquist diagram shrinks, while the angle continues to increase. This behaviour indicates that the primarily affected element is the resistance, which decreased due to Thermal Stress. Following this, in the first mechanical cycle, an increase in the magnitude and a decrease in the angle are observed, translating to an expansion of the Nyquist curve and a shift towards the negative imaginary part, demonstrating an increase in capacitive behaviour through capacitance reduction. The decrease in capacitance continues into the next thermal cycle (2), attributed to the introduction of air into the insulation, where the dielectric constant of air is lower than that of all solid insulation materials, resulting in a decrease in capacitance according to the parallel plate equation. Consequently, there is an increase in the circuit's capacitive behaviour, as evidenced by the shift and expansion of the Nyquist curve and an increase in impedance. After the second mechanical cycle, the resistance and Nyquist curve increase significantly. This may be related to the appearance of local delamination due to thermal deterioration from thermal stress, which introduced air bubbles into the insulation, likely increasing its resistance. Subsequently, in the third cycle, the resistance decreases due to thermal ageing. However, in the fourth thermal cycle, it is evident that local delamination has significantly intensified, with a rapid increase in impedance and, consequently, the Nyquist diagram, attributable to the resistance increase due to R_{air}, until the fourth mechanical cycle causes cracks in the insulation, evident from the change in shape of the peak, which split as a result of the insulation crack. Moreover, this split in the peak may be attributed to permanent alterations in the insulation material caused by delamination. Overall, the fourth cycle represents a critical threshold where delamination escalates significantly in severity, leading to insulation cracks and permanent changes in the insulation material. Following this, in the fifth cycle, we immediately observe a decrease in resistance, indicating that the insulation has separated from the copper, resulting in a decrease in its resistance. The characteristics of the pole are completely altered due to the crack and delamination after the fourth cycle.
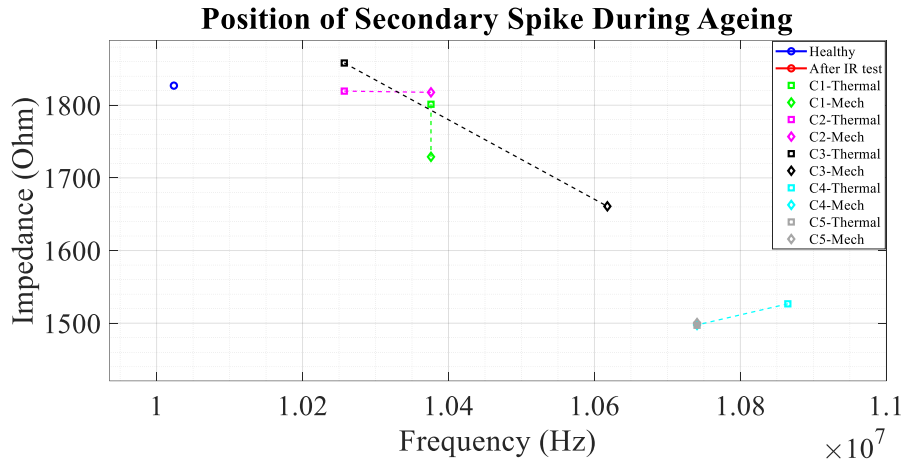
Fig.5.9: High-Frequency Resonance (Spike) Positions

Cycle	Frequency (Hz)	$\|Z\|\angle\varphi$ (Ω)	Real (Ω)	Imag (Ω)
Healthy	10023700	$1826.95\angle -38.577°$	1406.6	-1142.987
After IR	9795580	$1892.931\angle -36.55°$	1494.507	-1134.55
C1-Therm	10376000	$1801.335\angle -34.12°$	1473.349	-1014.98
C1-Mech	10376000	$1729\angle -38.324°$	1338	-1075
C2-Therm	10257200	$1819.43\angle -35.328°$	1461.326	-1054.3578
C2-Mech	10376000	$1817.73\angle -40.284°$	1360.529	-1178.99
C3-Therm	10257200	$1858.12\angle -37.283°$	1446.284	-1129.597
C3-Mech	10617700	$1660.87\angle -37.313°$	1278.51	-1013.146
C4-Therm	10865000	$1526.67\angle -38.7129°$	1174.59	-956.156
C4-Mech	10740600	$1497.61\angle -30.727°$	1274.626	-765.48
C5-Therm	10740600	$1497.19\angle -31.19°$	1230.8938	-826.192
C5-Mech	10740600	$1500.19\angle -33.49°$	1268.012	-779.058

Table 5.4: High-frequency resonance(spike)

Regarding the spike, which is attributed to end-effects phenomena occurring in the pole, until the third thermal cycle, it exhibits some relatively minor fluctuations. The decrease in amplitude is due to a decrease in resistance, while the increase is attributed to a reduction in capacitance due to the introduction of air into the insulation. However, during the third mechanical cycle, a notable observation is the significant decrease in impedance. This decrease can be attributed to the detachment of the PAI insulation from the copper, which occurs as a result of mechanical vibrations and delamination.

By using Eq.5.1, the dissipation factor as a function of frequency is computed (Fig.5.10) following each complete cycle of multistress (thermal and mechanical). This approach aims to comprehensively illustrate the overall impact of multistress as a method.
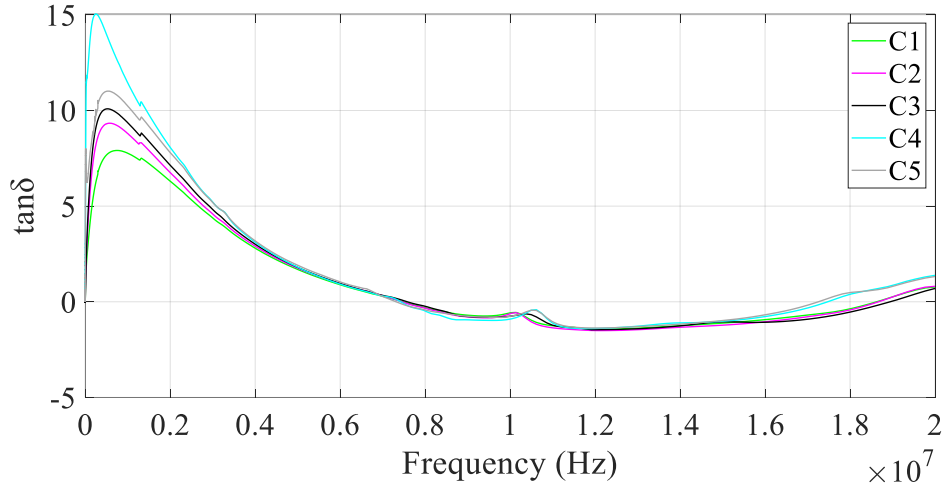

Fig.5.10: Dissipation Factor versus Frequency

Initially, as the frequency increases, a peak becomes apparent. This peak can be explained by the increasing polarization losses with rising frequency. For instance, orientation polarization increases as dipoles respond more rapidly to the electrical field at higher frequencies. This effect persists until a certain frequency, at which the peak appears. It is noteworthy that not only polarization loss, but also conductance loss (attributed to free charge carriers), becomes evident at these frequencies. However, with further increases in frequency, polarization fails to keep pace with the changing electric field. Consequently, polarization loss decreases, leading to a reduction in tanδ.

As the ageing cycle progresses, the dissipation factor increases within frequencies ranging from 0 to 4 MHz, a phenomenon attributed to the formation of delamination and air-filled voids in the insulation. Notably, the peak area of the dissipation factor demonstrates that cycle 4 exhibits the highest dissipation factor, verifying that this cycle consists a critical threshold where chemical changes in the insulation occur, where delamination and cracks are happening, leading to a possible damage in the insulation system. Additionally, there is a shift in tanδ, indicating a decrease in capacitance attributed to the presence of air bubbles in the insulation. This shift is evident both at the main peak and at a local peak observed at 10MHz.

The second team of poles to undergo multi-stress ageing consists of 18 poles. The accelerated ageing process is shown in Table 5.5 and Fig.5.11.
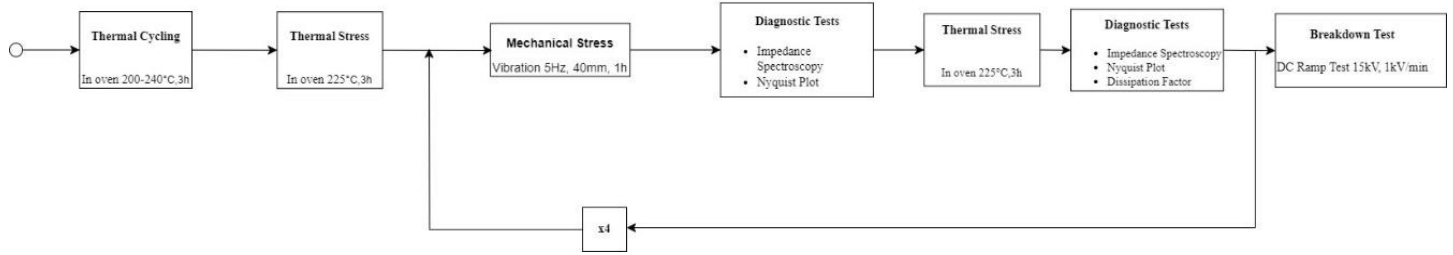

Fig.5.11: Test Procedure

Stress Type	Duration(hrs)	Stress Parameters
Thermal Cycling	3	200-240°C
Thermal Stress-Fixed	3	225°C
Mechanical	1	5Hz (motor)
Thermal Stress-Fixed	3	225°C
Mechanical	1	5Hz (motor)
Thermal Stress-Fixed	3	225°C
Mechanical	1	5Hz (motor)
Thermal Stress-Fixed	1	225°C
Mechanical	3	225°C

Table 5.5: Multistress Test Parameters

The impedance and phase amplitude across the frequency spectrum are illustrated in Fig.5.12a and Fig.5.12b, respectively. The low-frequency resonance (peak) is situated within a frequency range of 6.9-7.6MHz, while the high-frequency resonance (spike) is observed in the frequency range of 10-10.1MHz. The Nyquist diagram is presented in Fig.5.12c, with the peak indicated by a '+' symbol, nearly aligned with the real axis on the right-hand side of the plot, while the spike region is delineated by the encirclement that appears.
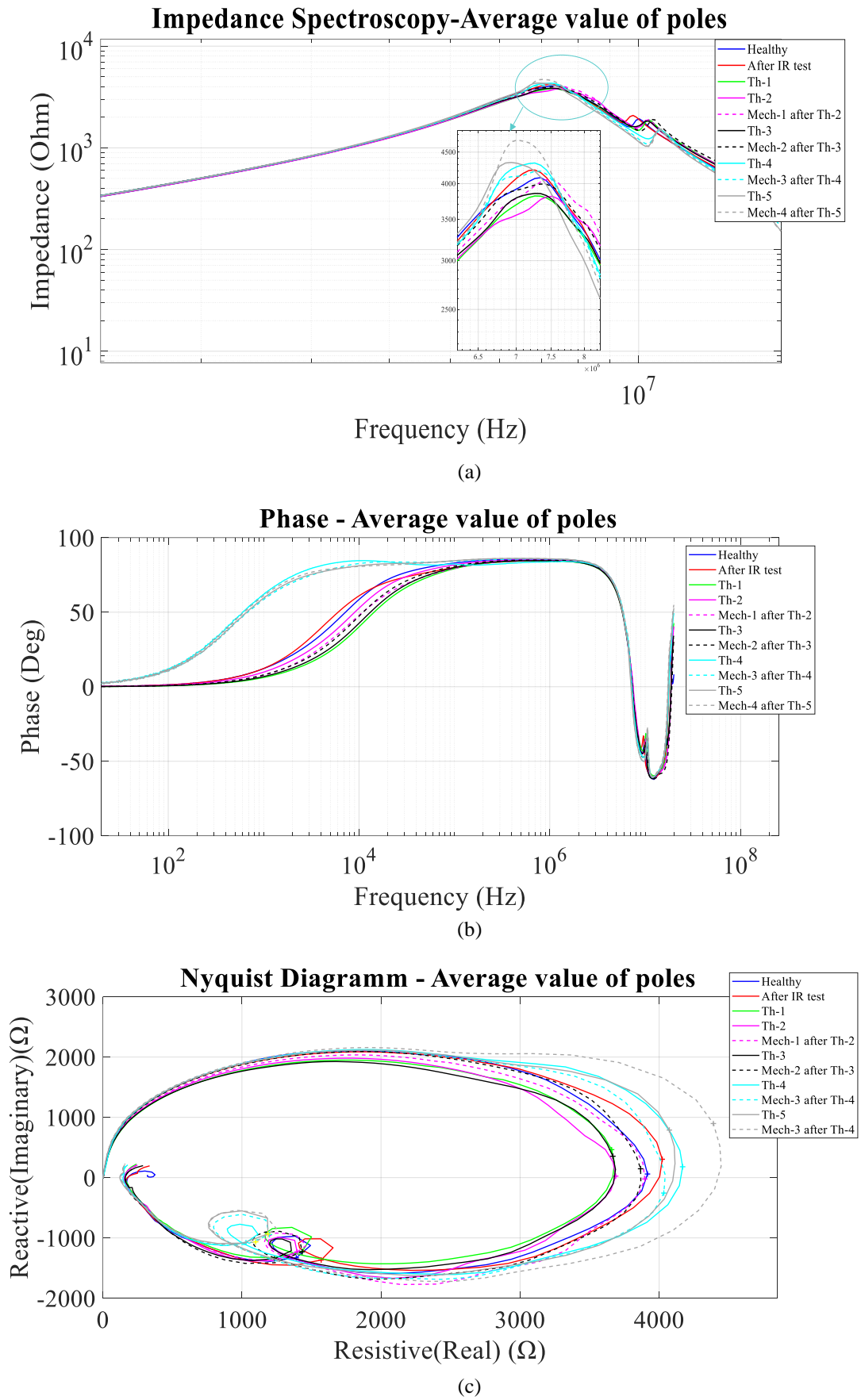
Fig.5.12: Comparative FRA results, where: (a) Impedance Spectroscopy, (b) Phase, (c) Nyquist Plot

In Fig.5.13 and Fig.5.14, as well as in Table 5.6 and Table 5.7, the displacements, magnitudes, angles, and both real and imaginary parts of the peak and resonance impedances are summarized. This coordination facilitates a more thorough analysis of the results.
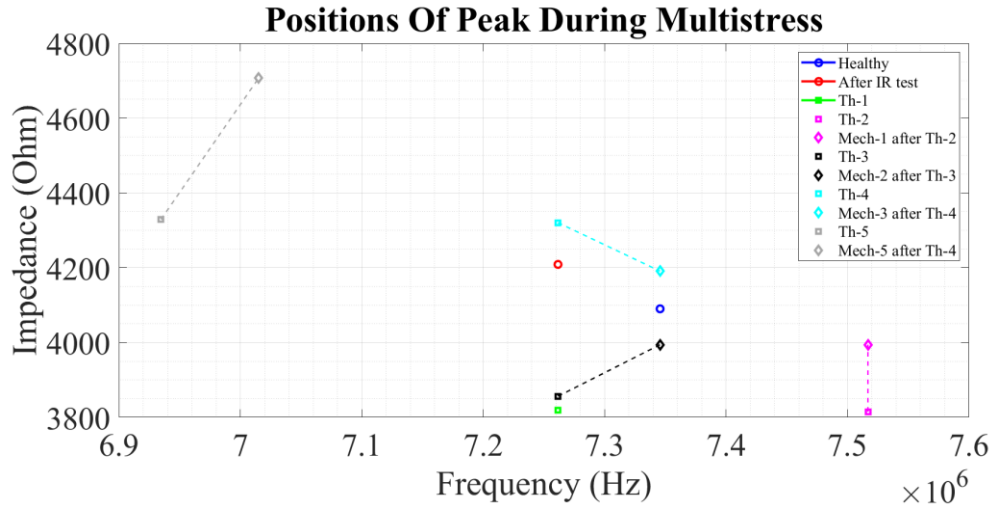

Fig.5.13: Low-Frequency Resonance (Peak) Positions

Cycle	Frequency (Hz)	$\lvert Z \rvert \angle \varphi$ (Ω)	Real (Ω)	Imag (Ω)
Healthy	7345650	4090.1∠ − 1.353°	3916.02	60.09
After IR	7261560	4208.77∠2.32°	4022.393	304.598
Th-1	7261560	3819.74∠5.692°	3658.376	464.045
Th-2	7516750	3814.78∠-1.554°	3687.512	24.987
Mech-1 after Th-2	7516747.5	4061.83∠-2.94°	3897.2	-22.404
Th-3	7261560	3856.329∠2.476°	3667.163	354.95
Mech-2 after Th-3	7345650	3994.28∠0.806°	3866.558	146.91
Th-4	7261560	4320.348∠0.537°	4168.864	180.083
Mech-3 after Th-4	7345650	4190.867∠-5.68°	4033.523	-255.897
Th-5	6934740	4329.16∠9.071°	4073.325	789.269
Mech-4 after Th-5	7015041.5	4706.713∠9.894°	4389.83	897.4759

Table 5.6: Low-Frequency Resonance(peak)

It is noted that the IR test displays analogous behaviour to the preceding experiment, manifesting an elevation in both resistance and capacitance. This leads to a rise in phase and a decline in capacitive behaviour. Subsequently, in the first thermal cycle, the amplitude decreases, and the Nyquist curve shrinks due to the decrease in resistance. In the second thermal cycle, the amplitude remains almost constant, while the Nyquist curve shifts downwards towards the capacitive region, indicating a decrease in capacitance due to the introduction of air, although the capacitive reaction also increases. However, there is a concurrent considerable decrease in resistance, so no significant changes are observed in the amplitude.

Following this, in the first mechanical cycle, the amplitude increases due to the increase in capacitive behaviour and a concurrent shift of the Nyquist plot towards the negative axis. This shift is caused by air ingress into the insulation resulting from thermal ageing, and mechanical vibration. Then, in the Th-3, the amplitude decreases, and the Nyquist curve shrinks after thermal stress due to the resistance decrease during thermal ageing. However, in Mech-2, the amplitude increases due to the decrease in capacitance.

Simultaneously, in these cycles, local delamination is highly likely, which becomes apparent in the fourth cycle, where the amplitude increases sharply, and the Nyquist curve significantly expands due to the additional resistance introduced by the air bubble in the insulation. Immediately after, in the third mechanical stress cycle, the amplitude decreases, and the Nyquist curve shrinks, despite the capacitive reactance increasing, as evidenced by the shift towards the negative axis. The decrease in amplitude in this case is attributed to a decrease in resistance due to PAI insulation detachment from copper caused by mechanical stress, and the creation of cracks in the insulation, as indicated by the split in the impedance peak.

Therefore, the fourth cycle (fourth thermal and third mechanical) represents a critical threshold, where permanent changes occur in insulation materials. These changes elucidate the behaviour of the pole in the fifth cycle (fifth thermal and fourth mechanical), with a rapid increase in amplitude and changes in the characteristics of the equivalent pole circuit like the rapid increase in phase.
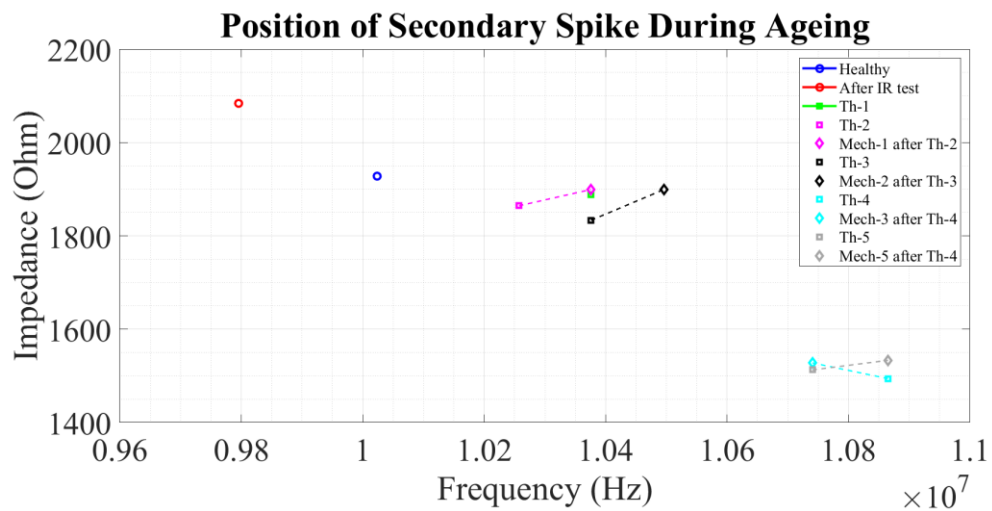

Fig.5.14: Spike Positions

Cycle	Frequency (Hz)	$|Z|∠φ$ (Ω)	Real (Ω)	Imag (Ω)
Healthy	10023700	1927.88∠-44.07°	1390.721	-1330.357
After IR	9795580	2083.88∠-41.28°	1569.832	-1366.355
Th-1	10376000	1888.55∠-40.85°	1432.275	-1226.35
Th-2	10257200	1864.44∠-41.58°	1396.572	-1231.11
Mech-1 after Th-2	10376008	1889.73∠-44.71°	1344.949	-1317.89
Th-3	10376000	1833.36∠-48.45°	1233.99	-1344.942
Mech-2 after Th-3	10496100	1899.34∠-40.68°	1433.209	-1230.33
Th-4	10865000	1494.08∠-46.34°	1029.012	-1078.038
Mech-3 after Th-4	10740600	1527.71∠-37.92°	1197.9	-942.78
Th-5	10740600	1512.73∠-38.22°	1187.11	-934.549
Mech-4 after Th-5	10865014	1533.28∠-44.04°	1098.87	-1066.27

Table 5.7: High-frequency resonance(spike)

Regarding the behaviour of the spike, it does not exhibit significant variations even after the IR test until the third cycle (third thermal and second mechanical). However, local delamination may exist, which becomes apparent from the fourth cycle where the spike amplitude notably decreases. This decrease could be attributed to the PAI insulation detachment from the copper due to delamination and vibration, along with potential insulation cracking. Since then, in all subsequent cycles, the amplitude remains consistently low.

Following is the graphical representation of the dissipation factor (Fig.5.15), utilized for the evaluation of multistress after each complete ageing cycle.
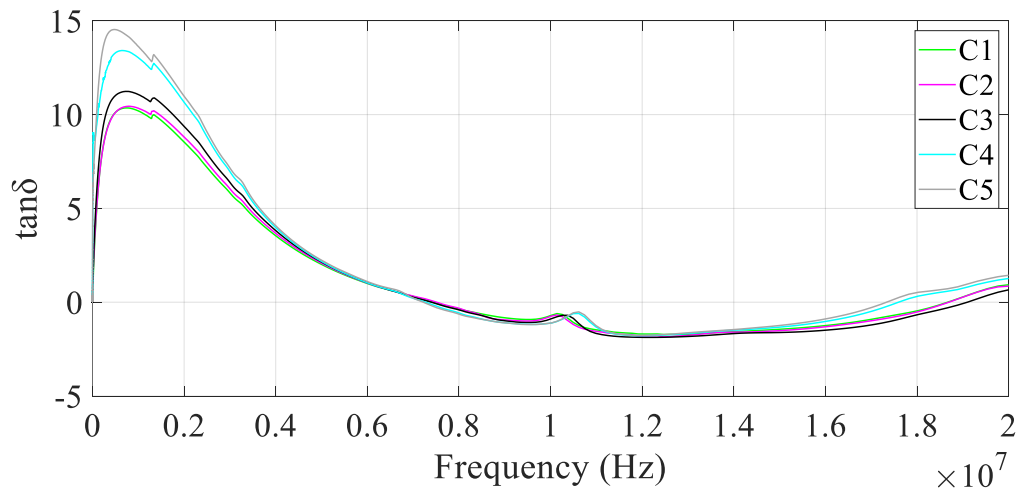

Fig.5.15: Dissipation Factor

In this case, the dissipation factor initially increases until reaching its peak, which correlates with the increase in polarization losses. Subsequently, as polarization

losses decrease, the dissipation factor also decreases. Moreover, it is observed in each cycle that the dissipation factor increases, indicating the presence of phenomena such as delamination and air-filled voids within the insulation. Additionally, during the fourth cycle, it is evident that the insulation characteristics have changed due to delamination and cracking, as the dissipation factor has increased significantly compared to the previous cycles, thus justifying the characterization of the critical threshold. Furthermore, it can be noted that the last two cycles are associated with higher losses, both near the peak frequency and at higher frequencies above 1.4MHz.

Following the aforementioned stressing procedures, the poles of these two groups underwent early voltage breakdown tests. A copper bar was positioned alongside each pole, ensuring full contact with all its turns. The high-voltage electrodes were connected to one terminal of the coil and the outer copper bar, thus establishing a high-voltage differential that imposed stress on the coil's insulation. Voltage was incrementally increased in a ramp-like fashion. Upon insulation breakdown, the instrument recorded the corresponding breakdown voltage.

To evaluate the Multistress procedure, breakdown tests were additionally performed on 6 healthy, unaged poles possessing similar characteristics. This was undertaken to compute their breakdown voltage and compare it with that of the aged poles. Consequently, histograms (Fig.5.16a) and normal distributions (Fig.5.16b) of both healthy and aged poles were generated for a detailed assessment of the results.

(a)
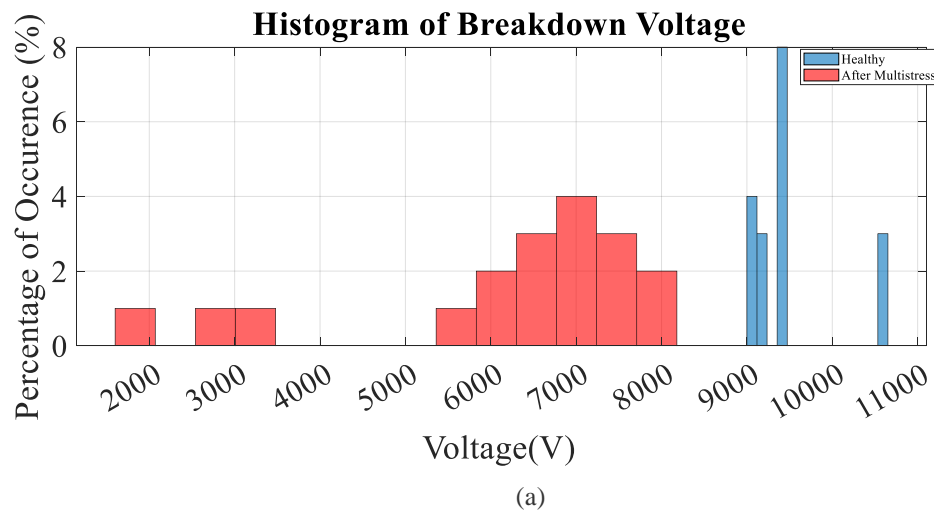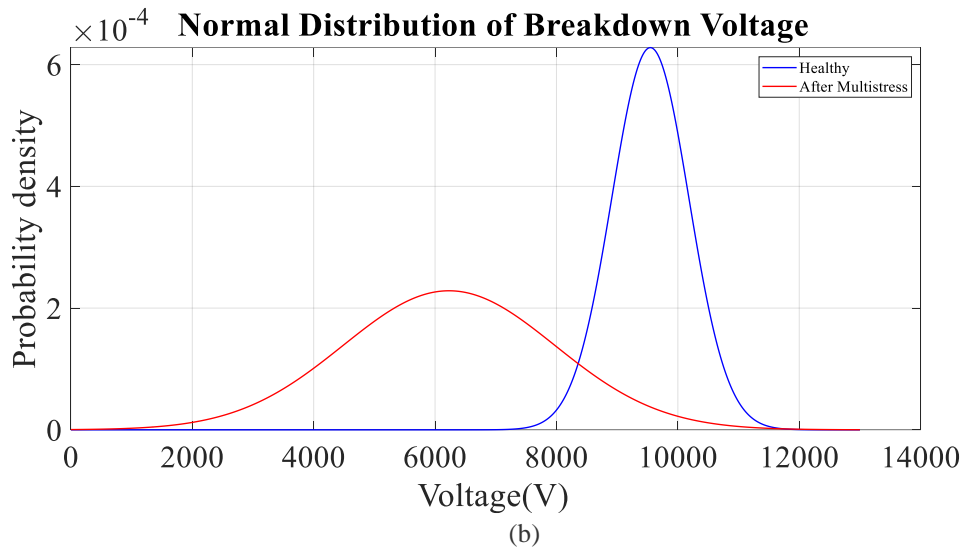
Fig.5.16: (a) Histogram and (b) normal distribution of the breakdown voltage of the poles that have been subjected to alternating thermal and mechanical stress cycles compared to the healthy samples.

Health Status	Average Value (V)	Standard Deviation (V)
Healthy	9546.6	635.28
After Multistress	6229.5	1746.26

Table 5.8: Normal Distribution Parameters

Throughout the multistress ageing process, a consistent decrease in breakdown voltage is observed, while the standard deviation tends to increase for aged samples. This rise in standard deviation is attributed to the utilization of more aged poles compared to unaged ones, along with the emergence of notably low breakdown voltages in some aged poles due to ageing. Nevertheless, these findings confirm the effectiveness of multistress accelerated ageing techniques. The trend of decreasing breakdown voltage is monotonic, as evidenced by the shift of the normal distribution of aged samples towards lower breakdown voltages. Additionally, the mean breakdown voltage of aged samples shows a significant reduction of 34.74% compared to unaged samples.

5.2.2 Thermal Cycling & Mechanical Stress

A group of 18 poles has initially undergone 8 cycles of thermal cycling stress. Thermal Cycling aims to simulate thermal changes in the insulating materials while the motor operates under varying loads, with minimal fluctuations. Subsequently, two cycles of mechanical stress will follow to assess the impact of mechanical stress after several thermal cycling cycles, particularly when delamination is most pronounced. The

analytical multistress procedure is illustrated in Fig.5.17. and the stressing temperatures and durations are detailed in Table 5.9.
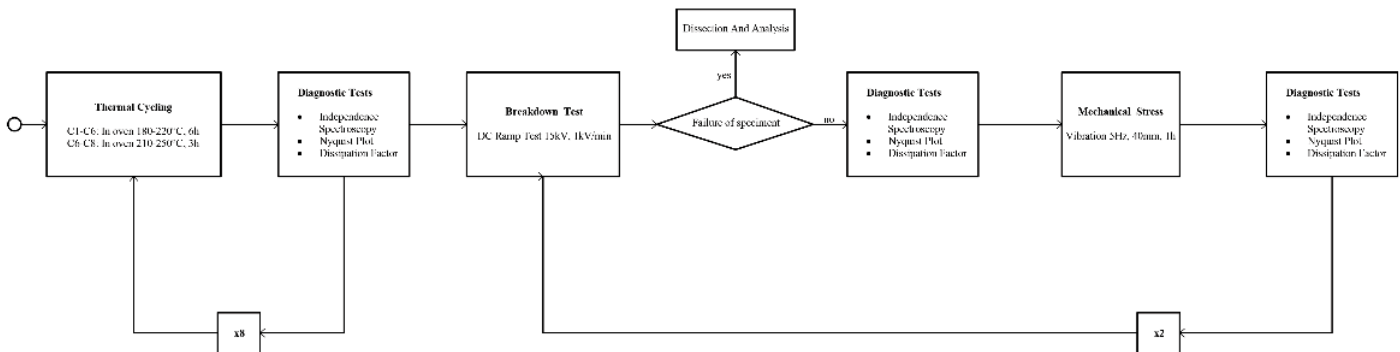
Fig.5.17: Test Procedure

Stress Type	Duration(hrs)	Stress Parameters
Thermal Cycling	6	180-220°C
Thermal Cycling	6	180-220°C
Thermal Cycling	6	180-220°C
Thermal Cycling	6	180-220°C
Thermal Cycling	6	180-220°C
Thermal Cycling	6	180-220°C
Thermal Cycling	3	210-250°C
Thermal Cycling	3	210-250°C
Mechanical	1	5Hz (motor)
Mechanical	1	5Hz (motor)

Table 5.9: Stress Parameters

Initially, the amplitude is presented in Fig.5.18a, the phase in Fig.5.18b, and the Nyquist diagram in Fig.5.18c exclusively for the thermal cycling to be evaluated separately as a distinct process.
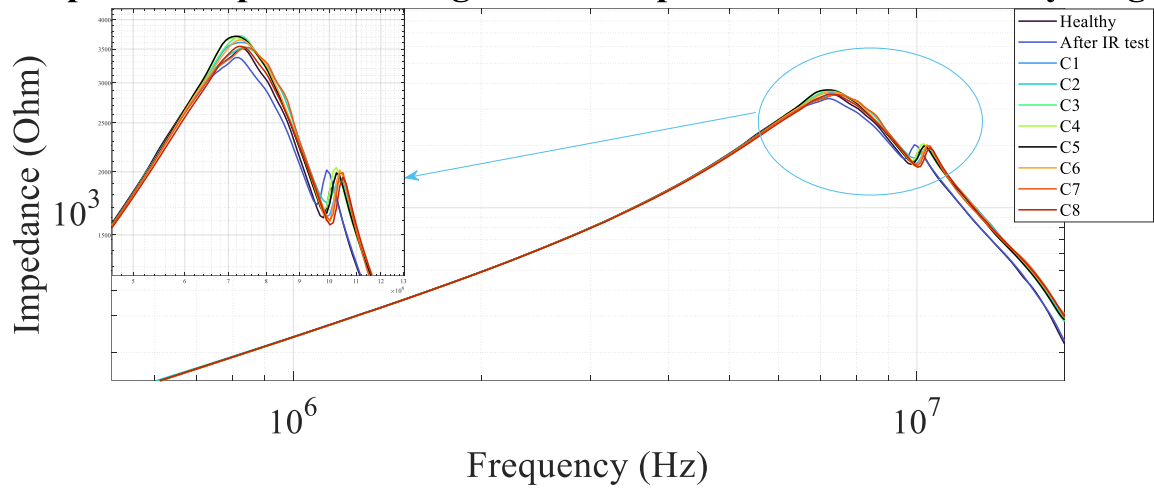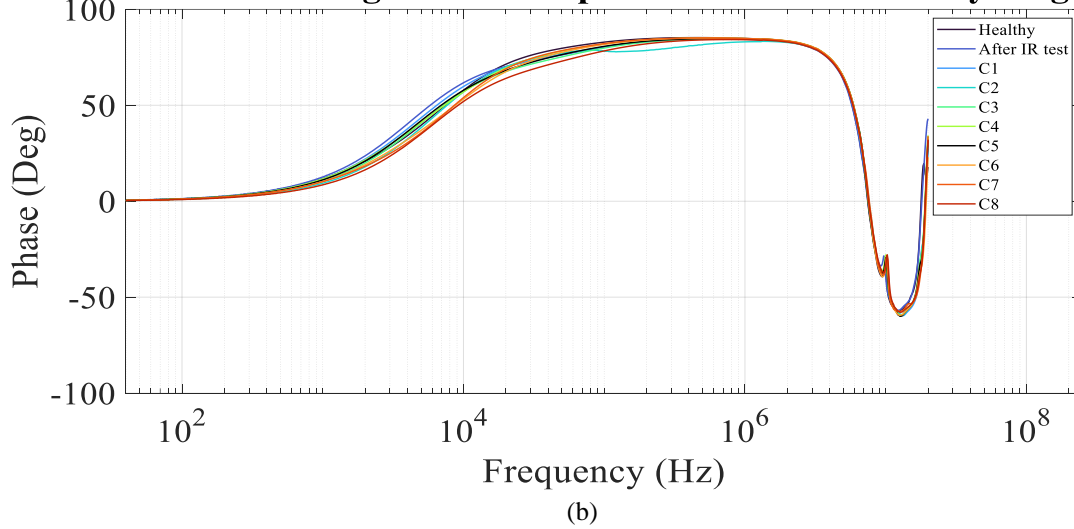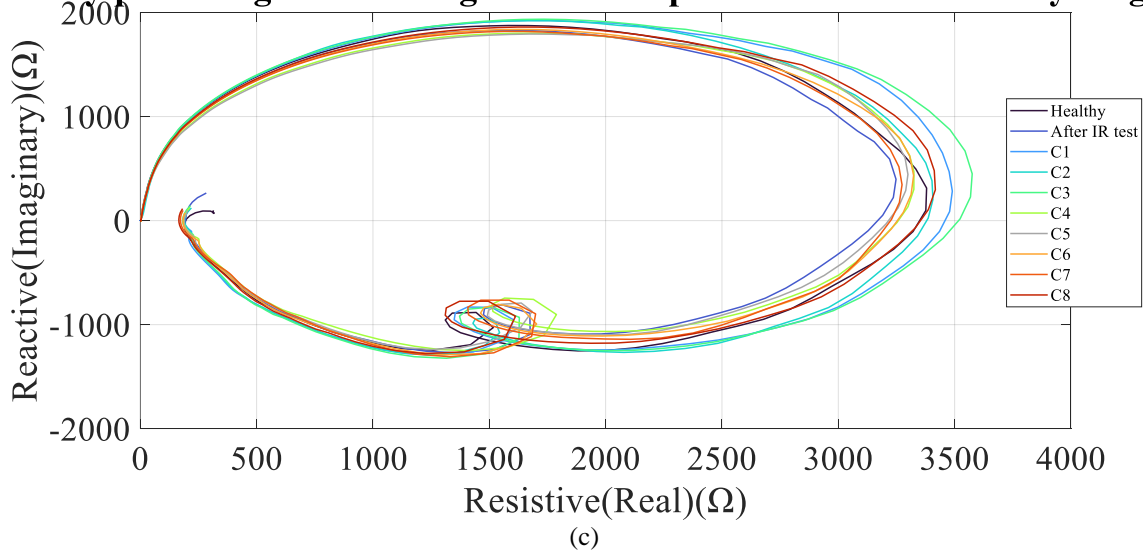
Fig.5.18: a) Impedance, b) Phase versus the frequency for the poles, and c) Nyquist plot, under various thermal cycling stress conditions

In Table 5.10 and Table 5.11, the magnitude, phase, real, and imaginary impedance values at the peak and spike are delineated, correspondingly.

Cycle	Frequency (Hz)	$|Z|\angle\varphi$ (Ω)	Real (Ω)	Imag (Ω)
Healthy	7345650	3513.56∠5.44°	3379.544	312.693
After IR	7178440	3366.57∠10.73°	3220.37	591.76
Th-1	7345650	3607.08∠7.93°	3476.42	470.1898
Th-2	7430710	3524.76∠6.62°	3402.717	382.5848
Th-3	7261560	3716.84∠11.04°	3544.799	668.8409
Th-4	7178440	3686.75∠12.69°	3504.26	764.5
Th-5	7178440	3710.52∠12.71°	3524.65	767.5399
Th-6	7345650	3647.58∠7.37°	3512.674	425.32
Th-7	7516748	3525.69∠4.7°	3414.476	275.32
Th-8	7261563	3542.72∠11.74°	3382.58	677.98

Table 5.10: Low-Frequency Resonance (Peak)

Following the IR test, the capacitance increases due to the absorption current. In the first thermal cycle (Th-1), the impedance rises because of the increased capacitive behaviour of the pole, evident from the decrease in angle and the extension and simultaneous downward shift of the Nyquist curve. The increase in capacitive behaviour is attributed to air ingress into the insulation due to Thermal Cycling. In Th-2, the amplitude decreases due to resistance reduction, while in the third cycle, the amplitude increases significantly, with no reduction in angle, indicating local delamination introducing an air bubble into the insulation, ultimately increasing resistance. From the fourth cycle onwards, the amplitude either decreases due to degradation or increases with extension and shifts towards the capacitive behaviour perspective of the Nyquist curve due to decreased capacitance caused by air ingress into the insulation. From the sixth cycle onwards, and particularly in the last two cycles (when accelerated ageing is performed), it is noteworthy that the Nyquist curve gradually expands, approaching the healthy condition.

Cycle	Frequency (Hz)	$|Z|\angle\varphi$ (Ω)	Real (Ω)	Imag (Ω)
Healthy	10139800	1868.17∠-41.03°	1418.81	-1193.13
After IR	9909010	2016.03∠-33.95°	1675.87	-1093.43
Th-1	10376000	1953.59∠-36.59°	1573	-1141.18
Th-2	10376000	1917.18∠-39.66°	1481.258	-1198.61
Th-3	10257200	1994.26∠-35.49°	1627.418	-1132.01
Th-4	10257200	2039.37∠-37.99°	1612.14	-1226.86
Th-5	10257200	1989.39∠-35.83°	1616.26	-1136.89
Th-6	10376008	2016.29∠-37.08°	1610.462	-1185.27
Th-7	10496148	1992.81∠-41.72°	1494.508	-1301.64
Th-8	10496148	1952.158∠-36.89°	1564.95	-1140.88

Table 5.11: High-Frequency Resonance (Spike)

In terms of the spike, overall, due to Thermal Cycling, a rightward shift and an increase in amplitude are observed compared to the healthy case, which is a consequence of the decrease in capacitance at the pole end-turns.

After Thermal Cycling has induced delamination and concurrently, there is a possibility that the windings may have loosened on the poles, consequently leading to higher vibration levels. For this reason, mechanical stress will be applied to assess its potential impact on the pole's health. Presented below are the impedance (Fig. 5.19a), phase (Fig. 5.19b), and Nyquist diagram (Fig. 5.19c) of the final thermal cycling cycle, as well as those of the 2 mechanical ageing cycles and breakdown test. The breakdown test is included in the FRA analysis as it significantly affects the pole's health.

(a)

(b)
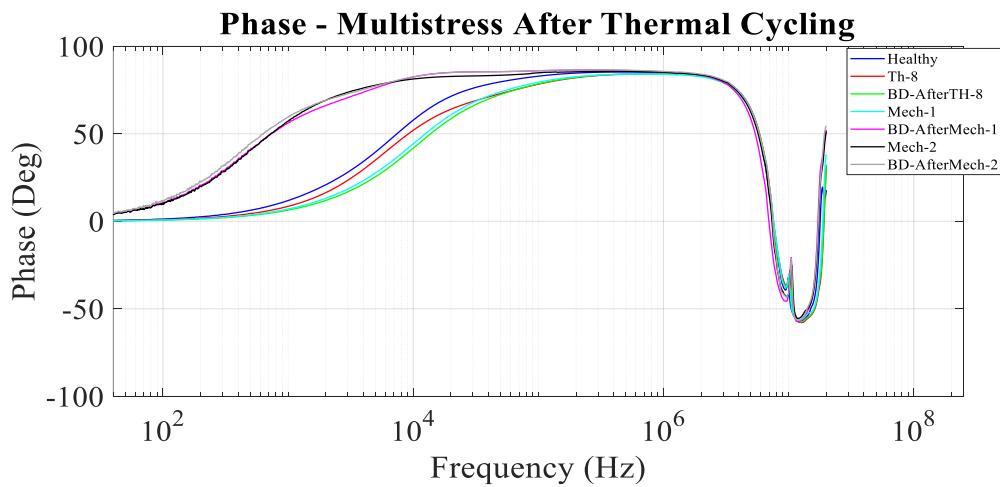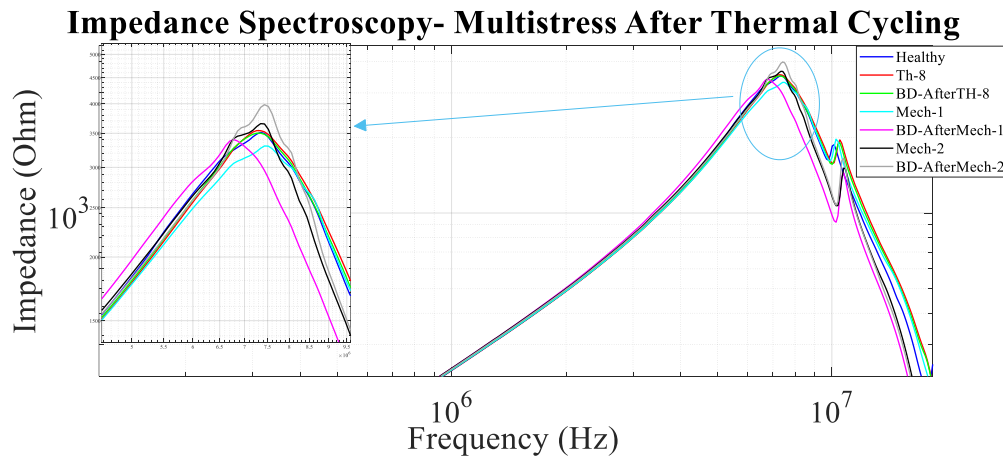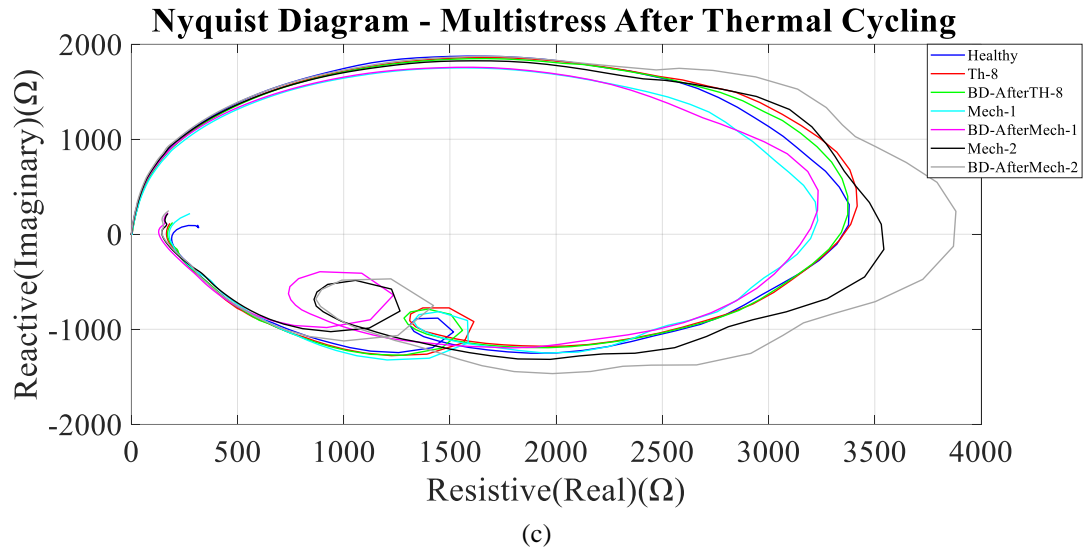
Fig.5.19: (a) Impedance, b) Phase versus the frequency for the poles, and (c) Nyquist plot, after various thermal cycling stress conditions

Cycle	Frequency (Hz)	$|Z|\angle\varphi$ (Ω)	Real (Ω)	Imag (Ω)
Healthy	7345650	3513.56∠5.44°	3379.5	312.69
Th-8	7261563	3542.72∠11.74°	3382.58	677.98
IR test after Th-8	7345650	3501.44∠6.66°	3372.763	398.5931
Mech-1	7430710	3304.93∠5.93°	3219.88	341.49
BD test after Mech-1	6776890	3401.406∠7.97°	3233.187	460.8843
Mech-2	7345650	3655.92∠0.58°	3530.59	104.8
BD test after Mech-2	7430710	3983.38∠2.58°	3881.84	241.421

Table 5.12: Low-Frequency Resonance (Peak)

After 8 cycles of thermal cycling, local delamination occurs. Following the IR test and during the first mechanical cycle, a significant decrease in impedance is observed, indicating that the PAI insulation may have completely detached from the copper due to delamination caused by thermal cycling and mechanical stress vibration. This leads to a dramatic reduction in resistance and amplitude, as well as a shrinkage of the Nyquist curve. Additionally, during the second mechanical cycle, a split in the peak is observed once again, indicating a probable crack in the insulation due to vibration and permanent changes in insulation materials. This is further confirmed in the subsequent breakdown test, where the pole characteristics have been altered, resulting in a rapid increase in amplitude.

Cycle	Frequency (Hz)	$|Z| \angle \varphi$ (Ω)	Real (Ω)	Imag (Ω)
Healthy	10139800	1868.16∠-41.03°	1418.81	-1193.13
Th-8	10496148	1952.158∠-36.89°	1564.95	-1140.88
IR test after Th-8	10496100	1902.53∠-40.02°	1460.1	-1199.1
Mech-1	10257200	1965.45∠-36.18°	1586.21	-1143.2
BD test after Mech-1	10740600	1445.62∠-39.01°	1125.48	-899.79
Mech-2	10740600	1508.01∠-32.68°	1265.24	-808.55
BD test after Mech-2	10740600	1650.42∠ − 40.57°	1254.28	-1065.88

Table 5.13: High-Frequency Resonance (Spike)

Observing the behaviour of spike following thermal cycling and the IR test, we note that there are no significant changes. However, local delamination exists due to thermal cycling, and it is highly probable that this, in combination with the initial mechanical stress, led to cracking of the insulation bonding. Therefore, in the subsequent breakdown test, it is highly likely that a puncture occurred in the insulation, resulting in an instantaneous drop in IR to zero, thereby causing an "infinite" current flow according to Ohm's law. This may explain the rapid drop in spike amplitude, which changes characteristics and remains at low amplitude levels.

In Fig.5.20, the dissipation factor resulting from the last thermal cycling cycle, as well as the two subsequent mechanical stress cycles, is presented to demonstrate the impact of multistress in the insulation system.
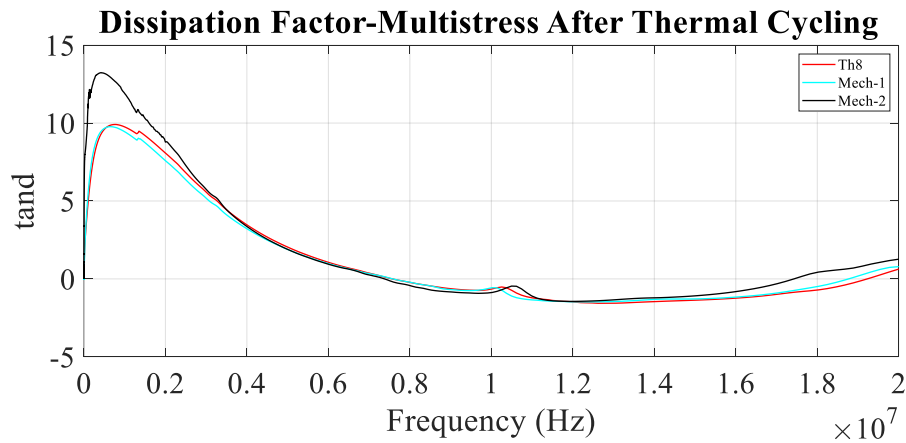
Fig.5.20: Multistress procedure after Thermal Cycling

Upon examination of the dissipation factor results, it becomes apparent that mechanical stress plays a pivotal role, particularly in the second cycle. This cycle exhibits a significant increase in the dissipation factor, primarily attributed to delamination induced by thermal cycling and insulation cracking resulting from mechanical stress induced by vibration and magnetically induced forces. These factors collectively contribute to insulation breakdown.

To conclude the evaluation of this ageing method, breakdown tests were conducted on all pole samples. It is noteworthy that during the breakdown test after Mechanical Cycle 1, one pole was experienced a catastrophic failure and subsequently excluded from the aforementioned FRA analysis measurements. Unfortunately, it is not possible to present images of this pole. However, the location of the fault suggests that its weakest point was the outer insulation of the coil.

As mentioned in the breakdown test of Section 5.2.1 the test applied to 6 unaged healthy poles for comparison. Then a group of poles was tested after finishing 8 thermal ageing cycles, followed by two mechanical stressing cycles (three breakdown voltage measurements in total). The resulting histogram is presented in Fig.5.21. The normal and Weibull distributions have been computed through Eq.5.3 and Eq.5.2 accordingly and shown in Fig.5.22 and Fig 5.23. The two distributions do not vary significantly; however, a more monotonic behaviour is observed in the normal distribution. The averages and standard deviations are shown in Table 5.14, while the parameters a, and b of Weibull Distribution are detailed in Table 5.15. It is clear that the mechanical vibrations have a strong effect on the integrity of the insulation. Although the average breakdown voltage does not change significantly (1% and 3.5% drops after each mechanical stress cycle concerning the condition after the thermal cycling), the standard deviation gets an impact (64% and 146% increase after each mechanical stress cycle concerning the condition after the thermal cycling). Such a shift in standard deviation is attributed to the emergence of very low breakdown voltage values).
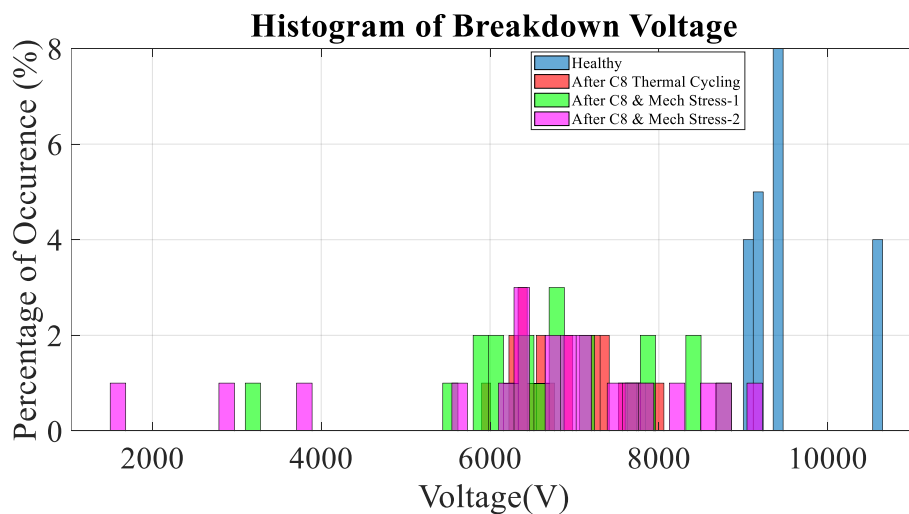
Fig.5.21. Comparative Histograms for all Stages of Multistress
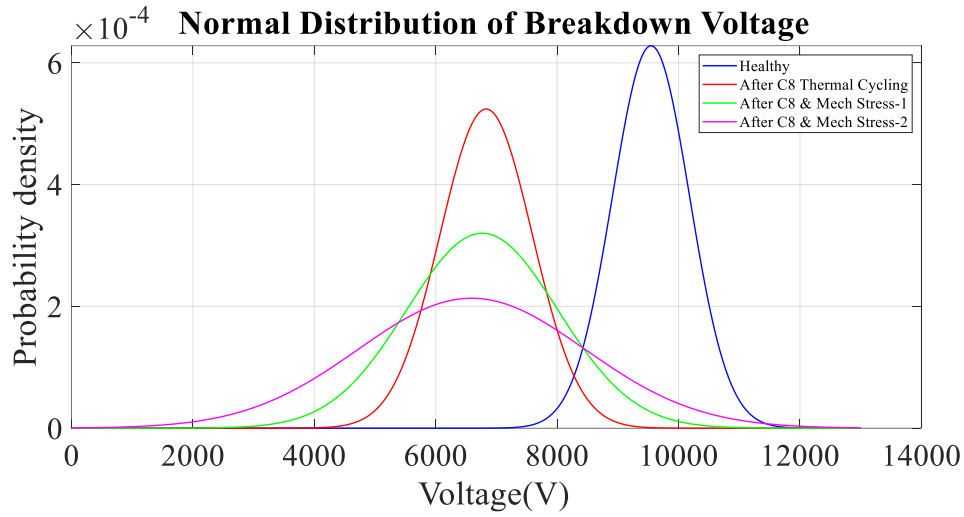
Fig.5.22: Comparative Analysis of Normal Distributions Across All Stages of Multistress

Health Status	Average Value (V)	Standard Deviation (V)
Healthy	9546.6	635.28
After Th-8	6830.28	761.14
After Mech-1	6766.52	1246.26
After Mech-2	6590.81	1869.71

Table.5.14: Normal Distribution Parameters
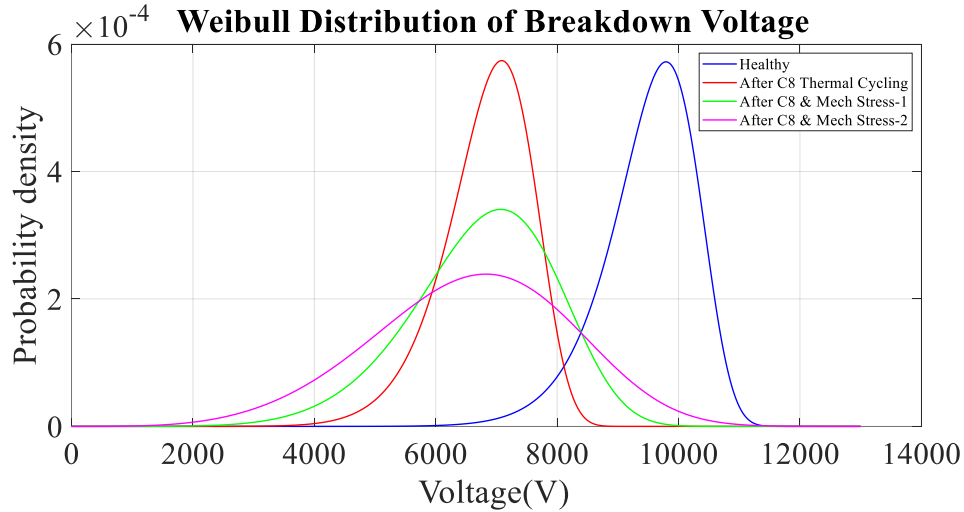
Fig.5.23. Comparative Analysis of Weibull Distributions Across All Stages of Multistress

Health Status	a	b
Healthy	9837.26	15.2625
After Th-8	7146.78	11.1037
After Mech-1	7247.42	6.62709
After Mech-2	7206.82	4.55923

Table 5.15: Weibull Distribution Parameters

An interesting observation would also be to note how the breakdown voltage of each pole is affected in each ageing cycle. The pole that failed during mechanical aging cycle 1 was excluded from the calculations since it was not reused in the second mechanical aging cycle.
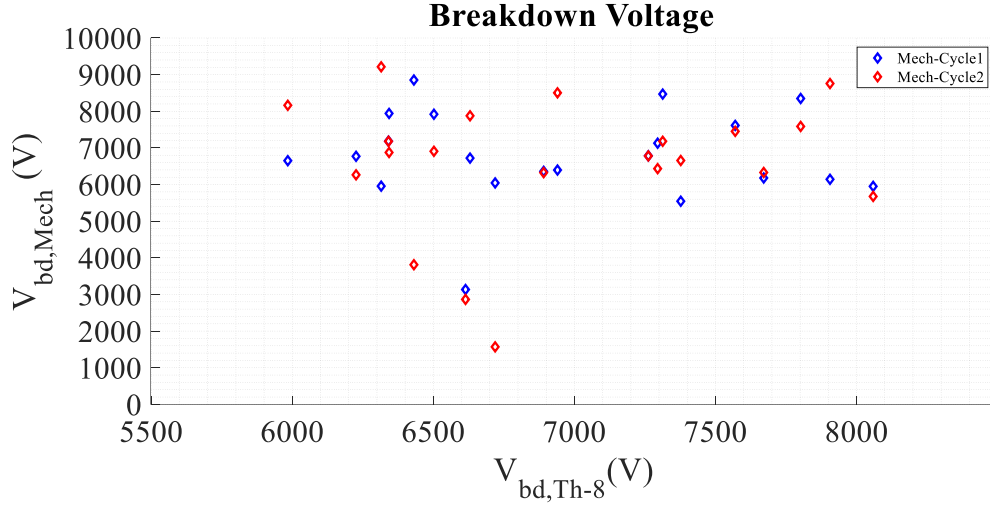
Fig.5.24. Scatter Plot Analysis of Breakdown Voltage Across Multistress Cycles

Examining the findings depicted in Fig.5.24, it becomes evident that in Mech-2, there is a 66.7% reduction in the breakdown voltage of the poles compared to Mech-1. Moreover, between TH-8 and Mech-1, the breakdown voltage of Mech-1 experiences a decrease of 51.38%, while between Mech-2 and TH-8, Mech-2 exhibits a reduction of 60% in breakdown voltage relative to TH-8.

5.3 Discussion and Conclusions

This master thesis has led to the following outcomes:

• The equivalent pole model offers the opportunity to establish a library that holds significant value for both prognosis and diagnosis. Concerning prognosis, with reference to the existing literature, predictions can be made regarding the alterations in dielectric characteristics of the pole. Regarding diagnosis, the utilization of Impedance Spectroscopy and Nyquist diagram allows for the continuous identification of the specific element within the equivalent circuit accountable for deviations in resistance and capacitance compared to the healthy state.

- Nyquist plots can be very useful to identify overall changes in the impedance spectra, because they combine the impedance and phase versus the frequency pieces of information.

- The effect of the IR test is not negligible and leads to an increase in the angle, attributable to the fact that the absorption current confounds the capacitance.

- Although Impedance Spectroscopy on its own may not be that reliable when degradation is involved, in combination with the Nyquist Diagram, it can provide exceptional diagnostic information regarding which parameters are affected in each aging cycle. As verified by experimental results, the impedance and ellipse of the Nyquist diagram of aged samples may, in some cases, closely resemble those of healthy samples. However, the breakdown test and dissipation factor reveal that the insulation has degraded significantly.

- The Thermal Cycling behaviour of the impedance spectra and the Nyquist plots is not monotonic with the accelerated ageing procedure. The amplitude either increases or decreases after each cycle, however the Nyquist ellipsis progressively shrinks back to the original size. This complex behaviour is attributed to the chemical composition changes of the different, co-existing insulating materials (epoxy and PAI insulation). Their respective electrical parameters have opposite effects on the total impedance. On one hand, the resistance of the insulation will drop with ageing leading to a reduction of the impedance. On the other hand, the ageing will reduce the capacitance as well, leading to an increase of the capacitive reactance and consequently the increase of the impedance.

- The mechanical stress is capable of weakening the material severely, after thermal stress is already applied. This is attributed to early delamination effects inside the coil.

- The mechanical stress tends to increase the size of the Nyquist ellipsis after thermal stress. This is a clear consequence of delamination effects caused by the drop in the insulation capacitance and consequently the increase of the capacitive reactance. At the same time, the high voltage testing has revealed that it becomes easier to break the insulation. Although, the average breakdown voltage of the material does not change after the thermally degraded insulation withstands consecutive mechanical

stress cycles, however the mechanical stress causes weak spots in the insulation causing it to break early (in this case with significantly lower voltage).

- After a series of aging cycles, the results from impedance spectroscopy and Nyquist diagram indicate that the insulation has reached a critical threshold. At this point, local delamination has significantly intensified due to combined thermal and mechanical stresses. This is evident from the increase in impedance and the expansion of the Nyquist diagram attributed to the rise in resistance caused by the introduction of air bubbles into the insulation. However, subsequent mechanical stress will ultimately prove decisive, as weak spots in the insulation will lead to insulation cracks and detachment of the PAI insulation from the copper. The insulation crack has been successfully diagnosed through impedance spectroscopy, with a noticeable split in the low-frequency resonance (peak). The detachment of the PAI insulation can be detected by the sudden drop in resistance. Finally, beyond the critical threshold, the characteristics of the poles undergo significant changes, with a substantial increase in both resistance and phase angle.

- The poles under examination exhibit a second peak (high-frequency resonance spike). This has been proven to hold exceptional diagnostic significance for the health of the pole, as in all aging methods conducted, at the point characterized as the critical threshold, there was a dramatic decrease in the amplitude without significant alteration in subsequent ageing cycles. This clearly indicates phenomena of delamination, insulation cracks, and detachment of the PAI insulation from the copper windings.

- The dissipation factor serves as an exceptional diagnostic tool for evaluating the multistress procedure. Initially, it increases until it reaches a maximum value due to the simultaneous presence of polarization and conductance losses. Subsequently, at higher frequencies, it decreases due to the decline in polarization losses. Among the cycles, the dissipation factor increases as a result of delamination and can also indicate the critical threshold, where the tanδ value significantly increases due to delamination and cracking.

- In the experiment involving alternating thermal-mechanical stress, it is evident that the normal distribution has shifted to the left, with a significant decrease in the mean value and an increase in the standard deviation. The latter is due to the fact that

some poles have been significantly deteriorated with reduced breakdown voltage, thereby increasing the standard distribution.

- In the experiment applying mechanical stress after thermal cycling, it is observed that thermal cycling reduces the required breakdown voltage of the material as expected. However, the standard deviation of the sample distribution remains similar to that of the healthy cases. Conversely, electromechanical stress does not significantly affect the average value but strongly impacts the standard deviation due to the sudden reduction in breakdown voltage of some poles. These poles have developed weak spots in the insulation system, leading to potential crack formations.

- So far, it can be concluded that early faults may be due to adjacent poles and not inter-turn short circuits. The only broken pole has such a failure and this agrees with the only early fault specimen that pole has salvaged.

5.4   Recommendations and Future work

- Development of a more complex model that takes into consideration each turn's individual complex inductance between the turn and the core. This model will reveal location-dependent fault information more accurately and could be used for more detailed degradation analysis.

- A series of degradation studies should be done with adjacent poles in order to investigate the turn-to-turn short circuit mechanism.

- Creation of a neural network that takes as input the results from impedance spectroscopy (magnitude and phase), and is trained to understand which parameters have changed based on certain patterns derived from the current work and literature. It will then adjust the corresponding parameters in the model, so that through impedance spectroscopy and the resulting Nyquist diagram, it simulates the ageing status of the pole's insulation.

Bibliography

[1] Osman, Ahmed I., et al. "Cost, environmental impact, and resilience of renewable energy under a changing climate: a review." Environmental Chemistry Letters 21.2 (2023): 741-764.

[2] Rahman, Abidur, Omar Farrok, and Md Mejbaul Haque. "Environmental impact of renewable energy source based electrical power plants: Solar, wind, hydroelectric, biomass, geothermal, tidal, ocean, and osmotic." Renewable and Sustainable Energy Reviews 161 (2022): 112279.

[3] Ivanova, G.; Moreira, A.C. Antecedents of Electric Vehicle Purchase Intention from the Consumer's Perspective: A Systematic Literature Review. Sustainability 2023, 15, 2878. https://doi.org/10.3390/su15042878.

[4] P. S. Kumari and M. P. Lalitha, "Analysis and Review of Various Motors Used for Electric Vehicle Propulsion," *2023 International Conference on Smart Systems for applications in Electrical Sciences (ICSSES)*, Tumakuru, India, 2023, pp. 1-5, doi: 10.1109/ICSSES58299.2023.10200965.

[5] I. Bolvashenkov, J. Kammermann and H. -G. Herzog, "Methodology for selecting electric traction motors and its application to vehicle propulsion systems," *2016 International Symposium on Power Electronics, Electrical Drives, Automation and Motion (SPEEDAM)*, Capri, Italy, 2016, pp. 1214-1219, doi: 10.1109/SPEEDAM.2016.7525853.

[6] Z. Cao, A. Mahmoudi, S. Kahourzade and W. L. Soong, "An Overview of Electric Motors for Electric Vehicles," *2021 31st Australasian Universities Power Engineering Conference (AUPEC)*, Perth, Australia, 2021, pp. 1-6, doi: 10.1109/AUPEC52110.2021.9597739.

[7] M. Ehsani, K. V. Singh, H. O. Bansal and R. T. Mehrjardi, "State of the Art and Trends in Electric and Hybrid Electric Vehicles," in *Proceedings of the IEEE*, vol. 109, no. 6, pp. 967-984, June 2021, doi: 10.1109/JPROC.2021.3072788.

[8] Liwei Song, Daqian Jiang, Shumei Cui and Shan Sheng, "Reluctance torque analysis and reactance calculation of IPM for HEVs based on FEM," *2010*

IEEE Vehicle Power and Propulsion Conference, Lille, France, 2010, pp. 1-4, doi: 10.1109/VPPC.2010.5729146.

[9] Y. Tang, J. J. H. Paulides, I. J. M. Besselink, F. Gardner and E. A. Lomonova, "Indirect drive in-wheel system for HEV/EV traction," *2013 World Electric Vehicle Symposium and Exhibition (EVS27)*, Barcelona, Spain, 2013, pp. 1-9, doi: 10.1109/EVS.2013.6915011.

[10] L. Shao, R. Navaratne, M. Popescu and G. Liu, "Design and Construction of Axial-Flux Permanent Magnet Motors for Electric Propulsion Applications—A Review," in *IEEE Access*, vol. 9, pp. 158998-159017, 2021, doi: 10.1109/ACCESS.2021.3131000.

[11] L. Jia, M. Lin, W. Le and A. Yang, "Design and Analysis of Axial-Flux Modular Interior Permanent Magnet Machines with Yokeless and Segmented Armature," *2022 IEEE 20th Biennial Conference on Electromagnetic Field Computation (CEFC)*, Denver, CO, USA, 2022, pp. 1-2, doi: 10.1109/CEFC55061.2022.9940836.

[12] N. Taran, G. Heins, V. Rallabandi, D. Patterson and D. M. Ionel, "Systematic Comparison of Two Axial Flux PM Machine Topologies: Yokeless and Segmented Armature versus Single Sided," *2019 IEEE Energy Conversion Congress and Exposition (ECCE)*, Baltimore, MD, USA, 2019, pp. 4477-4482, doi: 10.1109/ECCE.2019.8913104.

[13] W. Xu, J. Zhu, Y. Guo, S. Wang, Y. Wang and Z. Shi, "Survey on electrical machines in electrical vehicles," *2009 International Conference on Applied Superconductivity and Electromagnetic Devices*, Chengdu, China, 2009, pp. 167-170, doi: 10.1109/ASEMD.2009.5306667.

[14] Z. Q. Zhu and C. C. Chan, "Electrical machine topologies and technologies for electric, hybrid, and fuel cell vehicles," 2008 IEEE Vehicle Power and Propulsion Conference, Harbin, China, 2008, pp. 1-6, doi: 10.1109/VPPC.2008.4677738.

[15] S. J. Rind, Y. Ren, Y. Hu, J. Wang and L. Jiang, "Configurations and control of traction motors for electric vehicles: A review," in *Chinese Journal of Electrical Engineering*, vol. 3, no. 3, pp. 1-17, December 2017, doi: 10.23919/CJEE.2017.8250419.

[16]   https://blog.orientalmotor.com/technical-manual-series-brushless-motor-structure-and-principles

[17]   https://www.motioncontroltips.com/bldc-motor-marketing-jargon/

[18]   https://traxial.com/uncategorized/axial-flux-motor-vs-radial-flux-motor-a-focus-on-magnetic-field-orientation/

[19]   A. Mahmoudi, N. A. Rahim and W. Hew, "TORUS and AFIR axial-flux permanent-magnet machines: A comparison via finite element analysis", *Int. Rev. Model. Simulations*, vol. 4, no. 2, pp. 624-631, Apr. 2011.

[20]   Electrical Insulation for Rotating Machines: Design, Evaluation, Aging, Testing, and Repair, Second Edition. Greg C. Stone, Ian Culbert, Edward A. Boulter, and Hussein Dhirani. © 2014 John Wiley & Sons, Inc. Published 2014 by John Wiley & Sons, Inc.

[21]   T. Munih and D. Miljavec, "A method for accelerated ageing of electric machine insulation," Proceedings of the 16th International Conference on Mechatronics - Mechatronika 2014, Brno, Czech Republic, 2014, pp. 65-70, doi: 10.1109/MECHATRONIKA.2014.7018237.

[22]   C. Han, "Lifetime evaluation of class E electrical insulation for small induction motors," in IEEE Electrical Insulation Magazine, vol. 27, no. 3, pp. 14-19, May-June 2011, doi: 10.1109/MEI.2011.5871364.

[23]   P. Cygan and J. R. Laghari, "Models for insulation aging under electrical and thermal multistress," in IEEE Transactions on Electrical Insulation, vol. 25, no. 5, pp. 923-934, Oct. 1990, doi: 10.1109/14.59867.

[24]   G. C. Stone, B. K. Gupta, J. F. Lyles and H. G. Sedding, "Experience with accelerated aging tests on stator bars and coils," IEEE International Symposium on Electrical Insulation, Toronto, ON, Canada, 1990, pp. 356-360, doi: 10.1109/ELINSL.1990.109772.

[25]   Persson, E., "Transient effects in application of PWM inverters to induction motors," Pulp and Paper Industry Technical Conference, 1991., Conference Record of 1991 Annual, vol., no., pp.228,233, 3-7 June 1991

[26]   Stone, G.; Campbell, S.; Tetreault, S., "Inverter-fed drives: which motor stators are at risk?," Industry Applications Magazine, IEEE , vol.6, no.5, pp.17,22, Sep/Oct 2000

[27]   S. Choi et al., "Fault Diagnosis Techniques for Permanent Magnet AC Machine and Drives—A Review of Current State of the Art," in IEEE Transactions on Transportation Electrification, vol. 4, no. 2, pp. 444-463, June 2018, doi: 10.1109/TTE.2018.2819627.

[28]   Y. Duan and H. Toliyat, "A review of condition monitoring and fault diagnosis for permanent magnet machines," 2012 IEEE Power and Energy Society General Meeting, San Diego, CA, USA, 2012, pp. 1-4, doi: 10.1109/PESGM.2012.6345545.

[29]   T. Orlowska-Kowalska et al., "Fault Diagnosis and Fault-Tolerant Control of PMSM Drives–State of the Art and Future Challenges," in IEEE Access, vol. 10, pp. 59979-60024, 2022, doi: 10.1109/ACCESS.2022.3180153.

[30]   P. Zhou, D. Lin, Y. Xiao, N. Lambert and M. A. Rahman, "Temperature-Dependent Demagnetization Model of Permanent Magnets for Finite Element Analysis," in IEEE Transactions on Magnetics, vol. 48, no. 2, pp. 1031-1034, Feb. 2012, doi: 10.1109/TMAG.2011.2172395.

[31]   M. Cheng, J. Hang and J. Zhang, "Overview of fault diagnosis theory and method for permanent magnet machine," in Chinese Journal of Electrical Engineering, vol. 1, no. 1, pp. 21-36, Dec. 2015, doi: 10.23919/CJEE.2015.7933135.

[32]   Pietrzak P, Wolkiewicz M. Comparison of Selected Methods for the Stator Winding Condition Monitoring of a PMSM Using the Stator Phase Currents. Energies. 2021; 14(6):1630. https://doi.org/10.3390/en14061630

[33]   W. Qiao and D. Lu, "A Survey on Wind Turbine Condition Monitoring and Fault Diagnosis—Part I: Components and Subsystems," in *IEEE Transactions on Industrial Electronics*, vol. 62, no. 10, pp. 6536-6545, Oct. 2015, doi: 10.1109/TIE.2015.2422112.

[34]   S. Nandi, H. A. Toliyat and X. Li, "Condition Monitoring and Fault Diagnosis of Electrical Motors—A Review," in IEEE Transactions on Energy Conversion, vol. 20, no. 4, pp. 719-729, Dec. 2005, doi: 10.1109/TEC.2005.847955.

[35]   A. Bellini, F. Filippetti, C. Tassoni and G. -A. Capolino, "Advances in Diagnostic Techniques for Induction Machines," in *IEEE Transactions on Industrial Electronics*, vol. 55, no. 12, pp. 4109-4126, Dec. 2008, doi: 10.1109/TIE.2008.2007527.

[36]   J. CusidÓCusido, L. Romeral, J. A. Ortega, J. A. Rosero and A. GarcÍaGarcia Espinosa, "Fault Detection in Induction Machines Using Power Spectral Density in Wavelet Decomposition," in *IEEE Transactions on Industrial Electronics*, vol. 55, no. 2, pp. 633-643, Feb. 2008, doi: 10.1109/TIE.2007.911960

[37]   Ding, S., Hang, J., Li, H., & Wang, Q. (2017). Demagnetisation fault detection in PMSM using zero sequence current components. *Electronics Letters*, *53*(3), 148-150.

[38]   J. Faiz and H. Nejadi-Koti, "Demagnetization Fault Indexes in Permanent Magnet Synchronous Motors—An Overview," in IEEE Transactions on Magnetics, vol. 52, no. 4, pp. 1-11, April 2016, Art no. 8201511, doi: 10.1109/TMAG.2015.2480379.

[39]   D. G. Dorrell, M. -F. Hsieh and Y. Guo, "Unbalanced Magnet Pull in Large Brushless Rare-Earth Permanent Magnet Motors With Rotor Eccentricity," in IEEE Transactions on Magnetics, vol. 45, no. 10, pp. 4586-4589, Oct. 2009, doi: 10.1109/TMAG.2009.2022338

[40]   A. Rezig, A. N'Diaye, M. R. Mekideche and A. Djerdir, "Modelling and detection of bearing faults in Permanent Magnet Synchronous Motors," *2012 XXth International Conference on Electrical Machines*, Marseille, France, 2012, pp. 1778-1782, doi: 10.1109/ICElMach.2012.6350122.

[41]   V. Gurusamy, K. H. Baruti, M. Zafarani, W. Lee and B. Akin, "Effect of Magnets Asymmetry on Stray Magnetic Flux Based Bearing Damage

Detection in PMSM," in IEEE Access, vol. 9, pp. 68849-68860, 2021, doi: 10.1109/ACCESS.2021.3076779

[42]   K. Ahsanullah, E. Jeyasankar, A. N. Vignesh, S. K. Panda, R. Shanmukha and S. Nadarajan, "Eccentricity fault analysis in PMSM based marine propulsion motors," *2017 20th International Conference on Electrical Machines and Systems (ICEMS)*, Sydney, NSW, Australia, 2017, pp. 1-6, doi: 10.1109/ICEMS.2017.8056162.

[43]   M. Zafarani, E. Bostanci, Y. Qi, T. Goktas and B. Akin, "Interturn Short-Circuit Faults in Permanent Magnet Synchronous Machines: An Extended Review and Comprehensive Analysis," in IEEE Journal of Emerging and Selected Topics in Power Electronics, vol. 6, no. 4, pp. 2173-2191, Dec. 2018, doi: 10.1109/JESTPE.2018.2811538.

[44]   Pietrzak, P.; Wolkiewicz, M. On-line Detection and Classification of PMSM Stator Winding Faults Based on Stator Current Symmetrical Components Analysis and the KNN Algorithm. *Electronics* **2021**, *10*, 1786. https://doi.org/10.3390/electronics10151786

[45]   H. Jeong, S. Moon, J. Lee and S. W. Kim, "Inter-turn short fault diagnosis of permanent magnet synchronous machines using negative sequence components," 2016 IEEE International Conference on Industrial Technology (ICIT), Taipei, Taiwan, 2016, pp. 170-174, doi: 10.1109/ICIT.2016.7474745.

[46]   J. -C. Urresty, J. -R. Riba, H. Saavedra and L. Romeral, "Detection of inter-turns short circuits in permanent magnet synchronous motors operating under transient conditions by means of the zero sequence voltage," Proceedings of the 2011 14th European Conference on Power Electronics and Applications, Birmingham, UK, 2011, pp. 1-9.

[47]   Y. Da, X. Shi and M. Krishnamurthy, "Health monitoring, fault diagnosis and failure prognosis techniques for Brushless Permanent Magnet Machines," 2011 IEEE Vehicle Power and Propulsion Conference, Chicago, IL, USA, 2011, pp. 1-7, doi: 10.1109/VPPC.2011.6043248.

[48]   S. J. Engel, B. J. Gilmartin, K. Bongort and A. Hess, "Prognostics, the real issues involved with predicting life remaining," 2000 IEEE Aerospace

Conference. Proceedings (Cat. No.00TH8484), Big Sky, MT, USA, 2000, pp. 457-469 vol.6, doi: 10.1109/AERO.2000.877920.

[49]   D. F. Kavanagh, D. A. Howey and M. D. McCulloch, "An applied laboratory characterisation approach for electric machine insulation," *2013 9th IEEE International Symposium on Diagnostics for Electric Machines, Power Electronics and Drives (SDEMPED)*, Valencia, Spain, 2013, pp. 391-395, doi: 10.1109/DEMPED.2013.6645745.

[50]   B. Groschup, M. Nell, F. Pauli and K. Hameyer, "Characteristic Thermal Parameters in Electric Motors: Comparison Between Induction- and Permanent Magnet Excited Machine," in *IEEE Transactions on Energy Conversion*, vol. 36, no. 3, pp. 2239-2248, Sept. 2021, doi: 10.1109/TEC.2021.3056771

[51]   B. Petitgas *et al*., "High temperature aging of enameled copper wire — Relationships between chemical structure and electrical behavior," *2011 Annual Report Conference on Electrical Insulation and Dielectric Phenomena*, Cancun, Mexico, 2011, pp. 84-88, doi: 10.1109/CEIDP.2011.6232602.

[52]   R. Wrobel, S. J. Williamson, J. D. Booker and P. H. Mellor, "Characterizing the in situ Thermal Behavior of Selected Electrical Machine Insulation and Impregnation Materials," in *IEEE Transactions on Industry Applications*, vol. 52, no. 6, pp. 4678-4687, Nov.-Dec. 2016, doi: 10.1109/TIA.2016.2589219.

[53]   R. Wrobel, S. J. Williamson, J. D. Booker and P. H. Mellor, "Characterising the performance of selected electrical machine insulation systems," *2015 IEEE Energy Conversion Congress and Exposition (ECCE)*, Montreal, QC, Canada, 2015, pp. 4857-4864, doi: 10.1109/ECCE.2015.7310345.

[54]   D. F. Kavanagh, K. N. Gyftakis and M. D. McCulloch, "Early-onset Degradation of Thin-film Magnet Wire Insulation for Electromechanical Energy Converters," *2019 IEEE 12th International Symposium on Diagnostics for Electrical Machines, Power Electronics and Drives (SDEMPED)*, Toulouse, France, 2019, pp. 37-43, doi: 10.1109/DEMPED.2019.8864916.

[55]   R. Hemmati, F. Wu and A. El-Refaie, "Survey of Insulation Systems in Electrical Machines," *2019 IEEE International Electric Machines & Drives Conference (IEMDC)*, San Diego, CA, USA, 2019, pp. 2069-2076, doi: 10.1109/IEMDC.2019.8785099.

[56]   IEEE 43-2014, "IEEE Recommended Practice for Testing Insulation Resistance of Rotating Machinery"

[57]   S. Grubic, R. G. Harley, T. G. Habetler and J. Restrepo, "Sensitivity analysis of the surge test applied to AC machines," 2011 IEEE International Electric Machines & Drives Conference (IEMDC), Niagara Falls, ON, Canada, 2011, pp. 618-623, doi: 10.1109/IEMDC.2011.5994881.

[58]   Armando Souza Guedes, Sidelmo Magalhães Silva, Brazde Jesus Cardoso Filho, Cláudio Alvares Conceição, "Evaluation of electrical insulation in three-phase induction motors and classification of failures using neural networks" , Electric Power Systems Research,Vol.140,pp.263-273,2016.

[59]   "IEEE Recommended Practice for Insulation Testing of AC Electric Machinery (2300 V and Above) With High Direct Voltage," in *IEEE Std 95-2002 (Revision of IEEE Std 95-1977)* , vol., no., pp.1-56, 12 April 2002, doi: 10.1109/IEEESTD.2002.93574.

[60]   L. Rux and S. Grzybowski, "Evaluation of delaminated high-voltage rotating machine stator winding groundwall insulation," Conference Record of the 2000 IEEE International Symposium on Electrical Insulation (Cat. No.00CH37075), Anaheim, CA, USA, 2000, pp. 520-523, doi: 10.1109/ELINSL.2000.845562.

[61]   P. Zhang, P. Neti and K. Younsi, "Online Monitoring of Capacitance and Dissipation Factor of Motor Stator Winding Insulation During Accelerated Life Testing," *2018 IEEE Energy Conversion Congress and Exposition (ECCE)*, Portland, OR, USA, 2018, pp. 3267-3271, doi: 10.1109/ECCE.2018.8558036.

[62]   M. K. W. Stranges, S. Ul Haq and A. O. Vouk, "Monitoring Stator Insulation in Critical Motors: Choosing Diagnostic Tests," in IEEE Industry Applications Magazine, vol. 20, no. 1, pp. 50-55, Jan.-Feb. 2014, doi: 10.1109/MIAS.2013.2282566.

[63]   https://en.wikipedia.org/wiki/Schering_bridge

[64]   G. C. Stone, "Partial discharge diagnostics and electrical equipment insulation condition assessment," in IEEE Transactions on Dielectrics and Electrical Insulation, vol. 12, no. 5, pp. 891-904, Oct. 2005, doi: 10.1109/TDEI.2005.1522184.

[65]   P. A. Panagiotou, E. J. W. Stone, J. Mühlthaler, A. Reeh, A. Lambourne and G. W. Jewell, "Thermal Degradation Profile of Concentrated Stator Winding Insulation by Impedance Spectroscopy," 2023 IEEE 14th International Symposium on Diagnostics for Electrical Machines, Power Electronics and Drives (SDEMPED), Chania, Greece, 2023, pp. 554-560, doi: 10.1109/SDEMPED54949.2023.10271468.

[66]   F. Perisse, P. Werynski and D. Roger, "A New Method for AC Machine Turn Insulation Diagnostic Based on High Frequency Resonances," in IEEE Transactions on Dielectrics and Electrical Insulation, vol. 14, no. 5, pp. 1308-1315, October 2007, doi: 10.1109/TDEI.2007.4339494.

[67]   P. Neti and S. Grubic, "Online broadband insulation spectroscopy of induction machines using signal injection," 2014 IEEE Energy Conversion Congress and Exposition (ECCE), Pittsburgh, PA, USA, 2014, pp. 630-637, doi: 10.1109/ECCE.2014.6953454.

[68]   P. A. Panagiotou, A. Lambourne and G. W. Jewell, "Ex-situ Inspection of Concentrated Stator Coils by Means of Impedance Spectroscopy," *2022 International Conference on Electrical Machines (ICEM)*, Valencia, Spain, 2022, pp. 2331-2337, doi: 10.1109/ICEM51905.2022.9910588.

[69]   M. M. A. Salama and R. Bartnikas, "Determination of neural-network topology for partial discharge pulse pattern recognition," in IEEE Transactions on Neural Networks, vol. 13, no. 2, pp. 446-456, March 2002, doi: 10.1109/72.991430.

[70]   M. M. A. Salama and R. Bartnikas, "Fuzzy logic applied to PD pattern classification," in IEEE Transactions on Dielectrics and Electrical Insulation, vol. 7, no. 1, pp. 118-123, Feb. 2000, doi: 10.1109/94.839349.

[71]   M. Farahani, E. Gockenbach, H. Borsi, K. Schäfer and M. Kaufhold, "Behavior of machine insulation systems subjected to accelerated thermal aging test," in *IEEE Transactions on Dielectrics and Electrical Insulation*, vol. 17, no. 5, pp. 1364-1372, October 2010, doi: 10.1109/TDEI.2010.5595537

[72]   Pawel Piotr Pietrzak. Development of tests and methods of analysis for multi-factor ageing, degradation monitoring and/or lifetime modelling of an electrical insulation system of electrical motors (used in electric vehicle). Electric power. Institut National Polytechnique de Toulouse - INPT, 2023. English. ffNNT : 2023INPT0082ff.

[73]   'IEC 60034-18-31:2012 Rotating electrical machines - Part 18-31: Functional evaluation of insulation systems - Test procedures for form-wound windings Thermal evaluation and classification of insulation systems used in rotating machines'. 2012.

[74]   Ji, Y.; Giangrande, P.; Madonna, V.; Zhao, W.; Galea, M. Reliability-Oriented Design of Inverter-Fed Low-Voltage Electrical Machines: Potential Solutions. Energies 2021, 14, 4144. https://doi.org/10.3390/en14144144

[75]   A. Cimino, C. Staubach and F. Jenau, "Analysis of Accelerated Multi-Factor Aging Tests on the Winding Insulation System of Generator Stator Bars Used in Large Rotating Machines," *2018 IEEE Electrical Insulation Conference (EIC)*, San Antonio, TX, USA, 2018, pp. 110-113, doi: 10.1109/EIC.2018.8481029.

[76]   A. Cimino, C. Staubach and F. Jenau, "Ageing behaviour of the insulation system used in rotating machines," *2017 INSUCON - 13th International Electrical Insulation Conference (INSUCON)*, Birmingham, UK, 2017, pp. 1-6, doi: 10.23919/INSUCON.2017.8097184.

[77]   Q. Liu *et al.*, "Evaluation Method of Stator Insulation for Direct-drive Wind Turbine Generator Based on Accelerated Multi-factor Aging," *2019 IEEE Conference on Electrical Insulation and Dielectric Phenomena (CEIDP)*, Richland, WA, USA, 2019, pp. 138-141, doi: 10.1109/CEIDP47102.2019.9009904.

[78]   A. Cimino, F. Jenau and J. Horst, "Statistical Assessment of Lifetime Data of Multi-Factor Aged Generator Bars," *2019 54th International*

Universities Power Engineering Conference (UPEC), Bucharest, Romania, 2019, pp. 1-5, doi: 10.1109/UPEC.2019.8893560.

[79]   C. Shaver, M. Rumbaugh and S. Cain, "Accelerated thermal life testing for random-wound, polyimide wrapped medium voltage machines," *2014 IEEE Electrical Insulation Conference (EIC)*, Philadelphia, PA, USA, 2014, pp. 353-358, doi: 10.1109/EIC.2014.6869408.

[80]   R. Bartnikas and R. Morin, "Multi-stress aging of stator bars with electrical, thermal, and mechanical stresses as simultaneous acceleration factors," in *IEEE Transactions on Energy Conversion*, vol. 19, no. 4, pp. 702-714, Dec. 2004, doi: 10.1109/TEC.2004.832060.

[81]   R. Morin, R. Bartnikas and P. Menard, "A three-phase multi-stress accelerated electrical aging test facility for stator bars," in *IEEE Transactions on Energy Conversion*, vol. 15, no. 2, pp. 149-156, June 2000, doi: 10.1109/60.866992.

[82]   W. Chen and G. Gao, "Using multi-stress aging test to evaluate and improve medium-voltage stator insulation for adjustable speed drive applications," *2011 Record of Conference Papers Industry Applications Society 58th Annual IEEE Petroleum and Chemical Industry Conference (PCIC)*, Toronto, ON, Canada, 2011, pp. 1-7, doi: 10.1109/PCICon.2011.6085877.

[83]   R. Bartnikas and R. Morin, "Analysis of multistress-accelerated aged stator bars using a three-phase test arrangement," in *IEEE Transactions on Energy Conversion*, vol. 21, no. 1, pp. 162-170, March 2006, doi: 10.1109/TEC.2006.870047.

[84]   R. Brütsch, M. Tari, K. Fröhlich, T. Weiers and R. Vogelsang, "Insulation Failure Mechanisms of Power Generators [Feature Article]," in IEEE Electrical Insulation Magazine, vol. 24, no. 4, pp. 17-25, July-Aug. 2008, doi: 10.1109/MEI.2008.4581636

[85]   B. Singh, F. Mauseth, E. Eberg and E. Kantar, "Analysis of Partial Discharge Activity for Multi-Stress Accelerated Aged Stator Bars," *2023 IEEE Electrical Insulation Conference (EIC)*, Quebec City, QC, Canada, 2023, pp. 1-4, doi: 10.1109/EIC55835.2023.10177329.

[86]   Z. Jia, X. Peng, Z. Guan, L. Wang and B. Yue, "Evaluation of the Degradation of Generator Stator Ground Wall Insulation Under Multistresses Aging," in *IEEE Transactions on Energy Conversion*, vol. 23, no. 2, pp. 474-483, June 2008, doi: 10.1109/TEC.2008.918653.

[87]   Y. Nyanteh, L. Graber, C. Edrington, S. Srivastava and D. Cartes, "Overview of simulation models for partial discharge and electrical treeing to determine feasibility for estimation of remaining life of machine insulation systems," 2011 Electrical Insulation Conference (EIC).

[88]   Bo Yue, Xiaolin Chen, Yonghong Cheng, Jiancheng Song and Hengkun Xie, "Diagnosis of stator winding insulation of large generator based on partial discharge measurement," in *IEEE Transactions on Energy Conversion*, vol. 21, no. 2, pp. 387-395, June 2006, doi: 10.1109/TEC.2006.874223.

[89]   F. Guastavino, A. Ratto, E. Torello and G. Biondi, "Aging Tests on Nanostructured Enamels for Winding Wire Insulation," in *IEEE Transactions on Industrial Electronics*, vol. 61, no. 10, pp. 5550-5557, Oct. 2014, doi: 10.1109/TIE.2014.2301736.

[90]   F. Guastavino, A. Ratto, S. Squarcia and E. Torello, "Electro-thermal aging tests on different kinds of enamelled wires," 2010 10th IEEE International Conference on Solid Dielectrics, Potsdam, Germany, 2010, pp. 1-4, doi: 10.1109/ICSD.2010.5568020.

[91]   S. Grzybowski, E. A. Feilat and P. Knight, "Accelerated aging tests on magnet wires under high frequency pulsating voltage and high temperature," 1999 Annual Report Conference on Electrical Insulation and Dielectric Phenomena (Cat. No.99CH36319), Austin, TX, USA, 1999, pp. 555-558 vol.2, doi: 10.1109/CEIDP.1999.807866.

[92]   G. Lv, D. Zeng and T. Zhou, "Analysis of Secondary Losses and Efficiency in Linear Induction Motors With Composite Secondary Based on Space Harmonic Method," *IEEE Trans. Ener. Conv.*, vol. 32, no. 4, pp. 1583-1591, Dec. 2017.

[93]   Y. Feng, B. Shao, X. Tang, Y. Han, T. Wu and Y. Suzuki, "Improved Capacitance Model Involving Fringing Effects for Electret-Based Rotational

Energy Harvesting Devices," *IEEE Trans. Electr. Dev.*, vol. 65, no. 4, pp. 1597-1603, April 2018.

[94]   Al-Karmi, A. M. (2006). Impedance spectroscopy of gamma irradiated PM-355.   *Radiation   Measurements*,   *41*(2),   209-212. https://doi.org/10.1016/j.radmeas.2005.07.023

[95]   A. Mugarra, C. A. Platero, J. A. Martínez and U. Albizuri-Txurrka, "Large Salient Pole Synchronous Machines Field Windings Diagnosis by Frequency Response," *2018 XIII International Conference on Electrical Machines (ICEM)*, Alexandroupoli, Greece, 2018, pp. 1875-1880, doi: 10.1109/ICELMACH.2018.8506815.

[96]   M. Farahani, H. Borsi and E. Gockenbach, "Dielectric response studies on insulating system of high voltage rotating machines," in *IEEE Transactions on Dielectrics and Electrical Insulation*, vol. 13, no. 2, pp. 383-393, April 2006, doi: 10.1109/TDEI.2006.1624283.

[97]   Farahani, Mohsen, Hossein Borsi, and Ernst Gockenbach. "Study of capacitance and dissipation factor tip-up to evaluate the condition of insulating systems for high voltage rotating machines." *Electrical Engineering* 89 (2007): 263-270.

[98]   C. Hao and B. Gao, "Study on the frequency domain dielectric spectroscopy of rotating machines insulation," *2016 IEEE International Conference on High Voltage Engineering and Application (ICHVE)*, Chengdu, China, 2016, pp. 1-4, doi: 10.1109/ICHVE.2016.7800599.

Appendices

<div align="center">

Appendix A

Equipment Details

</div>

In this section, the measurement equipment utilized in the experimental procedure is included.

Fig6.1: Impedance Spectroscopy Set-Up

Fig6.2: Megohmmeter15kV Insulation Tester

Fig.6.3: Portable Megger Device

Fig.6.4: Digital Tachometer

Appendix B

Experimental Measurements

The experimental procedures involving the use of the equipment presented in Appendix A will be discussed in this section of the report.

- Impedance Spectroscopy:

Firstly, the most important setup has been the impedance spectroscopy. A table was devoted solely to the installation of the relevant equipment. The electrodes are normally screwed on the power transformer terminals. In this project, the electrodes have been screwed on the table at two fixed positions and at a 51 long distance between them to cancel any parasitic phenomena. The, two smaller wires have been connected to the electrodes while at their other end they carry crocodile clips. The pole under test is placed in the middle between the electrodes. A laptop is also connected to the instrument and controls the firing of the measurement and stores the results. The setup is shown in Fig.6.1.

When the capacitance between coil and core is to be measured, the coil is placed inside a 3D printed box. The box has a conducting bottom, where the pole sits thus having a galvanic connection, and it is offering an electrode outside the box. Therefore, the two terminals of the impedance analyser are connected to the conductor in contact with the pole and one of the winding's terminals. This setup is shown in Fig.6.5.
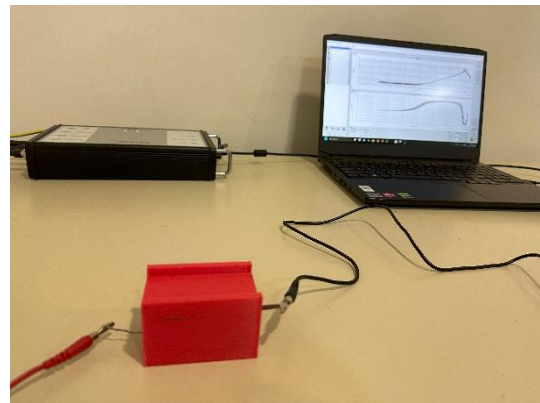
(a)   (b)

Fig.6.5: (a)box with conducting bottom, (b)the pole inside the casing
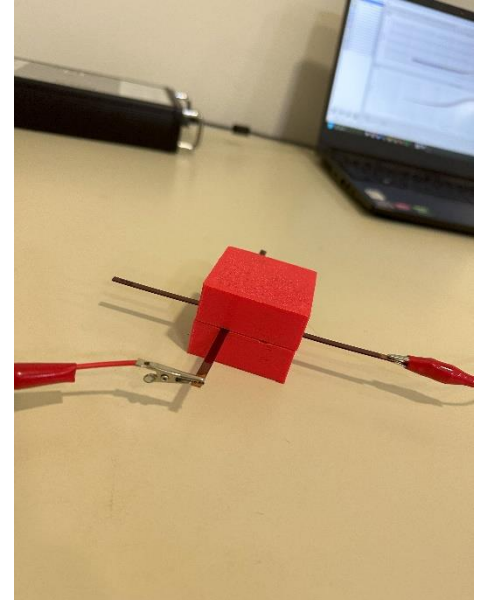
In order to measure the turn-to-turn capacitance and resistance, a different casing was built via 3D printing. It consists of two parallel racks that fit the copper bars. When placed perpendicular to each other, the two parts allow the crossing of two copper bars, thus offering their interconnection for dielectric testing. The setup is shown in Fig. 6.6.
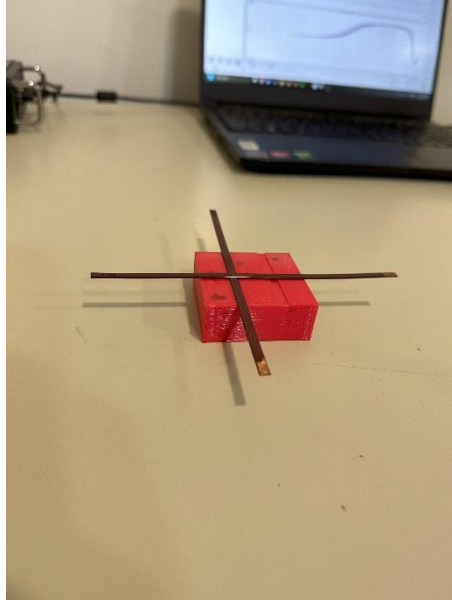
| (a) | (b) | (c) |

Fig. 6.6. a) The two parts of the casing, b) placing the copper bas and c) shielding the couple and connecting the electrodes.

- Megohmmeter 15kV:

For the measurement of coil-to-core resistance, a 15kV Megohmmeter (Fig. 6.2) was utilized in IR test mode. The connection configuration is depicted in Fig.6.7, where it is evident that one terminal of the Megohmmeter is connected to the top terminal of the pole, and the other terminal of the Megohmmeter to the bottom electrode of the casing, facilitating the application of high voltage between the coil and core for measuring the coil-to-pole insulation resistance.

Fig.6.7: Setup for measuring the coil-to-pole insulation resistance.

The measurement of the turn-to-turn insulation resistance was measured with the setup shown in Fig. 6.8. Due to high resistance value restrictions, two bars were tested simultaneously. The bars were placed in the two parallel ducts of the casing. A thin copper plate was placed on both of them and its end was outside the casing. Furthermore, the ends of the bars on one side are shorted. The Megohmmeter electrodes are applying a voltage at the copper plate and the shorted turns of the bars. The measurement is the equivalent surface resistance of the two bars (parallel connection).

Fig. 6.8. Setup for the measurement of the turn-to-turn insulation resistance.

In order to measure the Breakdown Voltage within the framework of DC Hipot Test, a Megohmmeter was utilized in Ramp Mode with a step of 1kV/min. For the execution of the test, the windings of the pole were in contact with an uninsulated copper bar, where one terminal of the measuring device was connected to one end of the pole, and the other terminal was connected to the bar where the pole was positioned. The voltage increases until reaching a point where the insulation is on the verge of breakdown, and the meter records the corresponding breakdown voltage.

- Portable Megger Device

The portable megger device (Fig. 6.3) was utilized to measure the internal DC resistance of the pole, with one end of the probe connected to the top end of the pole and the other end of the probe connected to the bottom end of the pole.

Appendix C
Mechanical Stress

Finally, the mechanical stressing device works as follows. Six poles are first placed in the moving wagon. The poles are placed between two still plates that are screwed in order to trap the poles. Then the electrical connections are made and the poles are connected in series. The wagon is then placed inside the C-core (Fig. 6.9) and screwed. The final assembly before operation is shown in Fig.6.10. Then the motor (Fig.6.11) is turned on via the inverter (Fig.6.12).
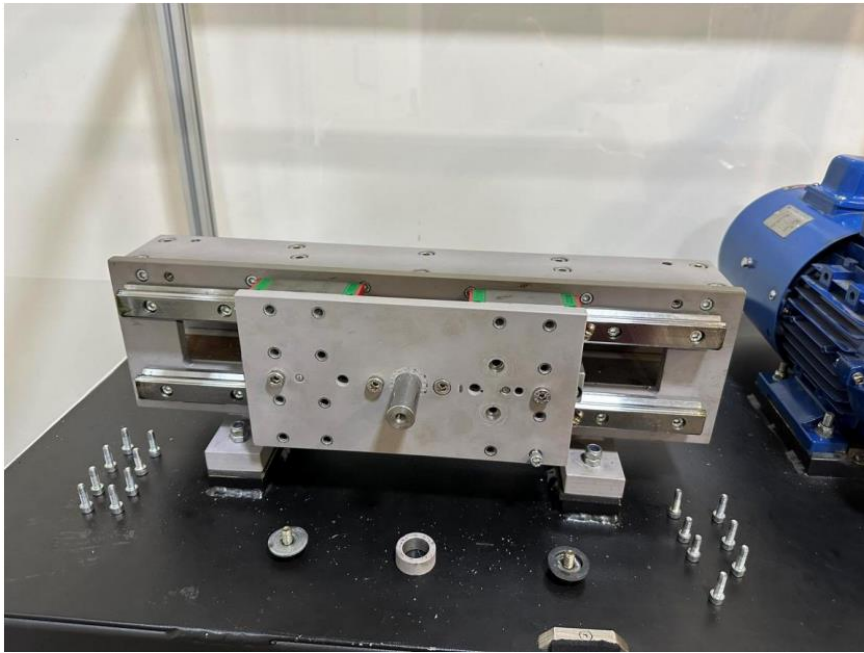
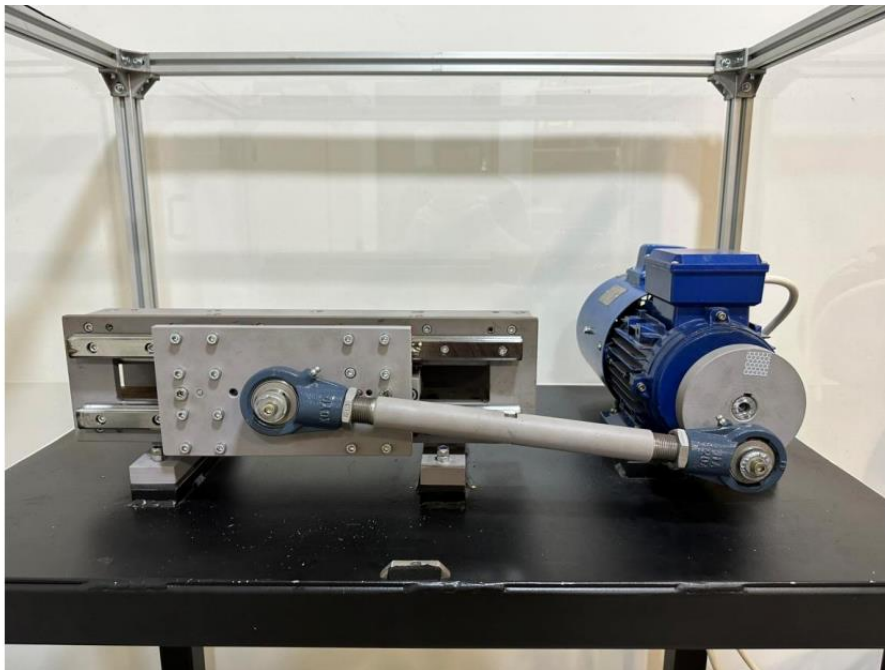Fig.6.9: Wagon placed inside the core

Fig.6.10: Final assembly of the mechanical stressing device

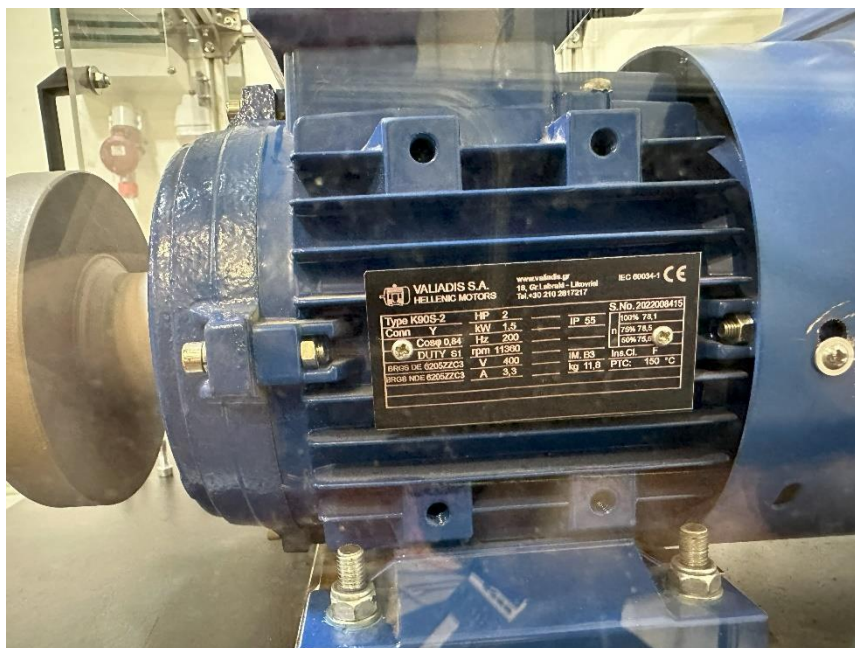Fig.6.11: Inverter used for the mechanical stressing machine drive

Fig.6.12: Induction Motor used for the mechanical stressing machine drive